APPLIED COMPUTATIONAL ELECTROMAGNETICS SOCIETY JOURNAL

October 2014
Vol. 29 No. 10
ISSN 1054-4887

The ACES Journal is abstracted in INSPEC, in Engineering Index, DTIC, Science Citation Index Expanded, the Research Alert, and to Current Contents/Engineering, Computing & Technology.

The illustrations on the front cover have been obtained from the research groups at the Department of Electrical Engineering, The University of Mississippi.

EMERITUS EDITORIAL ASSISTANTS

OCTOBER 2014 REVIEWERS

THE APPLIED COMPUTATIONAL ELECTROMAGNETICS SOCIETY

JOURNAL

Vol. 29 No. 10 October 2014

TABLE OF CONTENTS

Earth Conductivity Estimation from Through-the-Earth Measurements of 94 Coal Mines Using Different Electromagnetic Models

Lincan Yan, Joseph Waynert, and Carl Sunderman

The National Institute for Occupational Safety and Health (NIOSH)
626 Cochrans Mill Road, Pittsburgh, PA 15236, USA
LYan1@cdc.gov, Waynert@ieee.org, CSunderman@cdc.gov

Abstract ─ Through-the-Earth (TTE) communication systems require minimal infrastructure to operate. Hence, they are assumed to be more survivable and more conventional than other underground mine communications systems. This survivability is a major advantage for TTE systems. In 2006, Congress passed the Mine Improvement and New Emergency Response Act (MINER Act), which requires all underground coal mines to install wireless communications systems. The intent behind this mandate is for trapped miners to be able to communicate with surface personnel after a major accident-hence, the interest in TTE communications. To determine the likelihood of establishing a TTE communication link, it would be ideal to be able to predict the apparent conductivity of the overburden above underground mines. In this paper, all 94 mine TTE measurement data collected by Bureau of Mines in the 1970s and early 1980s, are analyzed for the first time to determine the apparent conductivity of the overburden based on three different models: a homogenous half-space model, a thin sheet model, and an attenuation factor or Q-factor model. A statistical formula is proposed to estimate the apparent earth conductivity for a specific mine based on the TTE modeling results given the mine depth and signal frequency.

Index Terms ─ Communication, conductivity, electromagnetic field, Extremely Low Frequency (ELF), Through-the-Earth (TTE), Very Low Frequency (VLF).

I. INTRODUCTION

In coal mines, frequency and effective electrical conductivity of the overburden are factors that determine the maximum range through which a TTE signal can successfully propagate. The effective electrical conductivity of the overburden cannot be controlled and depends on the mine geological properties and varies between different mine sites. Ideally, we would like to be able to predict the apparent conductivity of the overburden to determine the likelihood of being able to establish a TTE communication link. This includes communications between locations within the mine (horizontal communication) and between the underground and the surface (vertical communication). Obtaining information on the overburden electrical properties is useful for evaluating and improving the performance and reliability of a TTE system at a given mine. The limited information on the electrical characteristics of overburden above U.S. coal mines, however, prevents the development of a detailed theoretical approach.

In the 1970s and early 1980s, the Bureau of Mines measured the propagation of TTE signals for frequencies ranging from 600 Hz to 3000 Hz for 94 representative mines distributed throughout the United States. The TTE transmission data collected at the 27 coal mines were initially analyzed to estimate the apparent earth conductivity based upon a homogeneous half-earth model [1]. This model was used to predict the apparent earth conductivity, but it also led to

Submitted On: May 20, 2014
Accepted On: September 6, 2014

unrealistic results of the conductivity decreasing with increasing frequency and depth. Hill and Wait then proposed a thin sheet model to simulate conducting materials, such as pipes, cables, metal sheets, or higher conductivity layers near the surface [2]. This model provides an explanation for the depth dependency of the conductivity. It also predicts the magnitude of decrease in apparent conductivity with frequency by appropriately setting the properties of the conducting sheet. In this paper, the TTE data from all 94 mines are analyzed to determine the apparent conductivity of the overburden based on homogenous half-space model and thin sheet model. Alternately, a mathematically simple model, the Q-factor model, combining features of the two models mentioned above is proposed to predict the dependency of apparent conductivity on both frequency and depth. There is agreement on this prediction based on the thin sheet model and Q-factor model by appropriately choosing the properties of the highly conducting thin sheet layer. Based on the TTE modeling results, we develop statistical formulas that can be used to estimate the earth conductivity for a specific mine, given the mine depth and signal frequency.

II. BACKGROUND

A number of techniques are available for probing the earth electromagnetically with a transmitter and receiver, where conductivity information is contained in the received signal [3-6]. In the mid-1970s, Lagace et al., under the direction of the Bureau of Mines (BOM), conducted extensive TTE propagation measurements yielding the magnetic field (H-field) strengths at 94 coal mine sites [7]. The 94 mines were well-distributed over U.S. coal fields and were selected from the total mine population based on the depth and the number of mine workers (Table 1). In parallel, the BOM conducted additional TTE measurements at 27 coal mines which were selected from the 94 mines [1]. The sampling procedure used to select the 94 mines out of all US coal mines was based on the following principles:

1) each mine had a chance of being selected for this test;
2) the probability of selection was known beforehand and was based on the relative size of the mine in terms of the number of miners employed;
3) the selection process was random;
4) all depth intervals were selected;
5) test results could be used to make valid inferences about all mines [7].

Table 1: Overburden depth distribution of 94 coal mines in 1975[1]

Depth m	Depth ft.	Sampling Size	# Of Active Mines
<61.0	<200	2	73
61.3-121.9	201-400	35	369
122.2-182.9	401-600	30	309
183.2-243.8	601-800	13	199
244.1-304.8	800-1000	4	135
305.1-365.8	1001-1200	6	58
>365.8	>1200	4	79

III. METHODOLOGY

A. Homogenous half-space model

The homogenous half-space model can be illustrated by setting either the conducting sheet depth to $d=0$ or $\sigma=\sigma_0$, in Fig. 1. The vertical magnetic dipole source (small horizontal loop) has a magnetic moment IA and is located at $z=-h$ on the z axis of a cylindrical coordinate system (ρ, ϕ, z), where I is the current through the loop wire and A is the area formed by the circular loop. The earth media has a conductivity of σ_0 and an intrinsic propagation constant of $\gamma_0 = \sqrt{\mu\omega(j\sigma_0 - \omega\varepsilon_e)}$, where j is the square root of -1, ω the operating angular frequency, μ the permeability of the earth or air, and ε_e the earth dielectric constant. The displacement currents are usually very small and will be neglected for all TTE frequencies compared to the conduction currents, so approximation $\gamma_0 \approx \sqrt{j\omega\mu\sigma_0}$ is reasonable. The vertical H-field at the surface can be derived from a magnetic Hertz vector with only a z component, along with the application of

[1] MSHA and Bureau of Mines data files as of 1975.

appropriate boundary conditions [8]. It can also be obtained by setting the conductivities σ_1 and σ_2 both equal to σ, or the thickness h_1 of the upper layer can be considered to vanish and $\sigma_2 = \sigma$ in a 2-layer model [8]. This gives:

$$H_z = b_0 Q_{homo}(\omega, \sigma_0, h), \quad (1)$$

where

$$Q_{homo}(\omega, \sigma_0, h) = \frac{h^3}{2}\int_0^\infty \lambda^2 T(\lambda)\, e^{-\lambda z} J_0(\lambda\rho) d\lambda, \quad (2)$$

and

$$T(\lambda) = \frac{2\lambda}{k_0+\lambda} e^{-k_0 h}. \quad (3)$$

In the equations above, b_0=IA/($2\pi h^3$) is the value of H-field on the axis a distance h above a loop in free space, $Q_{homo}(\omega, \sigma_0, h)$ represents the attenuation factor due to the conductive earth. J_0 is the first order of Bessel function of the first kind, and $k_0 = (\lambda^2 + {\gamma_0}^2)^{1/2}$.

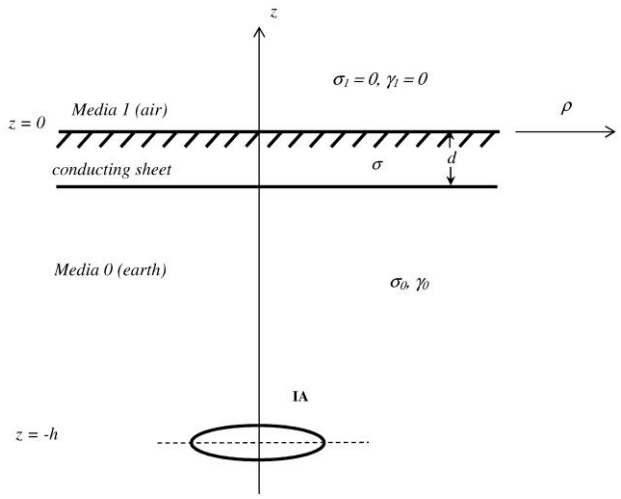

Fig. 1. A small horizontal loop (vertical magnetic dipole) buried in a dissipative half-space with a thin conducting sheet at the surface.

B. Thin sheet model

As we will see later, one result from applying the homogeneous model to the data of the 94 mines is that the apparent conductivity appears to decrease as the mine depth increases, which is contradictory to the model itself. However, this dependency might be explained by the presence of a thin highly conducting layer at the surface of the earth. In the thin sheet model, as depicted in Fig. 1, the highly conducting thin sheet represents the overall effect of possible surface metal structures, such as cables, pipes, cased bore holes, etc., as well as the relatively high conductivity at the surface which usually contains more dissolved salt and mineral substances. Note that $d \ll h$. Wait and Spies have derived the H-field from the electric vector potential [8]. Following their work, here we use magnetic Hertzian potential to obtain the vertical H-field in the air based on potential theory.

For the earth layer (z<0) and free space (z>0), the magnetic Hertzian potential Π^* satisfies the wave equation except at the exciting source:

$$\begin{cases} (\nabla^2 - {\gamma_0}^2)\Pi_0^* = 0, & z < 0 \\ \nabla^2 \Pi_1^* = 0, & z > 0 \end{cases}, \quad (4)$$

where

$${\gamma_0}^2 = \mu\omega(j\sigma_0 - \omega\varepsilon_0) \approx j\mu\omega\sigma_0, \quad (5)$$

is the intrinsic propagation constant. For free space (z>0), $\sigma_1 = 0$, hence, $\gamma_1 \approx 0$.

In a cylindrical coordinate system, the fields in the half-space (z<0) can be expressed in terms of Hertzian potential Π_0^*, in which 0 denotes the medium 0 (earth):

$$\begin{cases} \{H_{0\rho}, H_{0z}\} = \left\{\frac{\partial^2 \Pi_0^*}{\partial\rho\partial z}, \left(-j\mu\omega\sigma_0 + \frac{\partial^2}{\partial z^2}\right)\Pi_0^*\right\} \\ E_{0\phi} = j\mu\omega \frac{\partial \Pi_0^*}{\partial \rho}, \end{cases} \quad (6)$$

and the fields in the free space (z>0) can be expressed in terms of Π_1^*:

$$\begin{cases} \{H_{1\rho}, H_{1z}\} = \left\{\frac{\partial^2 \Pi_1^*}{\partial\rho\partial z}, \frac{\partial^2}{\partial z^2}\Pi_1^*\right\} \\ E_{1\phi} = j\mu\omega \frac{\partial \Pi_1^*}{\partial \rho}. \end{cases} \quad (7)$$

Note that the magnetic Hertzian potential $\mathbf{\Pi}^*$ has only a z component; i.e., $\mathbf{\Pi}^* = \Pi^* \hat{z}$. The magnetic Hertzian potential in each region is listed below:

$$\Pi_0^* = \frac{IA}{4\pi}\int_0^\infty J_0(\lambda\rho)\left(\frac{\lambda}{k_0} e^{-k_0|z+h|} + R_0(\lambda) e^{k_0 z}\right) d\lambda, z < 0, \quad (8)$$

$$\Pi_1^* = \frac{IA}{4\pi}\int_0^\infty T_1(\lambda) e^{-k_1 z} J_0(\lambda\rho) d\lambda, z > 0. \quad (9)$$

$R_0(\lambda)$ and $T_1(\lambda)$ are unknowns and can be determined by the application of the boundary conditions. The boundary condition here requires that at the layer interface the azimuthal E-field is continuous and the tangential H-field is discontinuous by the amount of longitudinal current per unit length carried by the thin sheet:

$$R_0(\lambda) = \frac{\lambda(k_0 - k_1 - j\omega\mu\sigma d)}{k_0(k_0 + k_1 + j\omega\mu\sigma d)} e^{-h k_0}, \quad (10)$$

$$T_1(\lambda) = \frac{2\lambda}{k_0 + k_1 + j\omega\mu\sigma d} e^{-h k_0}. \quad (11)$$

The surface vertical H-field in (7) then is given by:

$$H_z = b_0 Q_{thin}(\omega, \sigma_0, h, \sigma, d), \quad (12)$$

in which

$$Q_{thin}(\omega,\sigma_0,h,\sigma,d) = \int_0^\infty \frac{\lambda h^3 {k_1}^2}{k_0+k_1+j\omega\mu\sigma d} e^{-k_1 z-k_0 h} J_0(\lambda\rho) d\lambda. \quad (13)$$

For free space, $k_1 = (\lambda^2 + {\gamma_1}^2)^{1/2} = \lambda$. Equation (13) then can be rewritten as:

$$Q_{thin}(\omega,\sigma_0,h,\sigma,d) = \int_0^\infty \frac{\lambda^3 h^3}{k_0+\lambda+j\omega\mu\sigma d} e^{-\lambda z-k_0 h} J_0(\lambda\rho) d\lambda. \quad (14)$$

To avoid exponential attenuation when the signal passes through the highly conducting thin sheet, the value of $\gamma_0 d$ in this model is required to be small enough ($\gamma_0 d < 1$). Similarly as in (1), $Q_{thin}(\omega,\sigma_0,h,\sigma,d)$ here represents the attenuation factor due to the conductive earth and the thin sheet. An interesting feature of the attenuation factor $Q_{thin}(\omega,\sigma_0,h,\sigma,d)$ in (14), is that the dependence on σd is algebraic rather than exponential. This type of algebraic dependence is typical of thin conducting sheets regardless of the geometry [8].

C. Q-factor model

Since Q in (1) and (12) monotonically decreases with σ_0 and/or σ, an apparent conductivity value σ_a can be determined by assuming reasonable input values for the homogeneous half-space and thin sheet model. The procedure is to compute $Q_{thin}(\omega,\sigma_0,h,\sigma,d)$ using reasonable values of σ_0 and σd, and then equate the magnitude of Q_{thin} to that of a homogeneous half-space and determine the value of σ_a:

$$Q_{homo}(\omega,\sigma_a,h) = Q_{thin}(\omega,\sigma_0,h,\sigma,d). \quad (15)$$

IV. NUMERICAL EVALUATION AND RESULTS

The numerical integration of (2) and (14) can be evaluated by using a variable exchange, as shown below [9]:

$$x = \lambda h; D = \rho/h; Z = z/h; T = h/\delta;$$
$$\text{with } \delta = \sqrt{\frac{2}{\omega\mu\sigma}}. \quad (16)$$

Then the wave number k_i, can be rewritten as $k_0 = x/h; k_1 = \frac{1}{h}\sqrt{x^2 + jH^2}$, with $H = \sqrt{2}\, h/\delta$.

A. Based on the homogenous half-space model

For the TTE tests at the 94 mines, four transmission frequencies-630, 1050, 1950, and 3030 Hz-were used at each site. The magnetic moment, M=NIA (N is the number of turns of wire), for the in-mine transmitting loop was recorded and calibrated. Corrections have also been made on the overburden depth h for all the mine sites to account for possible horizontal offsets from the point directly above the transmitters [7]. After normalizing the surface vertical H-field to the corresponding M, the apparent earth conductivity, σ_a, can then be obtained by solving (1).

The resulting apparent earth conductivity distribution with overburden depth interval is listed in Table 2. The computed conductivity values for the mine with the least overburden depth appear to be a large outlier compared to the rest of the data and were excluded from further consideration. Also, because of the large expected uncertainty in the conductivity estimates for large Q, the data for about 25% of the 94 mines in which $|Q|>0.5$ were excluded. By examining Table 2, we can see that the estimated conductivity values tend to decrease with increasing depth by a factor of 25-30 over the depth range at each given frequency. This number is in contrast to the factor of 10 obtained by Durkin based on the data of 27 mines [10]. The estimated apparent conductivity in Table 2 also shows a dependence on frequency that decreases by a factor of ~3 over the frequency range at each given depth interval. Analyzing only 27 out of 94 mine data in [10], does not quite predict the magnitude of decrease in the apparent conductivity with depth and frequency. However, we would not expect the conductivity to decrease with increasing frequency or depth for the homogenous model. Another observation based on Table 2, is that the standard deviation of the conductivity distribution in each depth interval tends to decrease with overburden depth for all frequencies. This suggests that deep coal mines have smaller and more evenly distributed conductivity values than shallow coal mines.

Table 2: Apparent conductivity ($\boldsymbol{\sigma_a}$, S/m) distribution with overburden depth (m) interval for 94 coal mines at different frequencies based on the homogenous half-space earth model; the "std" denotes the conductivity standard deviation in each depth interval

Mine Depth (m)		630 Hz	1050 Hz	1950 Hz	3030 Hz
50-100	Mean	0.6185	0.4202	0.2564	0.1559
	STD	0.3062	0.3531	0.1767	0.1240
100-150	Mean	0.2760	0.1301	0.0858	0.0511
	STD	0.1350	0.0732	0.0465	0.0379
150-200	Mean	0.1425	0.0942	0.0498	0.0452
	STD	0.0963	0.0548	0.0347	0.0346
200-250	Mean	0.1307	0.0867	0.0378	0.0414
	STD	0.0826	0.0524	0.0238	0.0233
250-300	Mean	N/A	0.0170	0.0185	0.0140
	STD	N/A	N/A	0.0219	N/A
300-350	Mean	0.0380	0.0250	0.0170	0.0120
	STD	0.0354	0.0156	0.0141	0.0099
350-400	Mean	0.0265	0.0183	0.0130	0.0118
	STD	0.0261	0.0153	0.0076	0.0049
400-450	Mean	0.0220	0.0245	0.0230	0.0090
	STD	0.0118	0.0035	N/A	0.0085
450-500	Mean	0.0180	0.0170	0.0080	0.0050
	STD	N/A	N/A	N/A	N/A

B. Based on the thin sheet model

It may be possible to explain the behavior of the conductivity on frequency and depth as seen in the previous section by the addition of a thin, highly conducting layer at the surface of the earth [11]. A shallow mine would then have a more weighted contribution from the high conducting surface layer than a deep mine, and the apparent conductivity would decrease with greater depth. The estimated apparent conductivities of those mines with $|Q|<0.5$ based on the thin sheet model are calculated and sorted into several overburden depth intervals, and then plotted with depth interval as in Fig. 2 for various σd values and various frequencies. As mentioned earlier, although the conductivity of the thin sheet can be very high, choosing of product value σd is not arbitrary. The value of $\gamma_0 d$, hence the value of d, is required to be small enough to avoid exponential attenuation as the signal travels through the highly conducting thin sheet. One interesting finding is that the apparent conductivity has a greater dependency on the overburden depth at low frequency than at high frequency, as shown in Fig. 2; i.e., the derivative of the exponential curve fit has a greater value at low overburden depth than at greater depths. The exponential curve-fitting equations in these plots provide a good prediction for the depth dependency of the conductivity. This model also predicts the magnitude of decrease in the apparent conductivity with frequency as seen in Table 2, by the appropriate choice of value of σd.

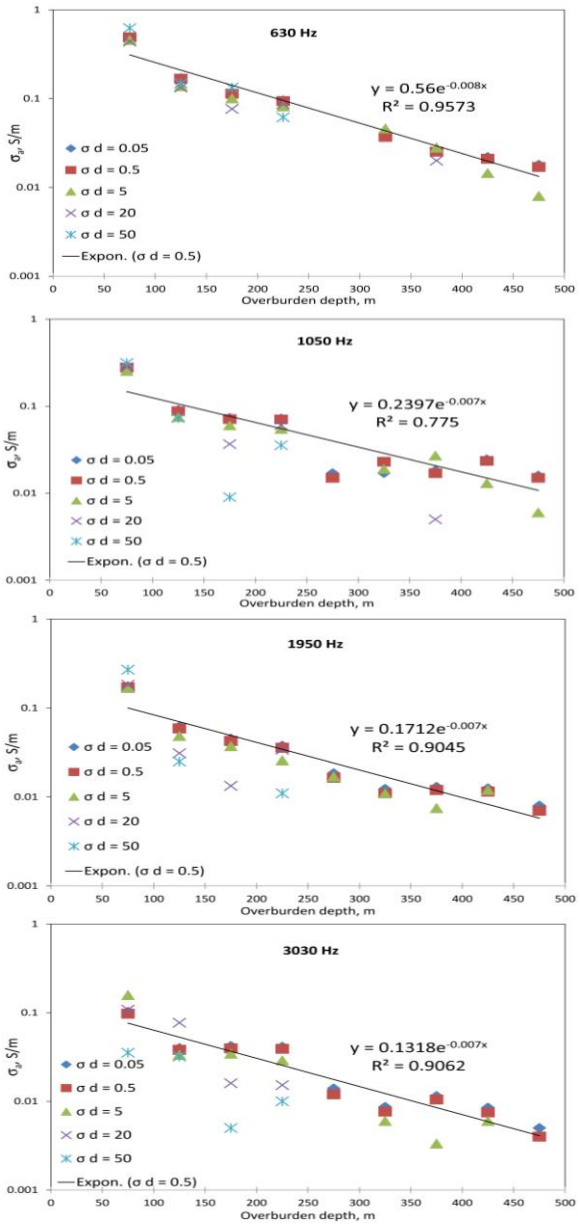

Fig. 2. Estimated apparent conductivities (S/m) change with overburden depth interval (m) for various $\boldsymbol{\sigma d}$ and frequencies (630 Hz, 1050 Hz, 1950 Hz, 3030 Hz) based on the thin sheet model.

C. Based on Q-factor model

While EM measurements of both transmitting and receiving antennas are needed for the models described above, the Q-factor model or attenuation factor model requires only two parameters: the estimated earth conductivity σ_0 and the conductivity thickness product σd of the thin sheet. Through the use of (15), we can calculate the apparent conductivity. The apparent conductivity values based on this model are plotted in Fig. 3. Again the value of $\gamma_0 d$, hence the value of d, is required to be small enough for the reason mentioned in the thin sheet model above. By comparing the exponential coefficients in the fitting functions as shown in Figs 2 and 3, the depth dependency of this model when $\sigma d = 20$ is very close to that of the thin sheet model. Furthermore, this approach can predict the dependency of apparent conductivity on frequency, as well as on depth, by choosing the value of σd appropriately.

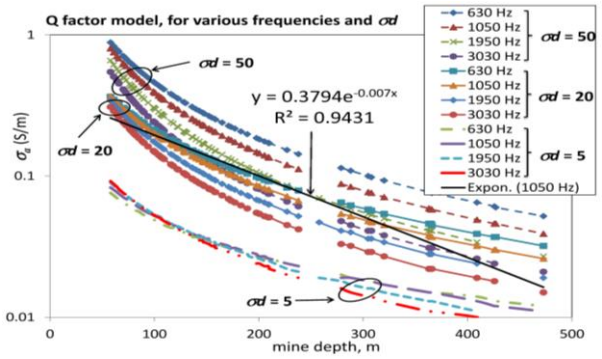

Fig. 3. Apparent conductivity (σ_a, S/m) for different frequencies and $\boldsymbol{\sigma d}$ based on the Q-factor model.

D. A regression model based on statistical approach

The conductivity of overburdens above mines in U.S. coal fields can be characterized as a function of overburden depth and operating frequency. The overburdens consist of a large number of horizontal layers of different materials and thicknesses. For any given overburden depth, we can expect overburden characteristics such as conductivity to vary from location to location within the coal fields. Hence, we can develop a statistical approach of sampling a representative number of mines within each of the depth intervals of interest in order to characterize the overburden conductivity, and the corresponding variability about the average, as a function of depth and operating frequency.

In the regression model, overburden apparent conductivity is considered to be related to depth and frequency in an unknown pattern. Up to 94 data points were obtained as a result of field tests conducted at each of four frequency levels. With the assumption that the estimated values of apparent conductivity represent a random sample from a normal distribution with a mean dependent upon both frequency and depth and variance independent of both frequency and depth, a regression model can be obtained to describe the dependency of the apparent conductivity on both frequency and depth as shown in (17). In this model, σ_a is the apparent conductivity to be estimated, and a, b, and c are the regression coefficients to be determined from the mine data. The model values are given in Table 3. The random mine selection process was used to ensure that all measurements can be described by a log-normal probability law. The Cumulative Distribution Function (CDF) of the estimated apparent conductivity (based on the homogenous model) for all frequencies and depths is shown in Fig. 4. From the CDF plot, about 95% of conductivity values fall below 0.5 S/m, and about 60% of them fall below 0.1 S/m. It is worthy to mention that since the values in Table 3 (including standard error) is averaged over all the frequencies and overburden depths (as shown in Table 2), this regression model predicts apparent conductivity more reasonably for low frequencies and shallow mines than for high frequencies and deep mines:

$$\sigma_a = a + b * \log(freq) + c * \log(depth). \quad (17)$$

In the regression model as described in (17), the coefficient of frequency is of the same order as that of the depth, so the frequency dependency cannot be ignored in the apparent conductivity estimation in contrast to previous analyses [10].

Table 3: Regression model for apparent conductivity (σ_a, S/m) with respect to log depth (m) and log frequency (Hz)

Observations	238
a	2.1834
b	-0.2932
c	-0.5068
Standard Error	0.1479
R Square	0.4674

The apparent conductivity of a specific mine with given overburden depth and operating frequency can then be estimated based on this model, with the related coefficients to fit (17) as shown in Table 3.

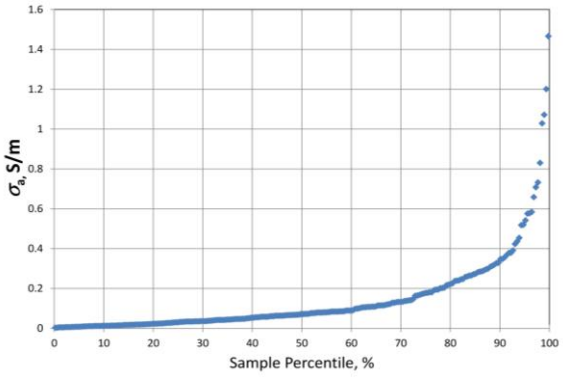

Fig. 4. Estimated apparent conductivities plotted with distribution percentile.

V. CONCLUSION

The TTE data from all 94 mines recorded by the BOM in the 1970s were analyzed to estimate the overburden apparent conductivity based on three different models: a homogenous half-space model, a thin sheet model, and a Q-factor model. In the past, full analysis of this data was constrained by computing limitations. The apparent conductivities from the 94 mine data were first estimated based on a homogenous half-space model. The results based on this model show that the apparent conductivity decreases with increasing depth and frequency, which is contrary to the expectations of the model. A thin sheet model was then considered, which is able to provide an explanation for the depth dependency of the conductivity. It also predicts the magnitude of decrease in the apparent conductivity with frequency by appropriately setting the properties of the conducting sheet. Alternately, the Q-factor model was also shown to predict the dependency of apparent conductivity on both frequency and depth by appropriately choosing the properties of a highly conducting thin sheet layer. Among those methods, the thin sheet model provides more reasonable estimation since it considers the effect of the relatively high conducting surface on overall apparent conductivity. By combining the features of the other two models, the Q-factor model also gives a good prediction but is mathematically simple. The conductivity behavior was also described based on a linear-logarithm regression model. The results provided in this paper offer more insight into the overburden apparent conductivity and help to predict the path loss. This estimation of earth conductivity can be used by the mine owner/operator or TTE vendor to predict the performance of the TTE system.

REFERENCES

[1] J. Durkin, "Study of through-the-earth transmission data as applied to earth conductivity," *U. S. Bureau of Mines*, Pittsburgh Mining and Safety Researcher Center, 1981.

[2] D. A. Hill and J. R. Wait, "Theoretical noise and propagation models for through-the-earth communication," *National Telecommunications & Information Admin.*, Institute for Telecommunication Sciences, 1982.

[3] J. R. Wait, "Mutual electromagnetic coupling of loops over a homogeneous ground," *Geophysics*, vol. 20, pp. 630-637, 1955.

[4] J. R. Wait, "Electromagnetic waves in stratified media," *The MacMillan Co*., 1962.

[5] G. V. Keller and F. C. Frischknecht, "Electrical methods in geophysical prospecting," *Pergamon*, 1966.

[6] I. IEEE Standard 356, "Guide for radio methods of measuring earth conductivity," *Institute of Electrical and Electronics Engineers*, p. 18, 1974.

[7] R. L. Lagace, J. M. Dobbie, T. E. Doerfler, W. S. Hawes, and R. H. Spencer, "Detection of trapped miner electromagnetic signals above coal mines," *Arthur D. Little, Inc*., Cambridge, Massachusetts, 1980.

[8] J. R. Wait and K. P. Spies, "Evaluation of the surface electromagnetic fields for a buried magnetic dipole source," *DTIC Document*, 1971.

[9] J. R. Wait, "Subsurface electromagnetic fields of a circular loop of current located above ground," *IEEE Transaction on Antennas and Propagation*, vol. 20, pp. 520-522, 1972.

[10] J. Durkin, "Apparent earth conductivity over coal mines as estimated from through-the-earth electromagnetic transmission tests," *U.S. Bureau of Mines*, Pittsburgh Mining and Safety Research Center, 1984.

[11] R. G. Geyer, G. V. Keller, and T. Ohya, "Research on the transmission of electromagnetic signals between mine workings and the surface," *Colorado School of Mines*, 1974.

Lincan Yan is a Research Scientist for the National Institute for Occupational Safety and Health (NIOSH). He received his B.S. degree in Mining Engineering from Northeastern University, Shenyang, China; M.E. degree in Engineering Mechanics from Tsinghua University, Beijing, China; M.S. degree in Mechanical Engineering from University of New Mexico (UNM), Albuquerque, NM, USA; and Ph.D. in Electrical Engineering from UNM. Having studied and worked in academia and in the laboratory, he has many years of experience in designing and conducting experiments. He is currently an RF Research Engineer at the National Institute for Occupational Safety and Health, Pittsburgh, PA, USA, where he works on through-the-earth wireless communication projects as a member of the Electrical Safety and Communications Team. By utilizing highly sensitive receive antennas and optimizing transmission, he conducts research on monitoring very weak VLF/ULF radio signals and improving communication range. His work also includes investigating factors that will affect communication in coal mines.

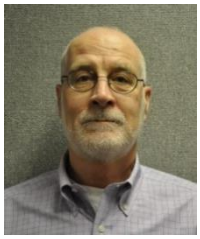

Joseph A. Waynert is a Team Leader at the National Institute for Occupational Safety and Health (NIOSH). His primary research focuses on wireless communications and electronic tracking. In particular, he is experimentally and theoretically investigating the mechanisms controlling path loss in underground coal mining applications. System frequency bands of interest include ELF, MF, and UHF. Prior to NIOSH, Waynert worked in the industry investigating methods of improved spectrum management for the military. Previous to that he worked at Los Alamos National Lab developing applications of applied superconductors. Waynert has a Ph.D. in Physics from the University of Wisconsin-Milwaukee.

Carl Sunderman is a Research Electrical Engineer for the National Institute for Occupational Safety and Health. He has twenty years of experience in the areas of mining equipment automation, geophysical electronics, and radio propagation, and is currently working on projects related to improvements in subterranean communication and pedestrian tracking technologies. He holds a BSEE and MSEE from Gonzaga University.

A Novel Switchable Double Band-Notch Antenna for Ultra-Wideband Application

Mohammad Naser-Moghadasi and Sajjad Faraji Qotolo

Faculty of Engineering, Science and Research Branch
Islamic Azad University, Tehran-Iran
mn.moghaddasi@srbiau.ac.ir, s.faraji_telecom@yahoo.com

Abstract ─ A novel microstrip-fed planar monopole antenna is proposed that is miniaturised in size and provides reconfigurable band-notch properties. The antenna's impedance bandwidth is 150% for VSWR < 2 across 2.6-18.3 GHz, thus satisfying FCC's frequency requirement for UWB systems defined between 3.1-10.6 GHz. To circumvent interference issues resulting from existing nearby communication systems within the UWB operating frequency, the antenna includes an inverted open-loop triangular slot embedded in the hexagonal shaped radiation patch to realize a band-notch response between 3.1 to 3.9 GHz necessary to reject the WiMax band, and open-end resonator structures at both sides of the patch to create a band-notch response between 5.1 to 5.9 GHz, thus enabling band rejection of WLAN and Hyperlink systems. Furthermore, it is demonstrated the band-notch can be electronically controlled without compromising the antenna's characteristic features. This is achieved by strategically located PIN diodes on the antenna.

Index Terms ─ Microstrip-fed monopole antenna, switchable band notch antenna, Ultra-Wideband (UWB) antenna.

I. INTRODUCTION

Ultra-wideband is a radio technology that can be used at very low energy levels for short-range high-bandwidth communications by using a large portion of radio spectrum. This technology has been widely used in non-cooperative radar imaging, target sensor data collections, and other military communications during the past two decades [1]. Regulatory setting of Federal Communications Commission (FCC) approved the frequency range of 3.1~10.6 GHz for commercial use of UWB systems in 2002. With regards to advantages of UWB antennas, such as high data transmission rate (100 M to 1 G/bps) over short distances, small size, [2] low power consumption (~200 μW), omni-directional pattern, low group delay, constant gain, and linear phase response, there is no surprise that the design of these antennas have drawn researchers' attention in recent years.

A suitable UWB antenna should be capable of operating over the allocated range of frequency, moreover satisfactory radiation properties over the entire frequency range are also necessary [3].

The existing narrow band wireless systems, such as Wireless Local Area Network (WLAN) and Hyperlink using IEEE 802/11a protocol, which are operating over 5.15-5.35 GHz (Band A) for indoor mobile and 5.47-5.725 GHz (Band B) for indoor and outdoor WLAN networks. The higher band 5.725-5.825 GHz (Band C), is a licensed band to be used for the installation of Fixed Wireless Access (FWA) services between stationary points [4,5]. In addition, Worldwide Interoperability for Microwave Access (WiMax) using the frequency band of 3.15-3.85 GHz, can cause the performance degradation of UWB systems due to the absence of band pass filters [6,7]. To overcome electromagnetic interference between UWB and other narrow band systems, various UWB antennas have been designed by different researchers to omit the undesirable bandwidth to avoid any kind of interference [9].

In this way, etching different kinds of slots on the patch or ground of antenna, such as U-shaped [8] or V-shaped slots is most commonly used [10]. Also, other techniques such as adding a parasitic

Submitted On: May 7, 2013
Accepted On: September 5, 2014

element [12,13], using folded strips, etching Split Ring Resonator (SRR) [14], and embedding resonator cells feeding line of antennas [15,16] can effectively filter the undesired bands.

The technique proposed in this paper elicits the inherent advantages of planar antennas for operation across the entire UWB spectrum. This is achieved by embedding an inverted open-loop triangular slot on the patch and incorporating open-end resonator structures on both sides of the patch. The proposed antenna has an impedance bandwidth of 15.7 GHz between 2.6 GHz to 18.3 GHz for VSWR < 2, and it radiates omni-directionally in both the E- and H-planes. Moreover, by mounting PIN diodes across the slot and between the open-end resonator structure and the patch, the notch bands can be electronically controlled.

II. ANTENNA DESIGNATION

Figure 1 (a) shows the physical geometry of the proposed antenna that comprises of a hexagonal shaped radiator with a 50 Ω microstrip feed-line, an inverse triangular shaped slot with a narrow horizontal section, and open-end resonator arms connected to the patch. The antenna was designed to operate at a frequency range between 2.7 to 18 GHz, with two notched bands that are determined by the slot and resonator structures. The microstrip monopole antenna was simulated and its performance optimized using HFSS.

The antenna's optimized parameters and photograph are shown in Fig. 1. The microstrip feed-line is 2 mm corresponding to a characteristic impedance of 50 Ω. The antenna was fabricated on Rogers 4003 substrate with thickness of 1.6 mm, relative dielectric permittivity ε_r=3.55, and dielectric loss $\tan\delta$ =0.0027. The proposed antenna is relatively small with dimensions 18.4×21 mm^2.

It is well known that microstrip patch antenna structures designed to operate at a given resonant frequency possess a limited bandwidth. This limitation can be compensated by introducing additional radiating patches located close to the main radiator. In the proposed antenna, the open-end resonant structures are electromagnetically coupled to the radiating patch in such a way as to perturb the antenna to extend its bandwidth response. Furthermore, the open-end resonator structures provide the desired rejection notch band. The gap between the plate and the open-end resonator arms was set to 0.4 mm to enhance its electromagnetic coupling with the radiating patch and to broaden the antenna's impedance bandwidth. To comprehend the phenomenon behind this dual band-notch performance and UWB frequencies, Fig. 2 (a,b,c) shows the simulated current radiation at 3.5 GHz for WiMax band that is first frequency band notch, and 5.5 GHz for WLAN band at the middle of the second stop band, and 8 GHz for operating in UWB systems.

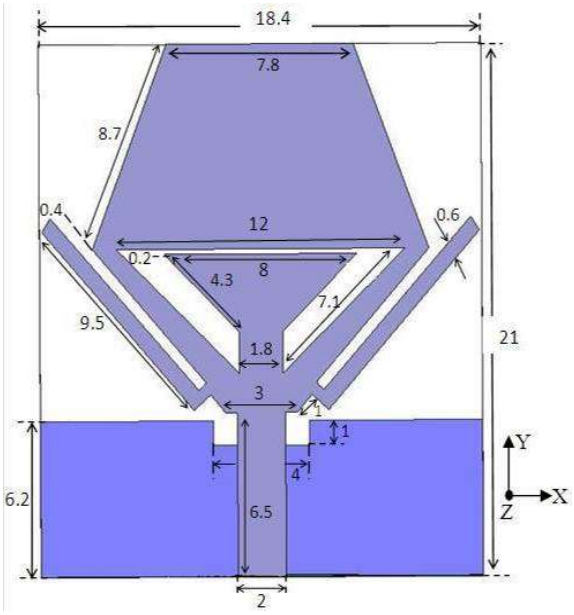

(a)

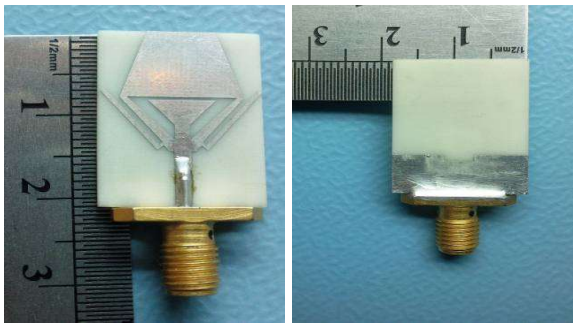

(b) (c)

Fig. 1. (a) Geometry of proposed antenna, (b) top view of the proposed UWB antenna, and (c) bottom view of the antenna with ground plane.

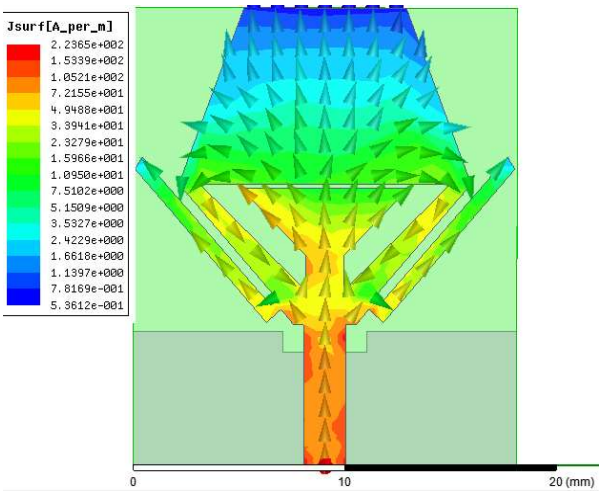

(a) 3.5 GHz

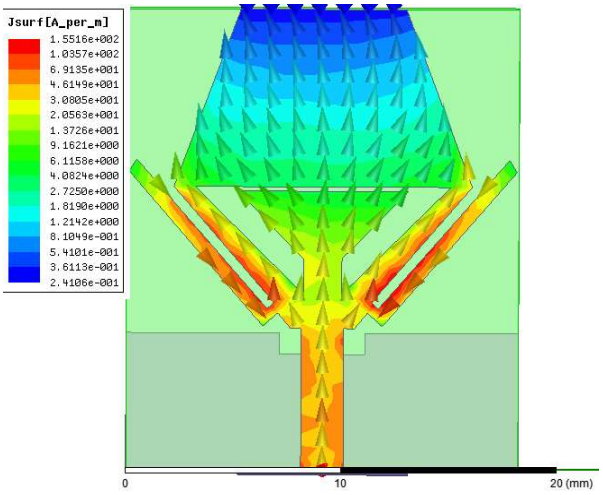

(b) 5.5 GHz

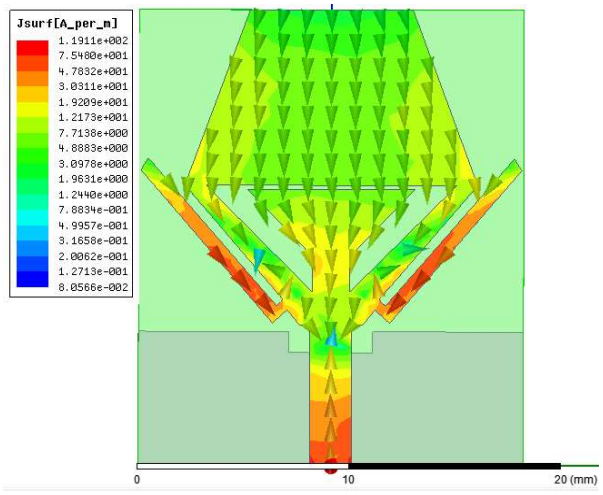

(c) 8 GHz

Fig. 2. Simulated surface current on the radiation patch: (a) 3.5 GHz, (b) 5.5 GHz, and (c) 8 GHz.

The regions of greatest current intensity are over the open-loop resonator structures and the adjacent region on the patch. It can be observed from Fig. 2 (b), that the direction current in the resonator and the adjacent patch are oppositely directed, therefore, we can eliminate the WiMax band. It is also discernable, the intensity is greatest in the lower part of the feed-line too. Moreover, the region around the middle section of the slot has least current intensity.

III. SIMULATION AND MEASUREMENT RESULTS

A. Stop bands design

In the previous section, the proposed antenna with optimal geometrical parameters was analyzed. The fabricated antenna's performance was measured using Agilent's Network Analyzer E8361c. The VSWR response of the microstrip monopole antenna under three scenarios now described, is depicted in Fig. 3. The first stop-band with central frequency of 3.5 GHz is located at the WiMax band, and is achieved by inserting an inverted open-loop triangular slot in the middle of the hexagonal shaped radiating patch. The second stop-band with central frequency of 5.5 GHz is located at the WLAN band, and is created by adding open-end resonator arms on both sides of the patch.

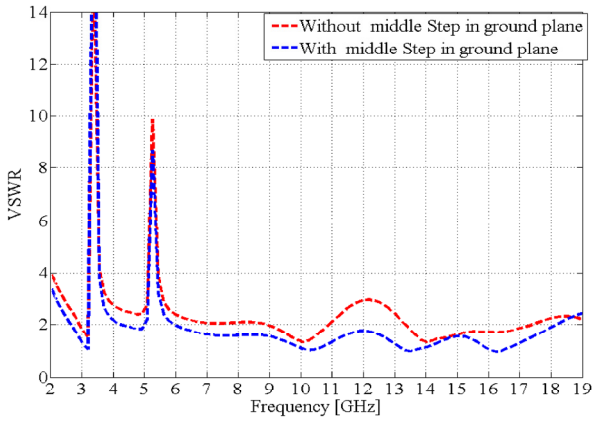

Fig. 3. Simulated VSWR for the antenna with and without middle step in ground-plane.

The antenna's mismatch improves between 11-13.4 GHz by creating a step in the ground-plane around the feed-line near the patch, and hence, its impedance bandwidth improves

significantly as shown in Fig. 3. This is because, by cutting a notch in the ground-plane provides an additional current path, which changes the inductance and the capacitance property of the feed-line at that point. The overall bandwidth improves from 2.9-11.0 GHz to 2.6-18.2 GHz. It should be noted that the effect of mutual coupling between the first and second notched bands of the antenna does not adversely affect the overall response of the antenna. As the antenna configuration is symmetrical with respect to x-axes, this improves its co-polarized patterns and suppresses its cross-polarized radiation.

The simulated and measured VSWR of the proposed antenna is shown in Fig. 4. The measured bandwidth of fabricated antenna is between 2.8 and 17.7 GHz for VSWR<2. The first rejection frequency band is from 3.3 to 4.2 GHz, and the second band notched characteristics is exhibited between 5.2 to 6 GHz. The correlation between the simulation and the experimental results is excellent; it is result of faithful designation of monopole antenna, precise assembly of the antenna with low loss connectors, and accuracy calibration band with return loss better than 50 dB from 1 to 20 GHz with network analyzer.

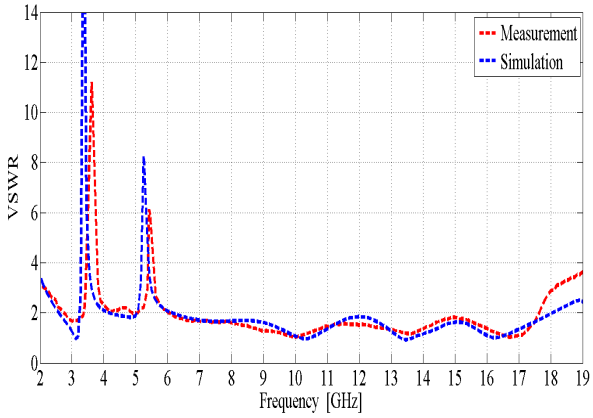

Fig. 4. Simulated and measured VSWR of the proposed antenna.

If we consider the simulation and the measurement graphs in Fig. 4, it can be found a shift in the peaks in both the stop bands that refer to the 5% tolerance in relative permittivity ε_r and substrate thickness that here is 1.6 mm. As we know, the effective relative permittivity of a patch antenna is defined as:

$$\varepsilon_r^{eff} = (\frac{\varepsilon_r + 1}{2}) + (\frac{\varepsilon_r - 1}{2})[1 + 12(\frac{h}{w})]^{-1/2}.$$

In addition, the guided wavelength is defined as:

$$\lambda_g = \frac{c}{f\sqrt{\varepsilon_r^{eff}}}.$$

So if we assume the effective relative permittivity is increased with the tolerance in the fabrication process as mentioned above, therefore, the guided wavelength becomes lower than expected value and causes a frequency shift in both notch bands.

B. Switching modes by PIN diode

To realize an UWB antenna with reconfigurable band-notch characteristics, PIN diodes were employed [11]. The PIN diodes were located across the horizontal thin section of the triangular slot in the patch, and between the open-end resonator arms and the main patch, as shown in Fig. 5.

The PIN diodes were strategically located in the antenna's structure based on the surface current distribution in Fig. 2. To enable the notched bands to be electronically selected by simply switching the diodes either 'on' or 'off' without compromising the antenna's overall performance.

The current distribution on the middle of the triangular slot and the end of the resonator stubs that connected to the patch by PIN diodes, has the minimum dense and the potential deference that can be changed on the current direction on the radiating elements. The selectivity function enhances the functionality of the UWB antenna.

In Fig. 5 (c), the PIN diode labelled (a) can switch either 'on' or 'off' the first notch band of the antenna centered at the frequency of the WiMax system. PIN diodes labelled (b) and (c) can activate or deactivate the antenna's second stop band in order to mitigate interference from WLAN devices.

The type of PIN diodes used in the proposed antenna is HSMP-3820 that has an equivalent circuit given in Fig. 5 (d). To take the ideal behaviour of the diode into account in the simulation, the PIN-diode was modelled as a lumped element capacitor in open state and as a lumped element resistor in shorted state.

The three pairs of identical PIN diodes mounted on the proposed UWB dual band-notched planar monopole antenna were modelled

in accordance to its characterizing parameters; namely, resistance of 2.5 Ω in the 'on' state and capacitance of 0.8 pF in the 'off' state. The PIN diodes were activated by applying a bias voltage of 5V.

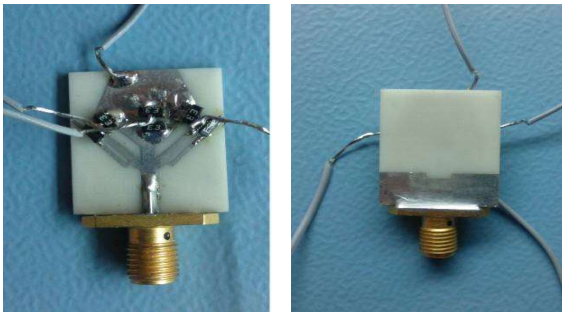

(a) (b)

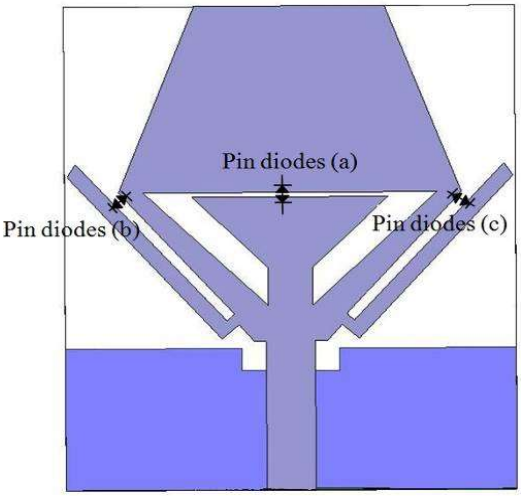

(c)

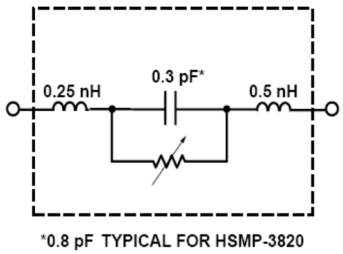

(d)

Fig. 5. (a) Photograph of antenna with PIN switching diodes, (b) back plane of the antenna, (c) location of the PIN diodes in the patch antenna, and (d) equivalent circuit of PIN diode (HSMP 3820).

Figure 6 shows the simulation result of antenna's VSWR for various PIN diode bias conditions. The biasing wires do not simulate in HFSS software, but the resistance and the capacitance property of the PIN diodes assumed when they are in OFF or ON state. When all the PIN diodes are in the ON state, the antenna operates like a UWB monopole antenna without any notch bands. When the PIN diodes labelled (a) are in the OFF state and PIN diodes labelled (b, c) are in the ON state, only the WiMax notch is activated in overall band. When the PIN diodes labelled (a) are in the ON state and PIN diodes labelled (b, c) are in the OFF state, the WLAN notch is activated. When all PIN diodes are in the ON state, the antenna acts as a normal UWB antenna. Figure 7 shows the simulated and measured VSWR of antenna when all PIN diodes are in the ON state.

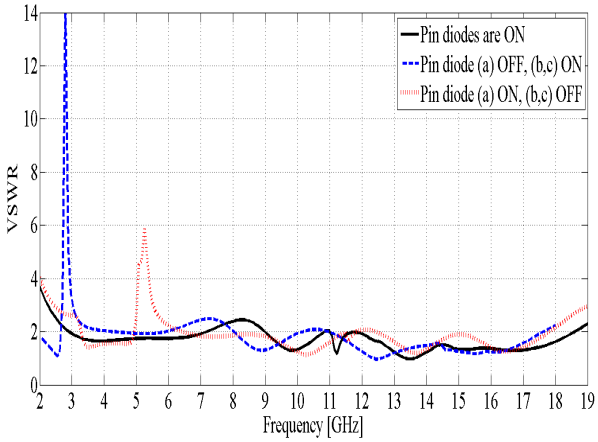

Fig. 6. Simulated VSWR for the antenna with and without band-notched function.

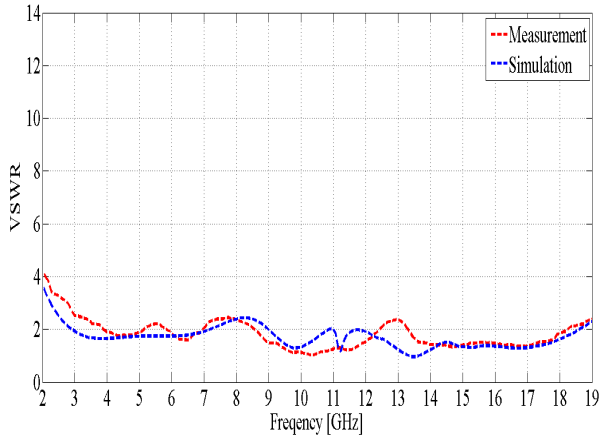

Fig. 7. Simulated and measured VSWR of the proposed antenna without band-notched function.

Figure 8 shows the variation of gain in dBi of the UWB antenna as a function of frequency under two conditions: i.e., with and without band-notch functionality. It is clear that there is sharp dip in the gain at around 3.5 GHz and 5.3 GHz, which confirms the effective operation of the dual band-notch UWB antenna. The gain generally increases with increasing frequency. The normalized radiation pattern of proposed antenna at various spot frequencies is shown in Fig. 9. The antenna's patterns are obtained when all of the PIN diodes are in the OFF state, when the antenna response operates in its dual notch-band mode. Two of the radiation patterns shown are at the center frequency of the notched bands; i.e., 3.5 GHz and 5.5 GHz, which shows suppressed radiation in the desired stop-bands due to the fact that the co- and cross-polarization pattern is near to each other in both E- and H-Plane that disturb the radiation pattern of the antenna, thus mitigating interference with WiMax and WLAN signals. Also shown is radiation pattern at 4.5 GHz, which is between the two-notched bands, where the antenna shows the distinctive difference between co- and cross-polarization levels for both H- and E-plane. At this frequency, the antenna is partially bidirectional in the E-plane and omni-directional in the H-plane. The final radiation pattern at 9 GHz demonstrates good gain performance at high frequency of antenna's operation.

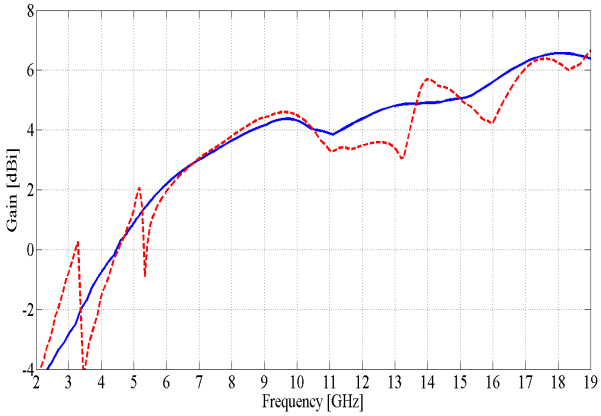

Fig. 8. Simulated Gain for the antenna with and without band-notched.

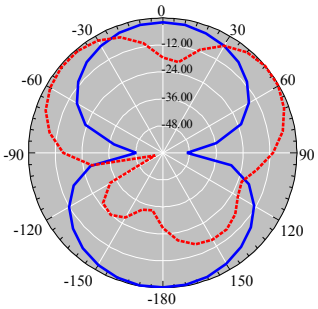

(a) E-Plane

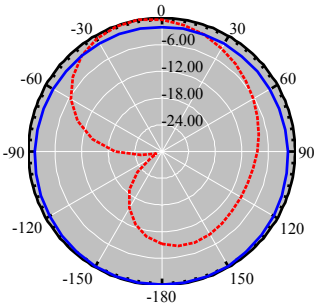

(b) H-Plane

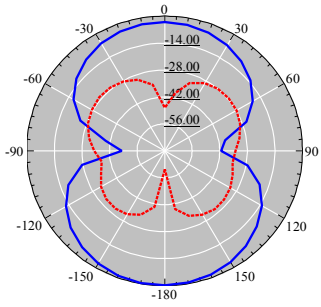

(c) E-Plane

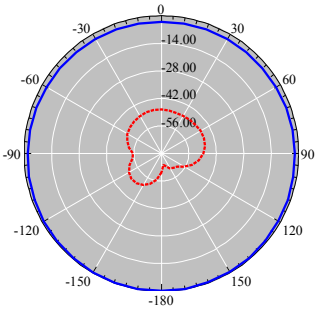

(d) H-Plane

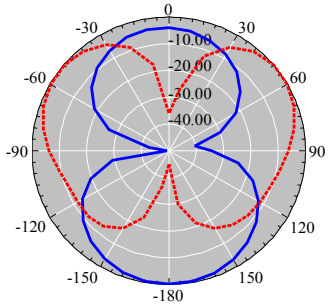

(e) E-Plane

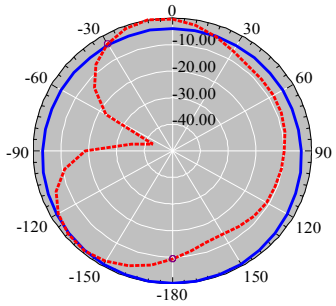

(f) H-Plane

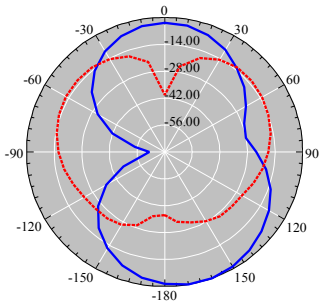

(g) E-Plane

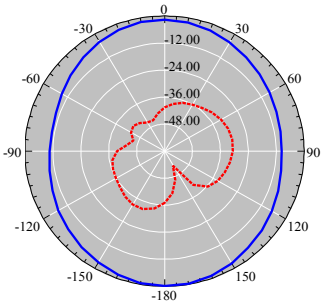

(h) H-Plane

Co-polar:
Cross-polar:

Fig. 9. E-Plane and H-plane of radiation patterns of proposed antenna: (a,b) at 3.5 GHz (central frequency of first notched band), (c,d) at 4.5 GHz (antenna operating frequency between first and second notched band), (e,f) at 5.5 GHz (central frequency of second notched band), and (g,h) at 9 GHz.

IV. CONCLUSION

A compact UWB antenna with band-notch characteristics is presented. The notch bands were obtained by embedding an inverted open-loop triangular shaped slot of varying width in the hexagonal radiating patch, and open-end resonator structures on both side of the patch. The open-end resonator structures also enhance the impedance bandwidth of the antenna. The central frequency of the notch bands were implemented at 3.5 GHz and 5.5 GHz corresponding to WiMax and WLAN bands. PIN diodes mounted across the slot and between the open-end resonator and patch enables reconfigurable functionality. The notch bands can be activated by switching the PIN diodes either 'on' or 'off' to eliminate the interfering effects of WiMax and WLAN signals. This is achieved without compromising the antenna's overall performance. The proposed antenna has a compact size of 18.4×21 mm^2 and provides omni-directional radiation pattern across the entire UWB bandwidth. The excellent features of the proposed antenna make it suitable for application in UWB systems.

REFERENCES

[1] *FCC*, "First report and order on ultra-wideband technology," 2002.

[2] N. Agrawall, G. Kumar, and K. Ray, "Wideband planar antennas," *IEEE Trans. Antennas Propag.*, vol. 46, no. 2, pp. 294-295, 1998.

[3] S. Suh, W. Stutzman, and W. Davis, "A new ultra wideband printed monopole antenna: the planar inverted cone antenna (PICA)," *IEEE Trans. Antennas Propag.*, vol. 52, no. 5, pp. 1361-1364, 2004.

[4] Y. Ge, K. P. Esselle, and T. S. Bird, "A compact E-shaped patch antenna with corrugated wings," *IEEE Trans. on Antennas and Propagation*, vol. 54, no. 8, pp. 2411-2413, August 2006.

[5] C. H. Wu and K. L. Wong, "Printed compact S-shaped monopole antenna with a perpendicular feed for penta-band mobile phone application," *Microwave and Optical Technology Letters*, vol.

49, no. 12, December 2007.

[6] M. Naser-Moghadasi, L. Asadpor, R. Sadeghzadeh, and B. S. Virdee, "A compact CPW-fed UWB monopole antenna and bifurcated antenna with a variable notching frequency," *Microwave and Optical Technology Lett*., vol. 52, no. 7, July 2010.

[7] J. Jiao, H. W. Deng, and Y. J. Zhao, "Compact ultra-wideband CPW monopole antenna with dual band notched," *Antennas Propagation and EM Theory*, pp. 263-266, November 2008.

[8] B. Ahmadi and R. Faraji-Dana, "A miniaturized monopole antenna for ultra-wideband applications with band-notch filters," *IET Microw. Antenna Propag*., vol. 3, iss 8, pp. 1224-1231, 2009.

[9] Y. F. Weng, S. W. Cheung, and T. I Yuk, "Ultra-wideband antenna using CPW resonators for dual-band notched characteristic," *IEEE, Wireless Communications & Signal Processing*, pp. 1-4, November 2009.

[10] Y. Gao, B. L. Ooi, and A. P. Popov, "Band-notched ultra-wideband ring-monopole antenna," *Microw. Opt. Technol. Lett*., vol. 48, no. 1, pp. 125-126, January 2006.

[11] M. Naser-Moghadasi, S. Faraji Gotolo, and N. Bayat Maku, "Switchable double band-notch ultra wideband monopole antenna," *IEICE Electronics Express*, vol. 8, no. 16, pp. 1315-1321, August 25, 2011.

[12] Y. Li, W. Li, and W. Yu, "A switchable UWB slot antenna using SIS-HSIR and SIS-SIR for multi-mode wireless communications applications," *ACES Journal*, vol. 27, no. 4, April 2012.

[13] K. H. Kim, Y. J. Cho, S. H. Hwang, and S. O. Park, "Band-notched UWB planar monopole antenna with two parasitic patches," *Electron. Lett*., vol. 41, no. 14, July 2005.

[14] Z. N. Low, J. H. Cheong, and C. L. Law, "Low-cost PCB antenna for UWB applications," *IEEE Antennas Wireless Propag. Lett*., 4, pp. 237-239, 2005.

[15] C. M. Leea, T. C. Yoa, C. H. Luoa, W. S. Chenb, C. H. Tuc, and Y. Z. Juangc, "Ultra-wideband printed disk monopole antenna with dual-band notched functions," *IEEE Wireless and Microwave Technology Conference*, pp. 1-4, December 2006.

[16] J. R. Verbiest and G. A. E. Vandenbosch, "A novel small-size printed tapered monopole antenna for UWB WBAN," *IEEE Antenna Wireless Propag. Lett*., 5, pp. 377-379, December 2006.

Mohammad Naser-Moghadasi was born in Saveh, Iran, in 1959. He received his B.Sc. degree in Communication Eng. in 1985 from the Leeds Metropolitan University (formerly Leeds Polytechnic), UK. Between 1985 and 1987, he worked as an RF Design Engineer for the Gigatech Company in Newcastle Upon Tyne, UK. From 1987 to 1989, he was awarded a full scholarship by the Leeds Educational Authority to pursue an M.Phil., studying in CAD of Microwave circuits. He received his Ph.D. in 1993, from the University of Bradford, UK. He was offered then a two year Post Doc. to pursue research on Microwave cooking of materials at the University of Nottingham, UK. From 1995, Naser-Moghadasi joined Islamic Azad University, Science & Research Branch, Iran, where he currently is an Associate Professor and Head of Postgraduate Studies. His main areas of interest in research are Microstrip antenna, Microwave passive and active circuits, RF MEMS. Naser-Moghadasi is member of the Institution of Engineering and Technology, MIET and the Institute of Electronics, Information and Communication Engineers (IEICE). He has so far published over 140 papers in different journals and conferences.

Sajjad Faraji was born in Urmiah, Iran. He received his M.Sc. degree in Electrical Engineering from Srbiau University in 2010, and now he is at present finishing his Ph.D. studies in Telecommunication Engineering from Srbiau University, Tehran, Iran. He has been a Scholar in the mmw Communication Laboratory, since 2010. His research interests and activities include the planner and reflectarray antennas, wave propagation, microstrip filters and passive microwave devices.

FDTD-Based Time Reversal Detection for Multiple Targets or Moving Object

Lei Zhong, Rui Zang, and Jing-Song Hong

School of Physical Electronics
University of Electronic Science and Technology of China, Chengdu, 610054, China
albertzhonglei@163.com

Abstract ─ Based on the Finite-Difference Time-Domain (FDTD) method, this paper presents a novel Time Reversal (TR) algorithm for multiple targets or moving object detection. Two numerical experiments are carried out by the Finite-Difference Time-Domain (FDTD) programs. The results confirm that the proposed TR algorithm could detect multiple targets effectively and track the moving object accurately. The re-focusing waves are very similar with the excitation signal, which can be applied in communications.

Index Terms ─ FDTD, moving object, multiple targets, time reversal detection.

I. INTRODUCTION

The time-reversal technique was introduced to acoustics by Fink in 1992, which has been applied successfully for target imaging, underwater communication and nondestructive testing [1]. Then TR technique was transposed to electromagnetism [2,3]. Due to its spatial-temporal focusing, TR technique is believed to improve the performance of current microwave systems [4]. Time-Reversal Mirror (TRM) is the key component in a TR system, which is used to reverse electromagnetic wave in time domain [5]. TRM usually consists of a transmitter-receiver array and a time reversal device.

In recent years, microwave detection has been exhaustively analyzed and experimentally researched, which may be widely applied in tomography [6], cancer treatment [7,8] and ultra-wideband radar technique [9,10]. Microwave detection can be achieved by a variety of methods, such as FDTD method [11], the Iterative Time Reversal Mirror (ITRM) [12], the Decomposition of the Time Reversal Operator (DORT, the French abbreviation of 'Décomposition de l' opérateur de retournement temporal') [13], and the Time Reversal Multiple Signal Classification (MUSIC) [14]. TR algorithms based on the Transmission-Line Method (TLM) have also been proposed [2,15]. Among these methods, FDTD is the most accurate and simplest one. Therefore, FDTD method is adopted in this paper.

In existing investigations, most TR FDTD algorithms for detection have only considered one target [7-9,16]. This paper investigates the TR FDTD algorithm for multiple targets and also uses it to track a moving object. This algorithm can precisely detect and localize the targets. Additionally, this paper has qualitatively analyzed the factors which may influence the spatial-temporal focusing.

II. TIME REVERSAL TECHNIQUES

The time-symmetry of wave propagation is the basis of TR technique [17]. In a linear, homogeneous, isotropic, and time-invariant medium without a source, the electric-field intensity E(r, t) can be described by the following vector wave equation:

$$\nabla^2 \boldsymbol{E}(\boldsymbol{r},t) - \mu\varepsilon \frac{\partial^2 \boldsymbol{E}(\boldsymbol{r},t)}{\partial t^2} = 0 . \qquad (1)$$

Equation (1) does not contain any time-varying coefficient nor the odd derivation of time, which is so-called time-symmetry of wave equation. In other words, if E(r, t) is a solution of the vector wave equation, its time reversed mode E(r, -t) is also a solution of equation (1). Furthermore, E(r, T-t) is also a solution of the wave equation.

Submitted On: May 17, 2013
Accepted On: September 5, 2014

A typical schematic of TR process is shown in Fig. 1. Firstly, a source emits a wave front which propagates through a complex medium and is received by the TRM [5,16]. Then, the received signal is time-reversed and retransmitted by the TRM. The time-reversed electromagnetic field back-propagates, and a spatial-temporal focusing can be observed at the initial position exactly. So TR is an adaptive waveform transmission scheme that utilizes the rich scattering medium to best match to the target response.

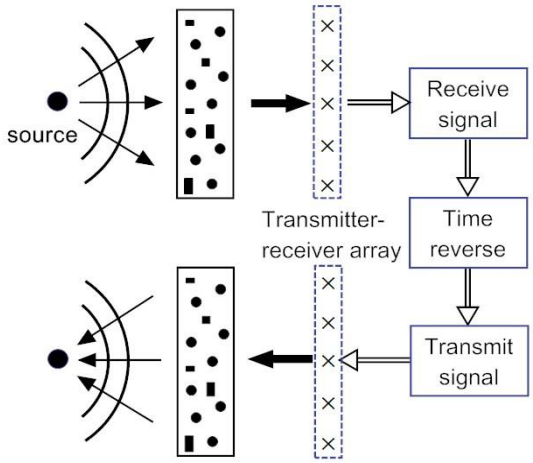

Fig. 1. Typical process of TR.

III. FDTD SIMULATION MODEL

A simplified Two-Dimension (2D) lossless indoor space model is used to carry out FDTD simulations (see Fig. 2). The propagation in this model is described by TMz mode consisting of Hx, Hy and Ez, which means the magnetic fields (Hx and Hy) are orthogonal to the normal to the plane of propagation.

The simulation model is a 3 m * 3 m indoor space, which is surrounded by three concrete walls (10-cm-thick, permittivity εr=6.4), a Perfect Electric Conductor (PEC) door and a glass window (permittivity εr=3.7). There are three PEC boxes, one PEC round table, one glass box and one wood desk (permittivity εr=7.6) in the room. The circles on the left are three targets, and the five diamonds on the right represent the TRM of five transmitter-receivers with space of 0.5 m. To verify the accuracy of the TR FDTD algorithm, the positions of targets and TRM are fixed before the simulation.

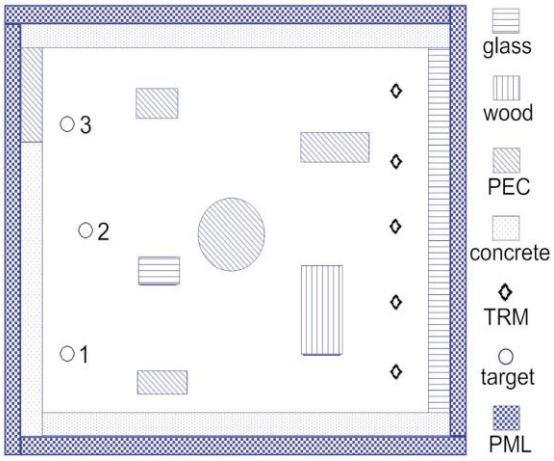

Fig. 2. Simplified 2D lossless indoor space model.

The size of FDTD grid cell is 12.5 mm * 12.5 mm. A split-field Perfectly Matched Layer (PML) is set outside the walls and window to absorb outgoing waves [18]. The PML has a thickness of 8 cells. The order of the PML parameter npml is 2, and the theoretical reflection coefficient R(0) is 10-5. The excitation signal is a second-order Gaussian pulse with a center frequency of 2.4 GHz, and a bandwidth of 1 GHz (see Fig. 3). The problem is run for 1,200 time steps.

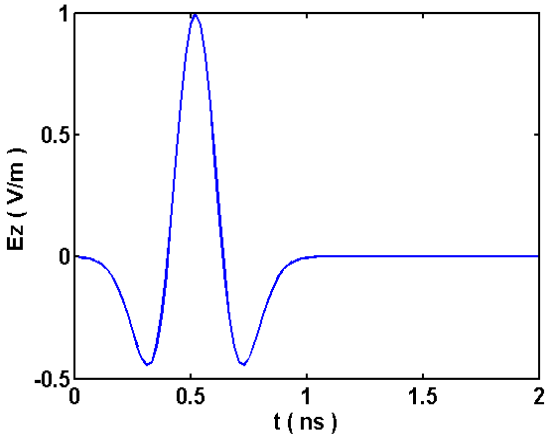

Fig. 3. The second-order Gaussian pulse.

For simplicity, the media are lossless, and specific antenna elements are not modeled. Therefore, a target is an ideal isotropic point source assigned an electric field Ez, and an observation point represents a receiving antenna of TRM.

As FDTD is performed directly in time domain, in order to get the best TR image, it is very important to determine the optimal time instant when the TR electromagnetic wave focuses back to the targets. Due to the spatial focusing property of TR, the best image of targets is expected to have some sharp peaks at the target locations and small value elsewhere. That is, the best image has minimum entropy. Therefore, a minimum entropy criterion is adopted to choose the optimal time instant. As the inverse varimax norm is known to be an easily computable and accurate approximation to entropy [19], we use the inverse varimax norm S instead of entropy, which can be calculated by:

$$S(E_z^n) = \frac{\left\{\sum_i \sum_j \left[E_z^n(i,j)\right]^2\right\}^2}{\sum_i \sum_j \left[E_z^n(i,j)\right]^4}, \qquad (2)$$

where (i, j) are the grid cell coordinates, n is the time step of FDTD, and summation is over all the grids of room. We can calculate the inverse varimax norm at every time step and find out the minimal one. Then we get the best TR image of targets and its corresponding time instant.

IV. RESULTS AND DISSCUSSSION

In this section, two numerical examples are provided to demonstrate the performance of TR FDTD algorithm under various conditions. The FDTD codes written by ourselves are calculated in MATLAB.

A. Detection and localization for multiple targets

To simulate this situation, three targets at different locations are excited by the identical second-order Gaussian pulse (see Fig. 3) at the same time. The waves travel through the multi-path environment and arrive at the TRM. Then the signals received by the TRM are normalized, time reversed and transmitted (see Fig. 4).

According to the minimum entropy criterion mentioned in Section III, the best image of targets is obtained at time step of 976 (t=20.33 ns), which is shown as Fig. 5. We can observe three targets clearly in the image. These three targets locate exactly at the same position respectively as shown in Fig. 2, which means that with TR FDTD algorithm we can precisely detect and localize multiple targets.

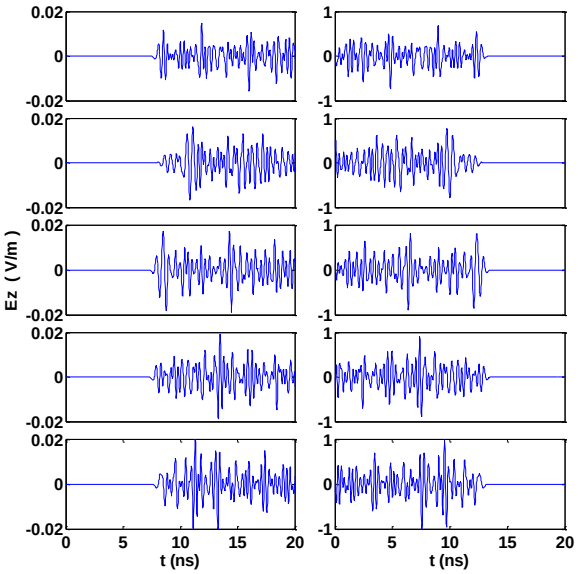

Fig. 4. Received and transmitted signals of TRM: (a) five signals received by TRM, and (b) normalized time reversed signals.

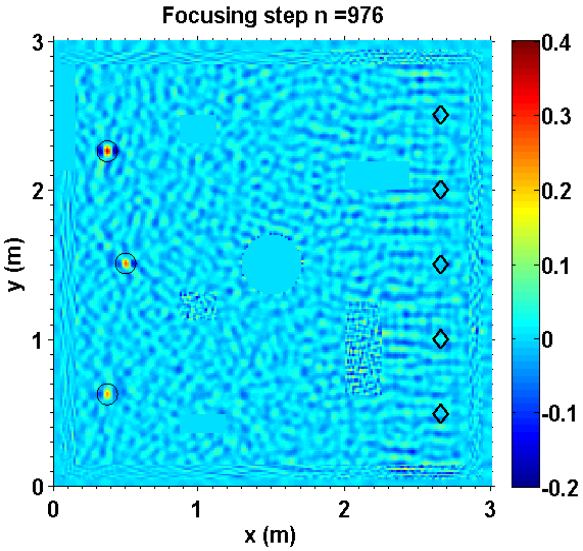

Fig. 5. Locations of three targets.

Figure 6 illustrates the time domain waveforms of the re-focused wave at three target locations. Although three targets emit the excitation pulse with the same amplitude, the amplitudes of re-focused waves are different,

because TRM receives different amounts of energy from different targets. Generally, the more energy TRM received, the higher amplitude of the re-focused wave is obtained at the corresponding target location.

Three re-focused waveforms are very similar with the excitation signal. Theoretically, the re-focused waveform is the time reversed second-order Gaussian pulse. However, the second-order Gaussian pulse is center symmetric about the peak in time domain. Therefore, the time reversed second-order Gaussian pulse is the same with the original one.

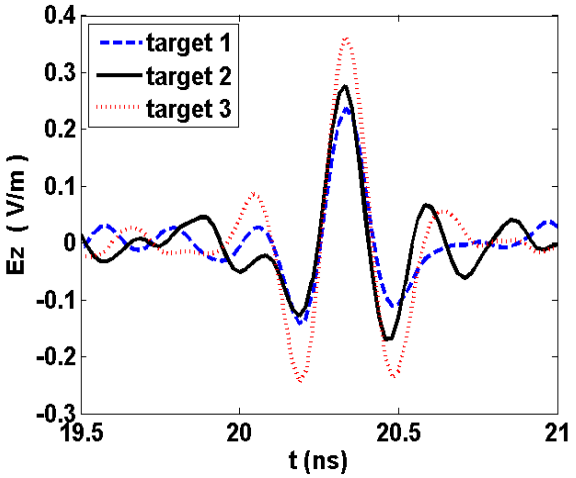

Fig. 6. The re-focused waveforms in time domain at three target locations.

B. Detection and localization for moving object

To imitate the movement of one target, target is excited from location 1 to location 3 with excitation 1 to 3 correspondingly. The excitation signals are second-order Gaussian pulses with different time delays (see Fig. 7).

Three re-focusing time steps need to be determined in this application, which means to find each minimum inverse varimax norm of three re-focused waves. However, for each re-focused waveform, the inverse varimax norm at re-focusing time step is only a little smaller than those around the re-focusing time steps. Therefore, a time gating with 0.5 ns width is adopted to avoid choosing two or more time steps from the same re-focused waveform.

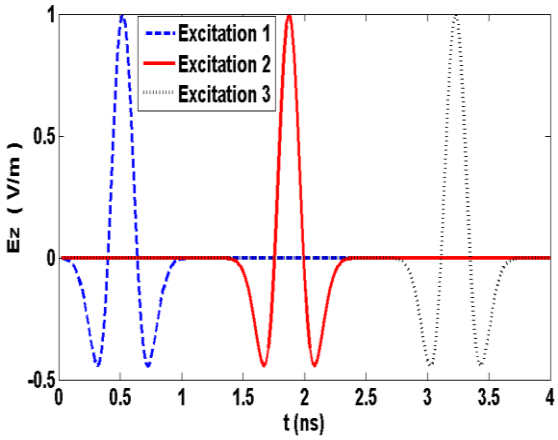

Fig. 7. Second-order Gaussian pulses with different time delays.

Figure 8 illustrates the received and transmitted signals of TRM.

The track of a moving object in TR FDTD algorithm is shown as Fig. 9. Three time instants when the TR electromagnetic wave focuses back to the target locations are time step of 846, 911 and 976, whose corresponding time is 17.63 ns, 18.98 ns and 20.33 ns.

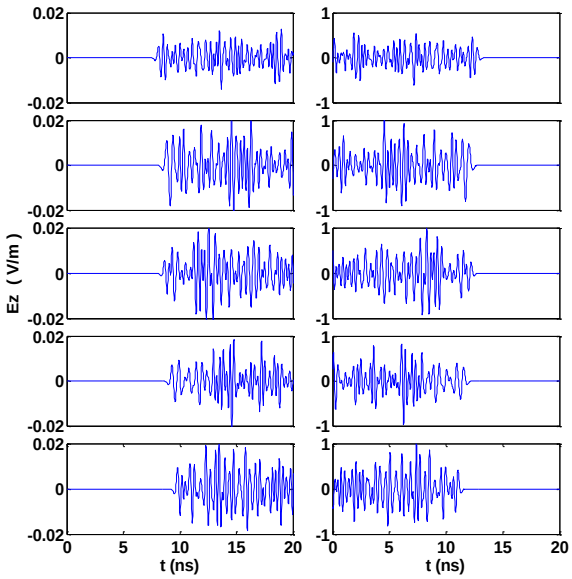

(a) (b)

Fig. 8. Received and transmitted signals of TRM: (a) five signals received by TRM, and (b) normalized time reversed signals.

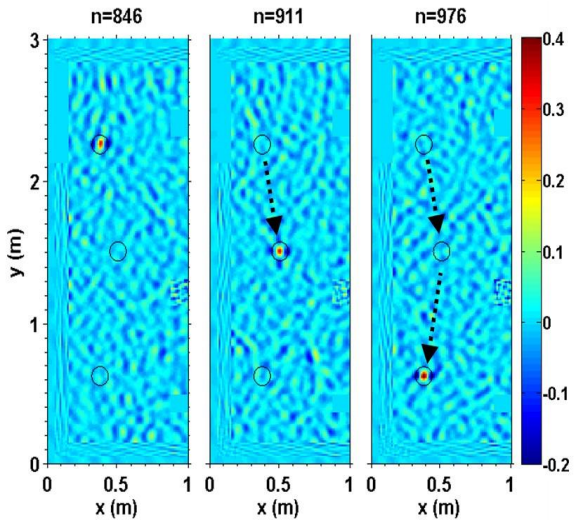

Fig. 9. Track of the moving object in TR FDTD algorithm: (a) first re-focusing image at time step of 846, (b) second re-focusing image at time step of 911, and (c) third re-focusing image at time step of 976.

Figure 10 illustrates the re-focused waves at three locations, which is very similar to the excitation signals in Fig. 7. From location 3 to location 1, the TR wave focuses sequentially at 17.63 ns, 18.98 ns and 20.33 ns respectively, which agree well with Fig. 9. Besides, the amplitude of re-focused wave at location 1 is largest, because target is first excited at location 1 with excitation 1. Compared with other excitations, the reflected and scattered waves of excitation 1 could travel more times to and from the TRM, which means the TRM receives maximum amount of energy from location 1.

It is important to notice that the focusing time sequence of TR wave is just in reverse order of exciting time sequence. That is, the TR wave would focus last at the location excited first. Therefore, to describe the movement accurately in the time domain, the image of TR FDTD algorithm should be time reversed again. So based on the Fig. 9, we can finally obtain both the real track of the moving object and the time differences between adjacent locations, which is shown as Fig. 11.

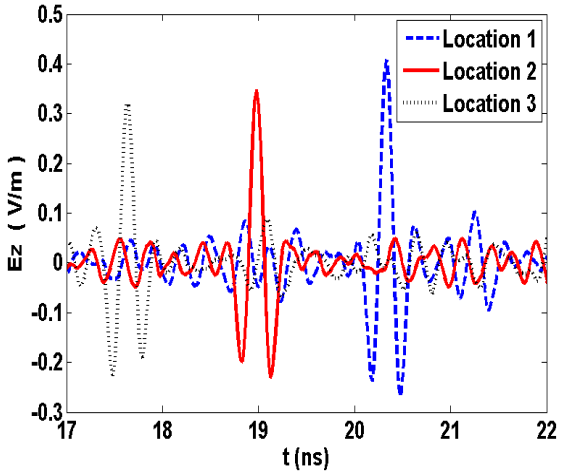

Fig. 10. The re-focused waveforms in time domain at three locations.

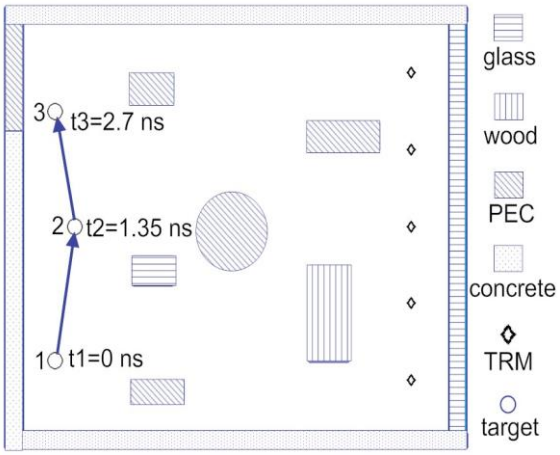

Fig. 11. Real track of the moving object.

V. CONCLUSION

Based on a simplified lossless indoor space model, this paper has presented a TR FDTD algorithm to detect and localize for multiple targets or moving object. The imaging results demonstrate the effectiveness of the proposed TR FDTD algorithm in the complex environment. As the TR technique is based on time-symmetry, the proposed algorithm is also available for lossy medium or reciprocal environment. However, because of big FDTD calculation amount or the failure of minimum entropy criterion, it is not the best choice for some scenarios, such as very large

detecting space, non-reciprocal or high target density environment. Therefore, the TR FDTD algorithm proposed in this paper can be widely applied in indoor location and tracking, short range communications in complex scattering environment and self-adaptive Wireless Power Transmission (WPT) system.

ACKNOWLEDGMENT

This work was supported partially by the National Science Foundation of China (No. 60872029 and No. 60872034), partially by the High-Tech Research and Development Program of China (No. 2008AA01Z206), partially by the Aeronautics Foundation of China (No. 2010018003), and partially by the Fundamental Research Founds for the Central Universities (No. ZYGX 2009J037).

REFERENCES

[1] M. Fink, "Time reversal of ultrasonic fields-part I: basic principles," *IEEE Trans. on Ultrasonics, Ferroelectrics, and Frequency Control*, vol. 36, no. 5, pp. 555-565, 1992.

[2] R. Sorrentino, P. P. M. So, and W. J. R. Hoefer, "Numerical microwave synthesis by inversion of the TLM process," *21st European Microwave Conference*, Stuttgart, Germany, pp. 1273-1277, 1991.

[3] G. Lerosey, J. de Rosny, A. Tourin, A. Derode, G. Montaldo, and M. Fink, "Time reversal of electromagnetic waves," *Physical Review Letters*, vol. 92, 193904, 2004.

[4] G. Lerosey, J. de Rosny, A. Tourin, A. Derode, G. Montaldo, and M. Fink, "Focusing beyond the diffraction limit with far-field time reversal," *Science*, vol. 315, no. 5815, pp. 1120-1122, 2007.

[5] J. de Rosny, G. Lerosey, and M. Fink, "Theory of electromagnetic time-reversal mirrors," *IEEE Trans. Antennas Propag.*, vol. 58, no. 10, pp. 3139-3149, October 2010.

[6] P. M. Meaney, M. W. Fanning, D. Li, S. P. Poplack, and K. D. Paulsen, "A clinical prototype for active microwave imaging of the breast," *IEEE Trans. Microw. Theory Tech.*, vol. 48, pp. 1841-1853, November 2000.

[7] P. Kosmas and C. M. Rappaport, "Time reversal with the FDTD method for microwave breast cancer detection," *IEEE Trans. Microw. Theory Tech.*, vol. 53, pp. 2317-2323, July 2005.

[8] P. Kosmas and C. M. Rappaport, "FDTD-based time reversal for microwave breast cancer detection-localization in three dimensions," *IEEE Trans. Microw. Theory Tech.*, vol. 54, pp. 1921-1927, April 2006.

[9] Y. Jin, J. Moura, and N. Donoughue, "Time reversal in multiple-input multiple-output radar," *IEEE Journal of Selected Topics in Signal Processing*, vol. 4, no. 1, pp. 210-225, February 2010.

[10] F. Foroozan and A. Asif, "Time-reversal ground-penetrating radar: range estimation with cramér-rao lower bounds," *IEEE Trans. Geosci. Remote Sens.*, vol. 48, no. 10, pp. 3698-3708, October 2010.

[11] A. Taflove and S. C. Hagness, "Computational electrodynamics: the finite-difference time-domain method," *MA: Artech House*, Boston, 2000.

[12] C. Prada, J. L. Thomas, and M. Fink, "Theory of iterative time reversal acoustic mirrors," *J. Acoust. Soc. Am.*, 91: 2326, 1992.

[13] C. Prada, S. Manneville, D. Spoliansky, and M. Fink, "Decomposition of the time reversal operator: detection and selective focusing on two scatterers," *J. Acoust. Soc. Am.*, 99: 2067-2076, 1996.

[14] E. A. Marengo, F. K. Gruber, and F. Simonetti, "Time-reversal MUSIC imaging of extended targets," *IEEE Trans. Image Processing*, vol. 16, no. 8, pp. 1967-1984, 2007.

[15] W. J. R. Hoefer and M. Forest, "TLM modelling of electromagnetic scattering in forward and inverse time sequence," *Proceedings of ISAP `92*, Sapporo, Japan, pp. 733-736, 1992.

[16] P. Kosmas and C. M. Rappaport, "A matched-filter FDTD-based time reversal approach for microwave breast cancer detection," *IEEE Trans. Antennas Propag.*, vol. 54, no. 4, pp. 1257-1264, April 2006.

[17] R. F. Harrington, "Time-harmonic electromagnetic fields," *MA: Artech House*, Boston, 2000.

[18] J. P. Berenger, "A perfectly matched layer for the absorption of electromagnetic waves," *Journal of Computational Physics*, vol. 114, no. 2, pp. 185-200, 1994.

[19] X. Xu, E. L. Miller, and C. M. Rappaport, "Minimum entropy regularization in frequency-wavenumber migration to localize subsurface objects," *IEEE Trans. Geosci. Remote Sens.*, vol. 41, no. 8, pp. 1804-1812, August 2003.

An Investigation of a Wearable Antenna Using Human Body Modelling

Esther S. Florence [1], Malathi Kanagasabai [2], and Gulam Nabi M. Alsath [1]

[1] Department of Electronics and Communication Engineering
SSN College of Engineering, Kalavakkam, Chennai, 603110, India
estherflorences@ssn.edu.in, mail.alsath@yahoo.com

[2] Department of Electronics and Communication Engineering
College of Engineering, Guindy, Anna University, Chennai, 600025, India
mala@annauniv.edu

Abstract ― The work presented is an assay done on the effects of wearable antenna when placed in proximity to the human body. Cloth fabric is used as a substrate to design a planar antenna. Measurement results of the fabricated patch at free space and close to the human body are also presented here. The S_{11} of the designed antenna when placed close to the body tissue is almost -30 dB and the gain is close to 4 dB. A rectangular three layered human body model is used to evaluate the extent of the effect that the human body has on the parameters that define an antenna like its gain, directivity, etc.

Index Terms ― Fabric substrate, Specific Absorption Rate (SAR), Wearable Antenna.

I. INTRODUCTION

The use of fabric as a substrate material for antennas has gained recent notice. Using the fabric in such a manner would provide the much pursued integration of antenna with clothing. To this end, a study on the effect of the human body on a simple patch, fabricated on a jean cloth is presented here. The results analyzed in this paper would aid in designing textile antennas, giving the best possible position on the human body without compromise on its performance.

Bending characteristics of antenna on a flexible substrate of a simple wearable antenna was previously analyzed [1]. The effect of varying distance of wearable antenna from the human body on the antenna parameters has also been done [2]. The use of wearable antenna for the purpose of medical monitoring has also been studied recently. The challenge of designing wearable antennas is still high and a surprising interest in the area has been noticed in recent months. A button wearable antenna and an L shape Planar Inverted F Antenna (PIFA) have been designed for medical e-Health system [3]. An Ultra-Wideband (UWB) printed antenna for wearable applications to monitor cardiac activity has been reported [4].

In another design for medical application wearable antenna that can be integrated with EKG sensors have been proposed [5]. The effect of ground plane on the efficiency of a wearable antenna is studied in [6], while [7] examines the effect of varying textiles on the antenna's performance. Analysis on the effect of bending on a wearable dipole patch is done in [8]. Research on the study of the feasibility and reliability of wearable antennas is still underway.

According to [9], "characterization of antennas is the key to establishing reliable on-body data transmission between sensors and the main data-collecting node (this may be worn on-body or an external stationary or mobile unit)." Hence, there is an immense need for characterizing the antenna and its performance when in the vicinity of the human body so that it can be used for wearable applications.

This paper puts forward a clear evaluation of the effect of the human body on the parameters that define an antenna. In order to design an on-

Submitted On: March 11, 2013
Accepted On: September 5, 2014

body wearable antenna, a fabric whose permittivity is known, can be used as the substrate material.

Major attraction of these wearable antennas would be its use in defense. It would serve to reduce to a great extent, the paraphernalia carried by soldiers, thus improving mobility of the troop. The implementation of wearable antennas can also provide medical monitoring of patients with chronic illness as they go about their daily chores. It could also be tweaked to help monitor patients with psychological disorders. Antenna if integrated onto the clothing of an individual would provide unrestricted movement and obviate the need to carry around large antenna.

II. WEARABLE PATCH DESIGN

A simple rectangular patch was designed for an operating frequency of 2.45 GHz using the transmission line model equations [10]. The height of the substrate is taken as 1 mm (normal thickness of jean fabric). The relative permittivity of the jean fabric at 2.45 GHz is 1.67 and permeability of 1.

Dimensions calculated according to the transmission line model [10]: length of the patch is 44.35 mm, width is 53 mm. The patch excited by a 50 Ω transmission line of length λ/4. Jean fabric that is 1 mm thick is used as the substrate. A square 120 x 120 mm^2 ground plane made of copper is also used for this design. The thickness of the ground plane and the patch is 0.035 mm. The antenna is simulated using CST Microwave Studio. The snapshot of the designed antenna is given in Fig. 1.

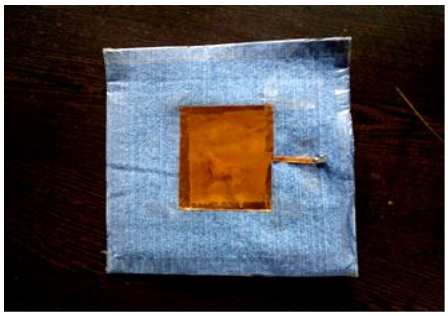

Fig. 1. A wearable patch antenna designed on a jean cloth fabric and excited by a transmission line feed.

A parametric sweep reveals that for different values of denim as found from literature, there is little variation in the frequency of patch with only a slight mismatch occurring due to the dimensions of the patch, and the feed point kept constant. Hence, we have chosen 1.67 as the dielectric constant in our study. Agilent Vector Network Analyser was used for the measurement of return loss of the antenna in free space. Measurement setup for the wearable antenna is shown in Fig. 2.

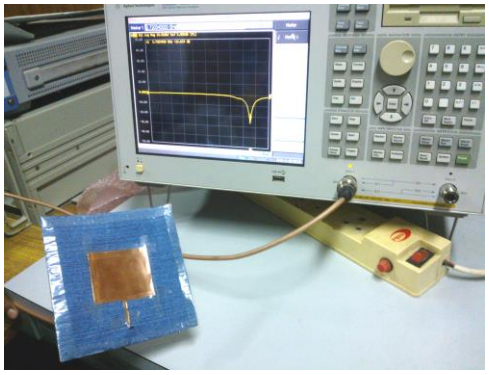

Fig. 2. The measurement setup for measurement of antenna parameter in free space.

Results obtained from measurement are compared to those obtained through simulation in Fig. 3. A slight shift in frequency in the simulated and measured results of the return loss of the antenna when placed in free space is observed. Utilizing accurate and appropriate fabrication methods, the deviation in the frequency could be reduced to a great extent. However, there is a good agreement in the return loss of the patch simulated and measured, which is observed to be 20.62 dB during simulation and 20.9 dB when measured.

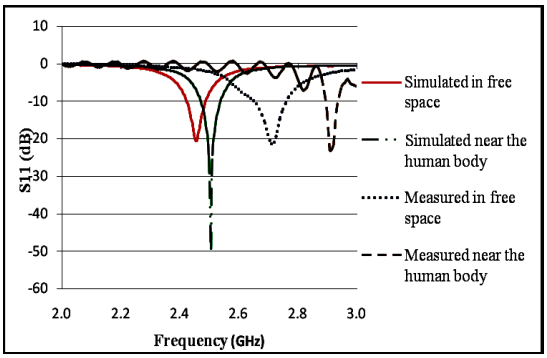

Fig. 3. The plot of S_{11} versus frequency for the designed wearable antenna, near and away from the human body.

By the use of better-suited fabrication methods, exact performance can easily be obtained. This is an issue that would require further improvement. The actual dimension of the patch length measured is approximately 40.1 mm, which when simulated shows a resonant frequency of 2.697 GHz while measured is at 2.72 GHz. Figure 4 shows the simulated radiation pattern in the vicinity of the body model.

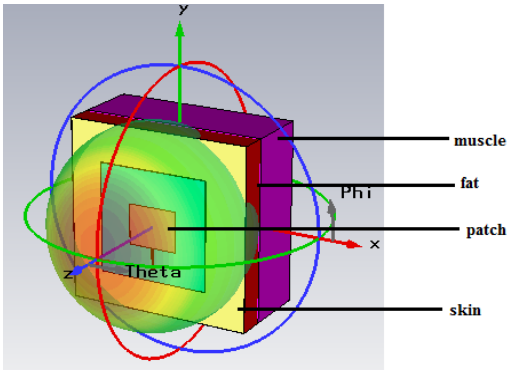

Fig. 4. Simulated radiation pattern in the vicinity of the body model.

III. SAR ASSESSMENT AND BODY EFFECTS DUE TO WEARABLE ANTENNA

A. Human body modelling

Since the application of wearable antennas necessitates it to function in close proximity to the human body, we need to assess the parameter changes in the antenna when working in such an environment [11]. To find the amount of electromagnetic radiation captured by the tissues in the body, evaluation of the Specific Absorption Rate (SAR) becomes necessary. SAR is a measure of the rate at which energy is absorbed by the body when exposed to the Radio Frequency (RF) electromagnetic field. It can also refer to the absorption of other forms of energy by tissue, including ultrasound. It is expressed as the power absorbed per mass of tissue and has units of Watts per Kilogram (W/Kg). SAR is usually averaged either over the whole body or over a small sample volume (typically 1 gram or 10 grams of tissue).

SAR can be calculated from the electric field within the tissue as:

$$\mathrm{SAR} = \int \left(\frac{\left(\sigma(r)|E(r)|^2\right)}{\rho(r)} \right) dr, \qquad (1)$$

where σ (r) - Sample Electrical Conductivity, E - RMS Electric Field, and ρ (r) - Sample Density. SAR is directly proportional to the conductivity of the tissue absorbing the radiation and inversely proportional to its density. The maximum permissible value for SAR is 1.6 W/Kg.

Hence, a broad analysis on the Specific Absorption Rate has been done for varying distance of the antenna from the body. The readings are noted with respect to the wavelength of operation in order to better understand the analysis done.

In order to assess the SAR for varying distance we need to define body models that would replicate the presence of lossy tissue close to the antenna. Usually detailed body models, those including organs, are complicated and demands more run time while utilizing resource intensively.

In literature, there are simplified human body models like the lossy cylinder with defined dielectric constant and conductivity and the rectangular body model [12]. The rectangular model of body is chosen for our study since it was found to give excellent agreement with measurements.

In the rectangular three layered model we have considered thickness of skin is taken as 0.4 mm, thickness of fat as 30 mm, and that of muscle is 69.6 mm. The permittivity, loss tangent and density for the different tissues are as follows. Skin: εr=37.952, δ=0.28184 and density is 1050kg/m3. Fat: εr=5.2749, δ=0.14547 and density is 918kg/m3. Muscle: εr=52.73, density is 1100kg/m3. All these parameters have been defined at frequency 2.45 GHz, according to [13].

Mass averaged Specific Absorption Rate, SAR (10 g) is estimated for distances varying from 0 λ to 0.08 λ between the body tissues and the antenna. In order to fully comprehend this, defining the quantity obtained as SAR becomes necessary.

Specific absorption rate or SAR is the amount of electromagnetic radiation absorbed by the body tissues. The sample volume considered for calculation of SAR can be 1 g or 10 g. 10 g sample is appropriate for our study when considering body regions like chest, wais, etc., that would generally be the positions of these wearable antennas. SAR depends on the conductivity and density of the sample considered.

B. Analysis of the effect of the human body on the antenna

Using the rectangular human body model explained in the previous section, we perform the following analysis. To learn about the effects of the body on the antenna [14], the S_{11} variation with respect to the frequency is studied. As can be seen from the graph of the simulated S_{11} versus frequency, when the antenna is placed on the human body it experiences a frequency shift of 48 MHz from 2.457 GHz to 2.505 GHz, as shown in Fig. 3.

The measurement of the return loss of the antenna is also done by placing the antenna on the body, as shown in Fig. 5. This measurement again shows a resonant frequency shift of 190 MHz from 2.72 GHz to 2.91 GHz when the antenna is placed in the vicinity of the human body. The reason for this shift in the resonant frequency is because of the dielectric loading due to the lossy human tissue [15] which is in close proximity to the wearable patch antenna.

When kept at free space, the simulated resonant frequency was at 2.457 GHz. The gain was observed as 4.144 dB and directivity of 8.957 dBi. The variation of SAR, gain, impedance and directivity are also analyzed from simulation with varying distance from the body in terms of wavelength, as presented in Table 1. Figure 6 depicts the simulation results of SAR for varying body-antenna separation.

Another analysis, keeping the over-all thickness as 100 mm and varying the depth of each layer is presented in Table 2. Most of the areas necessitating wearable antennas would be requiring the use of antenna arrays. A 1 x 4 array was constructed and simulations were run for various layer thickness. The values are noted in Table 3.

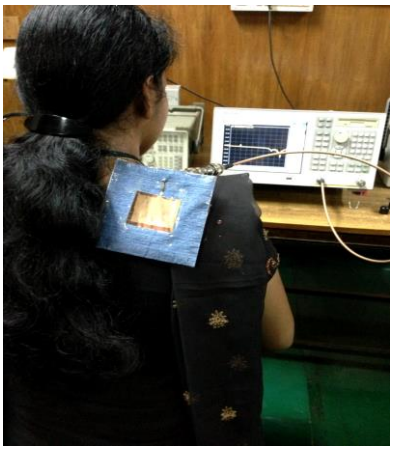

Fig. 5. Return loss measurement for antenna placed on-body.

Table 1: Table depicting the antenna parameters and SAR values for varying distance of the antenna from the body

Distance of Separation	Input Impedance (ohms)	Gain (dB)	Directivity (dBi)	SAR (W/Kg)
0λ	53.77, 0.27	3.956	8.682	0.00626
0.01λ	53.80, 0.24	3.932	8.680	0.00625
0.02λ	53.79, 0.23	3.932	8.677	0.00618
0.03λ	53.79, 0.22	3.922	8.666	0.00595
0.04λ	53.74, 0.34	3.908	8.651	0.00561
0.05λ	53.73, 0.35	3.898	8.641	0.00437
0.06λ	53.73, 0.35	3.884	8.627	0.00488
0.07λ	53.78, 0.24	3.887	8.626	0.00455

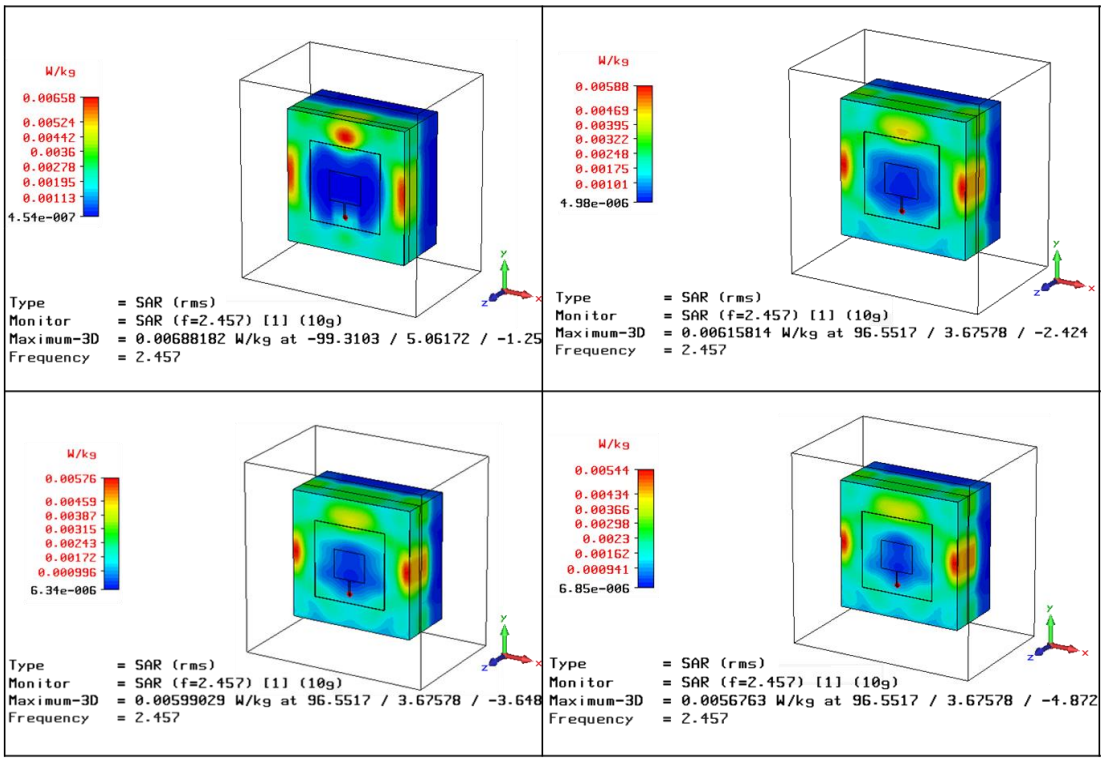

Fig. 6. Simulated SAR distribution for varying distances of the antenna from the body; 0λ, 0.01 λ, 0.02λ, and 0.03λ.

Table 2: Table depicting the parameter changes in an antenna and SAR values for varying thickness of individual layers

Varying Thickness (mm)			Input Impedance (ohms)	Gain (dB)	Directivity (dBi)	SAR (W/Kg)
Skin	Fat	Muscle				
0.4	0	99.6	53.90, 0.26	3.740	8.458	0.00659
0.4	15	84.6	53.73, 0.36	4.541	9.305	0.01005
0.4	30	69.6	53.80, 0.24	3.932	8.680	0.00625
2.6	0	97.4	53.88, 0.25	3.748	8.471	0.00669
2.6	15	82.4	53.82, 0.43	3.689	8.423	0.00831
2.6	30	67.4	53.87, 0.30	3.871	8.597	0.00719

Table 3: Table depicting the parameter changes in a 1 x 4 antenna array and SAR values for varying thickness of individual layers

Varying Thickness (mm)			Gain (dB)	Directivity (dBi)	SAR (W/Kg)
Skin	Fat	Muscle			
0.4	0	99.6	6.461	14.04	1.23789e-006
0.4	15	84.6	6.421	14.01	9.64977e-007
0.4	30	69.6	6.394	13.97	2.67269e-007
2.6	0	97.4	6.365	13.96	3.02758e-007
2.6	15	82.4	6.392	13.96	9.12359e-007
2.6	30	67.4	7.179	13.75	1.64409e-006

The frequency is at 2.505 GHz when in the vicinity of the human body, but does not show variation with respect to the distance since it is in the radiative far field of the patch. The foremost observation made from this specific study is the variation or the lack of it in the input impedance, gain and directivity for different distances from the body. Extensive literature study reveals the reason as: the boundary for the far-field region of a patch is normally so small that it would lie within the ground plane itself [16]. When the human body is near the antenna and absorbs power from the near field. By altering the reactive near field, the body affects the input impedance and other antenna parameters. In literature, as cited in [16], microstrip antennas near field maximum occurs in the gap between the element and the ground plane and the reactive near field is negligible elsewhere. Hence, the reactive near field region in microstrip antennas is much smaller than $\lambda/2\pi$.

Also, the percentage detuning by the human body given by (100*detuning)/free space frequency is 1.95 % for all distances simulated. The dielectric constant and penetration depth in the body is different for different frequencies. Hence, the detuning varies with the frequency. If we can design an antenna with a broadband characteristic such that the -10 dB impedance bandwidth encompasses the shifted frequency, the design would be acceptable. Literature has it that [16] dipoles as well as antennas working at lower frequencies have a very large percentage of detuning than microstrip antennas. This point would allow us to draw the conclusion that a patch antenna structure would be the best suitable contender for on-body wearable antennas. PIFA antennas also have a small far field, but considering the fabrication possibilities, a microstrip patch antenna scores over it with several distinct advantages. It does not require shorting, which makes its fabrication on the textile easier.

The second analysis will throw light on how different parts of the body, say, limbs, torso, etc., will impact the antenna parameters. The variation of SAR for different layer depths presents an interesting phenomenon that for a particular thickness of fat, say 15 mm, the SAR value slightly increases. A region in the human body with very less amount of fat is the best position for the placement of a wearable antenna. Say, when a jacket has a wearable antenna array, the antenna could be fabricated such that it lies at the back of the torso of the human body so that lesser radiation absorption takes place. These analyses throw light on the placement and positioning of wearable antennas when they are modeled for any particular application.

Similarly, simulation results as noted in the third analysis have revealed that for array antennas the SAR has decreased to a great extent. In an array as the pattern becomes more directive [17] and points away from the body when compared to a single patch, the SAR decreases. Hence, the conclusions drawn from this study and the insight gained can be used when larger more complicated arrays are designed.

VI. CONCLUSION

A comprehensive investigative study on the working of wearable antennas has been projected in this paper. Real time examination of the results has been demonstrated by the fabrication of a patch antenna integrated into cloth fabric.

Extensive analysis on both the effects of the antenna on the body and the effects of the human body on the antenna has been presented in detail.

REFERENCES

[1] S. Sankaralingam and B. Gupta, "Determination of dielectric constant of fabric materials and their use as substrates for design and development of antennas for wearable applications," *IEEE Transactions on Instrumentation and Measurement*, vol. 59, no. 12, December 2010.

[2] A. Alomainy, Y. Hao, and D. M. Davenport, "Parametric study of wearable antennas with varying distances from the body and different on-body positions," *2007 IET Seminar on Antennas and Propagation for Body-Centric Wireless Communications*, pp. 84-89, April 2007.

[3] W. Huang and A. A. Kishk, "Compact antenna designs for wearable and medical portable systems," *ACES Journal*, vol. 26, no. 4, April 2011.

[4] E. Pittella, P. Bernardi, M. Cavagnaro, S. Pisa, and E. Piuzzi, "Design of UWB antennas to monitor cardiac activity," *ACES Journal*, vol. 26, no. 4, April 2011.

[5] C. Kruesi, L. Yang, D. Staiculescu, M. M. Tentzeris, and M. Phelps, "Reusable wearable patch antenna for health monitoring body area sensor network," *25th Annual Review of Progress*

in Applied Computational Electromagnetics, March 8-12, 2009.

[6] H. Giddens, D. L. Paul, G. S. Hilton, and J. P. McGeehan, "Influence of body proximity on the efficiency of a wearable textile patch antenna," *6th European Conference on Antennas and Propagation (EUCAP)*, 2011.

[7] S. Sankaralingam, S. Dhar, and B. Gupta, "Preliminary studies on performance of a 2.45 GHz wearable antenna in the vicinity of human body," *2012 International Conference on Communications, Devices and Intelligent Systems (CODIS)*, pp. 250,253, December 28-29, 2012.

[8] N. A. Elias, N. A. Samsuri, M. K. A. Rahim, and N. Othman, "The effects of human body and bending on dipole textile antenna performance and SAR," *Proceedings of APMC 2012*, December 4-7, 2012.

[9] T. Yilmaz, R. Foster, and Y. Hao, "Detecting vital signs with wearable wireless sensors," *Sensors*, vol. 10, pp. 10837-10862, 2010.

[10] C. A. Balanis, "Antenna theory, analysis and design," *John-Wiley and Sons Inc.*, New York, 1997.

[11] M. A. R. Osman, M. K. A. Rahim, M. Azfar, N. A. Samsuri, F. Zubir, and K. Kamardin, "Design, implementation and performance of ultra-wideband textile antenna," *Progress In Electromagnetics Research B*, vol. 27, pp. 307-325, 2011.

[12] K. E. Wasife, "Power density and SAR in multi-layered life tissue at global system mobile (GSM) frequencies," *Journal of Electromagnetic Analysis and Applications*, vol. 3, pp. 328-332, 2011.

[13] P. S. Hall and Y. Hao, "Antennas and propagation for body-centric wireless communications," *Artech House*, Norwood, 2012.

[14] M. A. R. Osman, M. K. A. Rahim, N. A. Samsuri, H. A. M. Salim, and M. F. Ali, "Embroidered fully textile wearable antenna for medical monitoring applications," *Progress In Electromagnetics Research*, vol. 117, pp. 321-337, 2011.

[15] G. Emili and A. Schiavoni, "Computation of electromagnetic field inside a tissue at mobile communications frequencies," *IEEE Transactions on Microwave Theory and Techniques*, vol. 51, no. 1, pp. 178-186, 2003.

[16] T. Kellomaki, J. Heikkinen, and M. Kivikoski, "One layer GPS antennas perform well near a human body," *Proc. European Conference of Antennas and Propagation*, UK, November 2007.

[17] Y. Huang and K. Boyle, "Antennas from theory to practice," *Wiley Publishers*, 2008.

Esther S. Florence is working as an Assistant Professor in the department of ECE, SSN College of Engineering, Chennai. She is currently pursuing her Doctorate degree at Anna University. Her research interests include design and analysis of microwave components like antennas for multiple polarization applications, wearable applications, etc.

Malathi Kanagasabai obtained her Ph.D. degree in Microwave Engineering from College of Engineering, Guindy, Anna University, Chennai. She is currently serving as Associate Professor in the Department of ECE, College of Engineering Guindy, Anna University, Chennai. Her research interests include microwave engineering, planar transmission lines, antenna structures and signal integrity in high speed systems.

Gulam Nabi Alsath is working as an Assistant Professor in the department of ECE, SSN College of Engineering, Chennai. He is currently pursuing his Doctorate degree at Anna University. His research interests include design of reflector antennas, planar antennas, multiband antenna structures and antennas for vehicular applications.

Investigation and FDTD Analysis of UWB Microstrip Antenna with Dual Narrow Band-Notched Characteristic

Nasser Ojaroudi[1], Mehdi Mehranpour[1], Yasser Ojaroudi[2], and Sajjad Ojaroudi[2]

[1] Young Researchers and Elite Club
Islamic Azad University, Ardabil Branch, Ardabil, Iran
n.ojaroudi@yahoo.com, mehranpour.mehdi@gmail.com

[2] Young Researchers and Elite Club
Islamic Azad University, Germi Branch, Germi, Iran
y.ojaroudi@iaugermi.ac.ir, s.ojaroudi.p@yahoo.com

Abstract ─ In this manuscript, a novel design of Ultra-Wideband (UWB) monopole antenna with dual narrow band-stop performance is proposed. In this design, by using inverted T-shaped slit and T-shaped parasitic structure in the ground plane, additional resonances are excited and much wider impedance bandwidth can be produced; especially at the higher band. In order to generate single and dual band-notched characteristics, we use a pair of protruded E-shaped strips inside the square-ring radiating patch. The measured results reveal that the presented dual band-notched monopole antenna offers a very wide bandwidth form 3.01 GHz to 12.8 GHz with two narrow notched bands, covering 5.2/5.8 GHz to suppress interferences from Wireless Local Area Network (WLAN) system. To verify the validation of proposed antenna, Finite-Difference Time-Domain (FDTD) analysis is investigated. Good return loss, antenna gain and radiation pattern characteristics are obtained in the frequency band of interest. The antenna imposes negligible effects on the transmitted pulses.

Index Terms ─ Dual narrow notch bands, FDTD analysis, microstrip antenna, UWB applications.

I. INTRODUCTION

After allocation of the frequency band from 3.1 to 10.6 GHz for the commercial use of Ultra-Wideband (UWB) systems by the Federal Communication Commission (FCC) [1], UWB systems have received phenomenal gravitation in wireless communication. Designing an antenna to operate in the UWB band is quite a challenge because it has to satisfy the requirements, such as ultra wide impedance bandwidth, omni-directional radiation pattern, constant gain, high radiation efficiency, constant group delay, low profile, easy manufacturing, etc. [2]. In UWB communication systems, one of key issues is the design of a compact antenna while providing wideband characteristic over the whole operating band. Consequently, a number of microstrip antennas with different geometries have been experimentally characterized [3-6].

In [3], a compact hexagonal structure is used to enhance the impedance bandwidth. Based on Defected Ground Structure (DGS) and Electromagnetic Coupling Theory (ECT), slot and parasitic structures are used to excite more resonances in [4]. A novel CPW-fed E-shaped slot antenna which provides a wide usable fractional bandwidth of more than 115% is reported in [5]. Moreover, other strategies to improve the impedance bandwidth which do not involve a modification of the geometry of the planar antenna have been investigated [6-7].

There are many narrowband communication systems which severely interfere with the UWB communication system, such as the Wireless Local Area Network (WLAN) for IEEE 802.11a operating in 5.15-5.35 and 5.725-5.825 GHz bands. Therefore, UWB antennas with band-notched characteristic to filter the potential interference are desirable. Nowadays, to mitigate

Submitted On: February 23, 2014
Accepted On: August 25, 2014

this effect, many UWB antennas with various band-notched properties have developed [8-9].

All of the above methods are used for rejecting a single band of frequencies. However, to effectively utilize the UWB spectrum and to improve the performance of the UWB system, it is desirable to design the UWB antenna with dual band rejection. It will help to minimize the interference between the narrow band systems with the UWB system. Some methods are used to obtain the dual band rejection in the literature [10-14].

In this paper, a new design of 5.2/5.8 GHz dual narrow band-notched printed monopole antenna with multi-resonance performance is presented. The proposed antenna consists of square-ring radiating patch with a pair of protruded E-shaped strips, and modified ground plane with inverted T-shaped slit and T-shaped parasitic structure. The proposed antenna has a small size of 12×18 mm^2.

II. ANTENNA DESIGN

Configuration of the proposed monopole antenna fed by a microstrip line is shown in Fig. 1.

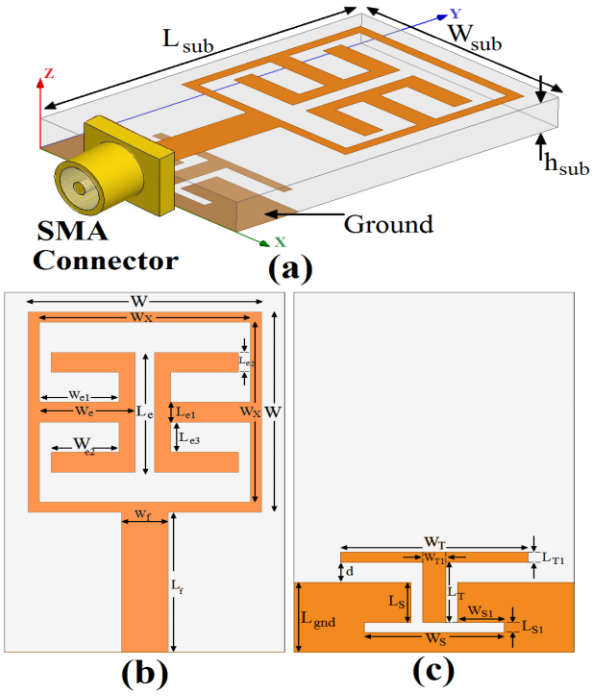

Fig. 1. Geometry of the proposed antenna: (a) side view, (b) top layer, and (c) bottom layer.

The dielectric substance (*FR4*) with thickness of 1.6 mm with relative permittivity of 4.4 and loss tangent 0.018 is chosen +as substrate to facilitate printed circuit board integration. The square patch has a width W. The radiating patch is connected to a feed line with width of W_f and length of L_f. The width of the microstrip feed-line is fixed at 2 mm, as shown in Fig. 1. The proposed antenna is connected to a 50-Ω SMA connector for signal transmission.

This work started by choosing the dimensions of the designed antenna. Hence, the essential parameters for the design are: f_0=4.5 GHz (first resonance frequency), ε_r=4.4 and h_{sub}=0.8 mm. The dimensions of the patch along its length have now been extended on each end by a distance ΔL, which is given as:

$$\Delta L = 0.412\, h_{sub} \frac{(\varepsilon_{eff}+0.3)(\frac{W_{sub}}{h_{sub}}+0.264)}{(\varepsilon_{eff}-0.258)(\frac{W_{sub}}{h_{sub}}+0.8)}, \quad (1)$$

where h_{sub} is the height of dielectric, W_{sub} is the width of the microstrip monopole antenna and ε_{reff} is the effective dielectric constant. Then, the effective length (L_{eff}) of the patch can be calculated as follows:

$$L_{eff} = L + 2\Delta L \,. \quad (2)$$

For a given resonant frequency f_0, the effective length is given as:

$$L_{eff} = \frac{C}{2 f \sqrt{\varepsilon_{reff}}} \,. \quad (3)$$

For a microstrip antenna, the resonance frequency for any TM_{mn} mode is given by as:

$$\varepsilon_{eff} = \frac{(\varepsilon_r+1)}{2} + \frac{(\varepsilon_r-1)}{2}\left[1+12\frac{h_{sub}}{W_{sub}}\right]^{-\frac{1}{2}}. \quad (4)$$

The width W_{sub} of microstrip antenna is given:

$$W_{sub} = \frac{C}{2 f_0 \sqrt{\frac{(\varepsilon_r+1)}{2}}} \,. \quad (5)$$

The last and final step in the design is to choose the length of the resonator and the band-stop filter elements. In this design, the optimized length $L_{resonance}$ is set to resonate at $0.25\lambda_{resonance}$, where $L_{resonance1}=W_{S1}+L_S+0.5L_{S1}$ and $L_{resonance2}=0.5(L_{T1}+d)+0.5W_T-W_{T1}$. $\lambda_{resonance1}$ and $\lambda_{resonance2}$ corresponds to first extra resonance frequency (11

GHz) and second extra frequency (12 GHz), respectively.

In addition, to create a desired dual frequency band-stop characteristic, a pair of protruded E-shaped strips are used inside square-ring radiating patch. At the notched frequencies, the current flows are more dominant around the T-shaped and C-shaped structures, and they are oppositely directed between the embedded structures and the radiating stub. As a result, the desired high attenuation near the notched frequency can be produced. Also, the optimized length L_{notch} is set to band-stop resonate at $0.5\lambda_{notch}$, where $L_{notch1}=W_{e1}+L_{e3}+0.5(L_e+L_{e2})$, and $L_{notch2}=W_e+L_{e1}+0.5L_e$. λ_{notch1} and λ_{notch2} corresponds to first band-notched frequency (3.9 GHz) and second band-notched frequency (5.5 GHz), respectively. The final values of proposed design parameters are specified in Table 1.

Table 1: Final dimensions of the antenna

Parameter	W_{sub}	L_{sub}	h_{sub}	W_f	L_f	W
(mm)	12	18	1.6	2	7	10
Parameter	W_S	L_S	W_{S1}	L_{S1}	W_T	L_T
(mm)	6	2	2	0.5	8	3
Parameter	W_{T1}	L_{T1}	W_e	L_e	W_{e1}	L_{e1}
(mm)	1	0.5	4	6	3.5	1
Parameter	W_{e2}	L_{e2}	W_X	L_{e3}	d	L_{gnd}
(mm)	3	1	9	1.5	1	3.5

III. RESULTS AND DISCUSSIONS

In this section, the proposed microstrip monopole antenna with various design parameters was constructed. The parameters of the proposed antenna are studied by changing one parameter at a time and fixing the others. The analysis and performance of the proposed antenna is explored by using Ansoft simulation software High-Frequency Structure Simulator (HFSS) [15], for better impedance matching.

A. UWB antenna with multi-resonance characteristic

The configuration of various structures used for simulation studies were shown in Fig. 2. Return loss characteristics for the ordinary monopole antenna [Fig. 2 (a)], antenna with an inverted T-shaped slit in the ground plane [Fig. 2 (b)], and the antenna with inverted T-shaped slit and T-shaped conductor-backed plane [Fig. 2 (c)] are compared in Fig. 3.

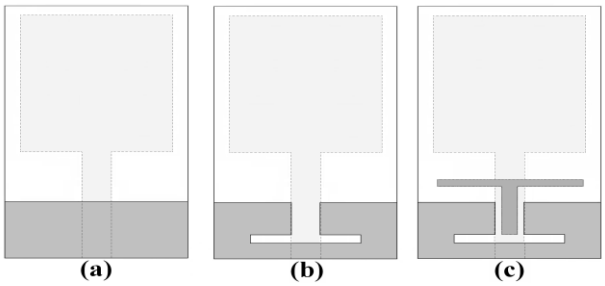

Fig. 2. (a) Ordinary monopole antenna, (b) antenna with an inverted T-shaped slit, and (c) antenna with inverted T-shaped slit and T-shaped parasitic structure.

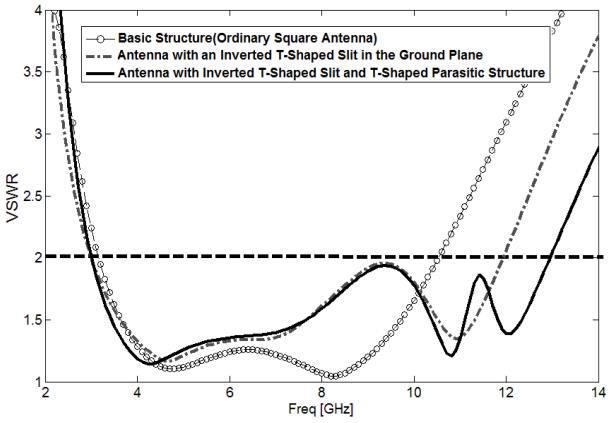

Fig. 3. Simulated return loss characteristics for the various antenna structures shown in Fig. 2.

As seen, the upper frequency bandwidth is significantly affected by using T-shaped structures in the ground plane. By using these modified elements, additional third (11 GHz) and fourth (12 GHz) resonances are excited, respectively. By using these modified structures, the usable upper frequency of the antenna is extended from 10.4 GHz to 12.8 GHz, which provides a wide usable fractional bandwidth of more than 125%.

Moreover, the input impedance of the various structures of the multi-resonance antenna on a Smith-Chart is shown in Fig. 4. The multi-resonance behavior is mainly due to the change of surface current path by changing the dimensions of the pair of T-shaped structures. In order to know the phenomenon behind the additional resonances performance, simulated current

distributions on the ground plane for the proposed antenna at 11 GHz and 12 GHz are presented in Fig. 5. It can be observed in Fig. 5 (a), that the current concentrated on the edges of the interior and exterior of the inverted T-shaped slit at 11 GHz. As shown in Fig. 5 (b), at the fourth resonance frequency the current flows are more dominant around of the T-shaped parasitic structure [8-9].

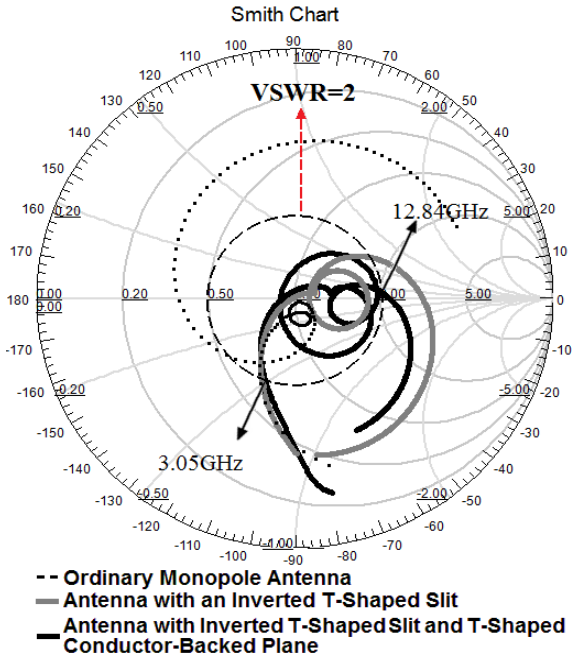

Fig. 4. Simulated input impedance results on a Smith Chart of various structures shown in Fig. 2.

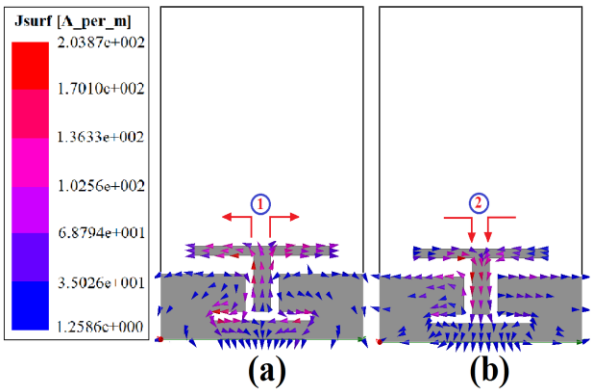

Fig. 5. Simulated surface current distributions in the ground plane for the proposed antenna: (a) at 11 GHz and (b) at 12 GHz.

In order to investigate the effects of the inverted T-shaped slit and T-shaped parasitic structures on the bandwidth of the proposed antenna and impedance matching, the VSWR characteristics for various slit and parasite sizes were analyzed in Figs. 6 and 7. As illustrated, four structures with different sizes of inverted T-shaped slit and T-shaped parasitic structure are shown in these figures. It is found that by using these structures with modified sizes of $W_S = 6 \& W_T = 8$, good additional resonances is excited and hence much wider impedance bandwidth with multi-resonance characteristics can be produced; which the usable upper frequency of the antenna is extended from 10.3 GHz to 12.84 GHz.

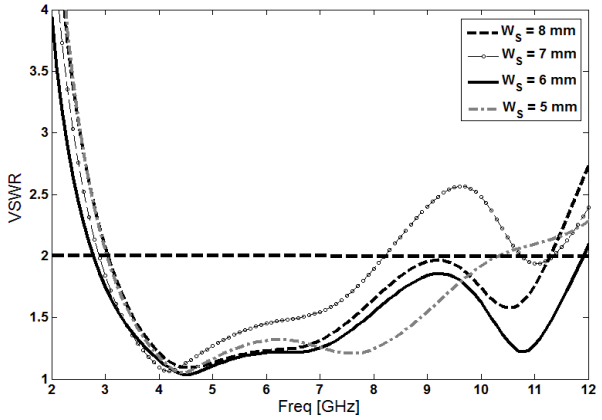

Fig. 6. Simulated VSWR characteristics for the various sizes of WS.

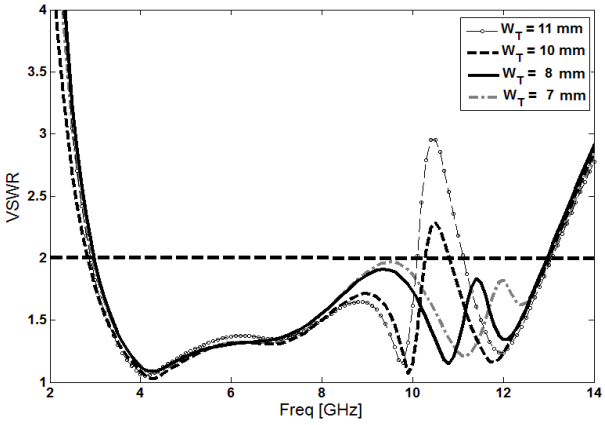

Fig. 7. Simulated VSWR characteristics for the various sizes of WT.

B. UWB antenna with dual narrow band-notched function

In order to generate the dual narrow band-notched characteristic, we used a pair of protruded E-shaped strips inside the square-ring radiating patch.

VSWR characteristics for antenna with a modified ground plane [Fig. 8 (a)], the antenna with modified ground plane and a protruded E-shaped strip inside square-ring radiating patch [Fig. 8 (b)], and the proposed antenna structure [Fig. 8 (c)] are compared in Fig. 9. As seen, to create a single band-notched characteristic, we use an E-shaped strip at square-ring radiating patch. Also, by adding another E-shaped strip, a good dual band-notched function is achieved.

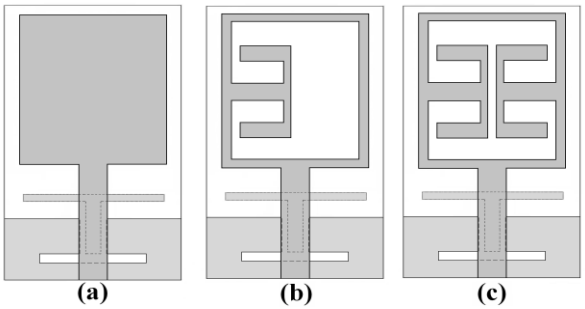

Fig. 8. (a) Antenna with modified ground plane, (b) the antenna with modified ground plane and protruded E-Shaped strip, and (c) the proposed antenna structure.

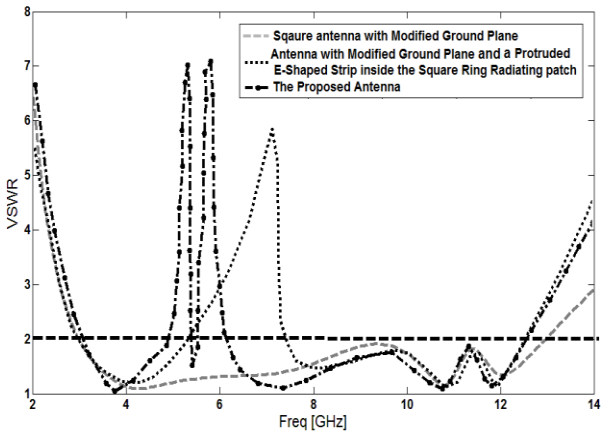

Fig. 9. Simulated VSWR characteristics for the various structures shown in Fig. 8.

In order to understand the phenomenon behind this dual band-stop performance, the simulated current distributions for the proposed antenna at the notched frequencies is presented in Fig. 10. It is found at the notched frequencies the current flows are more dominant around of the protruded E-shaped strips [10-12]. The proposed antenna with final design as shown in Fig. 11, was built and tested.

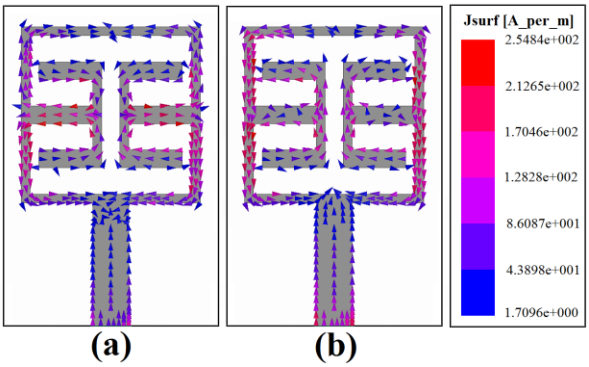

Fig. 10. Simulated surface current distributions for the proposed antenna in the radiating patch at the notched frequencies: (a) 5.2 GHz and (b) 5.8 GHz.

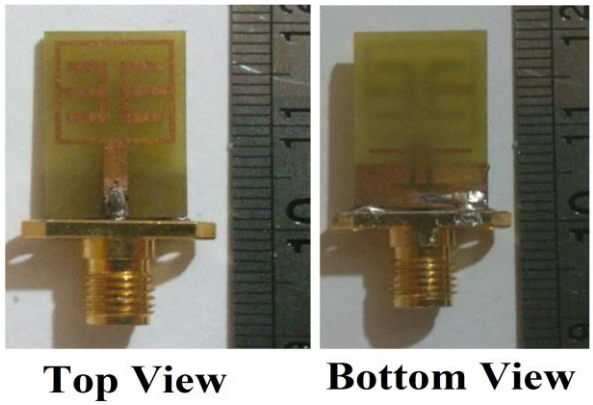

Fig. 11. Photograph of the realized antenna.

Figure 12 shows the effects of the pairs of T-shaped and E-shaped structures embedded at the proposed antenna configuration on the maximum gain in comparison to the ordinary square antenna without them. As seen, the ordinary square antenna has a gain that is low at 3 GHz and increases with frequency. It can be observed that

by using the pair of protruded E-shaped strips inside the square-ring radiating patch, the sharp decreases of maximum gain and the notched frequency bands (5.2 and 5.8 GHz) can be created. For other frequencies outside the notched frequencies, the antenna gain with the filters is similar to those without them [13].

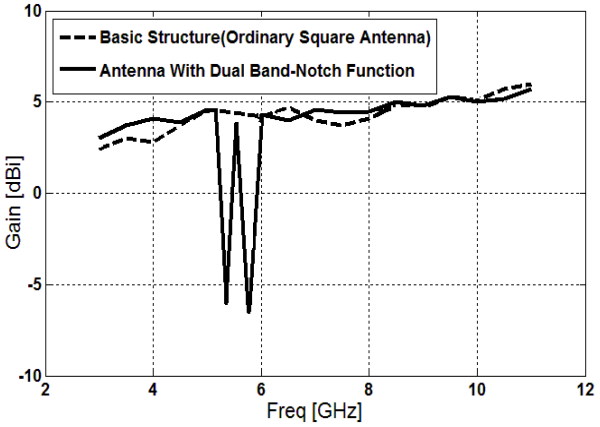

Fig. 12. Measured maximum gain of the proposed antenna in compared with the ordinary structure.

Figure 13 illustrates the FDTD computed and measured radiation patterns, including the co-polarization and cross-polarization in the H-plane (x-z plane) and E-plane (y-z plane). The main purpose of the radiating patterns is to demonstrate that the antenna actually radiates over a wide frequency band. It can be seen that the radiation patterns in *x-z* plane are nearly omni-directional for the three frequencies. The radiation patterns on the y-z plane are like a small electric dipole leading to bidirectional patterns in a very wide frequency band [13-14]. The comparison between measured and numerically computed radiation patterns are well within the acceptable limits.

Table 2 summarizes the proposed antenna and the previous designs [10-14]. As seen, the proposed antenna has a compact size with very wide bandwidth in compared to the pervious works. In addition, the proposed antenna has good omni-directional radiation patterns with low cross-polarization level, even at higher and upper frequencies. Also, the antenna imposes negligible effects on the transmitted pulses and has acceptable gain levels in the operation bands [16].

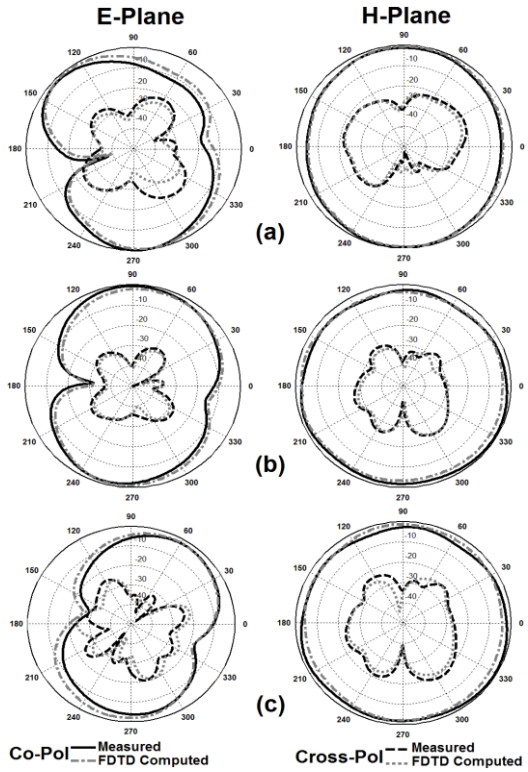

Fig. 13. The FDTD computed measured and radiation patterns of the proposed antenna at: (a) 4.2 GHz, (b) 8 GHz, and (c) 11.5 GHz.

Table 2: Comparison of previous designs with the proposed antenna

Ref.	FBW (%)	Dimension
[10]	1.8-10.5 GHz (140%)	30 mm×35 mm
[11]	2.4-10.1 GHz (120%)	28 mm×33 mm
[12]	2.8-12.0 GHz (124%)	24 mm×24 mm
[13]	3.1-10.6 GHz (109%)	16 mm×25 mm
[14]	3.0-12.0 GHz (121%)	21 mm×36 mm
This Work	*3.0-12.8 GHz (125%)*	*12 mm×18 mm*

IV. NUMERICAL RESULTS AND TIME-DOMAIN ANALYSIS

A. Numerical results

In this section, the results using FDTD method are derived for the proposed antenna and are compared with the simulated (HFSS) ones. The space steps used in Cartesian coordination are $\Delta x = 0.25mm$, $\Delta y = 0.25mm$, $\Delta z = 0.25mm$, and

the total mesh dimensions are $58\times110\times25$ in x, y and z directions, respectively. The antenna patch (Fig. 1) is thus $40\Delta x\times40\Delta y$. The length of the microstrip line from the source plane to the edge of the antenna is $150\Delta y$, and the reference plane for port 1 is $28\Delta y$ from the edge of the patch. The microstrip line width is modeled as $8\Delta x$. The time step used, according to Courant's condition is $\Delta t = 0.66ps$.

The launched wave has approximately unit amplitude and is Gaussian in time given by:

$$E_Z(t) = e^{-(\tau-\tau_0)^2/T^2}. \quad (6)$$

The wave's half-width is $T = 4\Delta t$ and the time delay t_0 is set to be $6T$, so the Gaussian will start at approximately 0; also, similar in [17], the magnetic wall source is used to minimize the source distortion. The spatial distribution of $E_Z(x, y, t)$ just beneath the microstrip at 450, 1000, 1200 and 1800 time steps is shown in Fig. 14, where the Gaussian pulse and subsequent propagation on the antenna are observed. Also, the incident, total and reflected voltages at the reference plane are illustrated in Fig. 15 for all time steps.

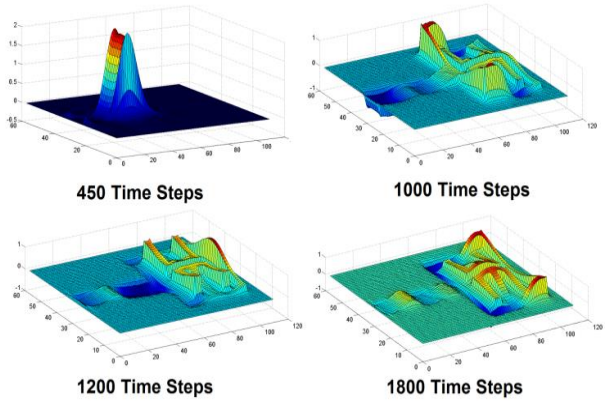

Fig. 14. The spatial distribution of EZ (x,y,t) just beneath the microstrip at 450, 1000, 1200 and 1800 time steps.

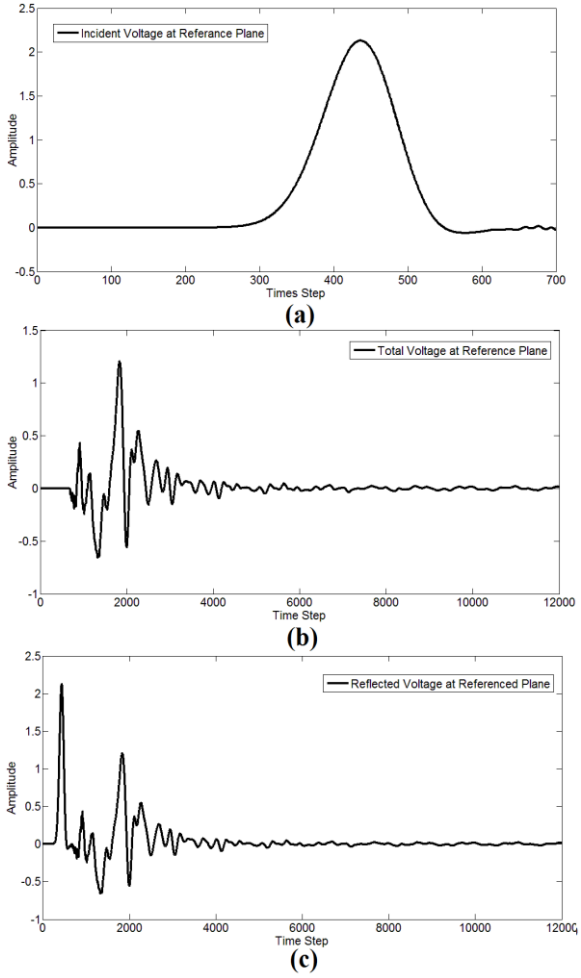

Fig. 15. (a) Incident voltage, (b) total voltage, and (c) reflected voltage at the reference plane: 50 Δy from the edge of the patch.

Measured and simulated VSWR characteristic of the proposed antenna which was calculated using FDTD and HFSS, were shown in Fig. 16. The fabricated antenna has the frequency band of 3.01 to over 12.8 GHz. Also, the frequency bands of 5.15-5.35 and 5.725-5.825 GHz are notched with maximum VSWRs more than 6.5, which is sufficient and deep enough to avoid the possible interference between UWB and WLAN systems.

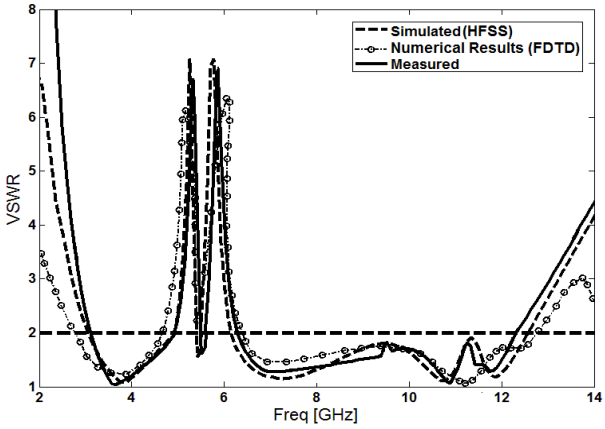

Fig. 16. Measured, simulated and FDTD computed VSWR characteristics for the antenna.

B. Time-domain analysis

In telecommunications systems, the correlation between Transmitted (TX) and Received (RX) signals is evaluated using the fidelity factor (7):

$$F = Max_{\tau} \left| \frac{\int_{-\infty}^{+\infty} s(t) r(t-\tau)}{\sqrt{\int_{-\infty}^{+\infty} s(t)^2 dt . \int_{-\infty}^{+\infty} r(t)^2 dt}} \right|, \qquad (7)$$

where $s(t)$ and $r(t)$ are the TX and RX signals, respectively.

Higher values of *F* prove a good correlation between the RX and TX signals. For impulse radio in UWB communications, it is necessary to have a high degree of correlation between the TX and RX signals to avoid losing the modulated information. However, for most other telecommunication systems, the fidelity parameter is not that relevant. In order to evaluate the pulse transmission characteristics of the proposed antenna, two configurations (side-by-side and face-to-face orientations) were chosen. The transmitting and receiving antennas were placed in a $d = 250mm$ distance from each other. As shown in Fig. 17, although the received pulses in each of the two orientations are broadened, a relatively good similarity exists between the RX and TX pulses; especially in the face-to-face orientation. Using (2), the fidelity factor for face-to-face and side-by-side configurations was obtained equal to 0.81 and 0.79, respectively. The pulse transmission results are obtained using CST [19].

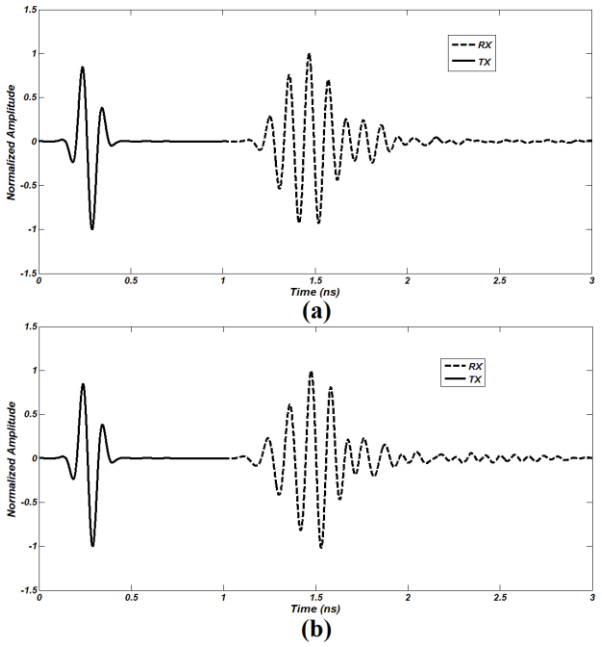

Fig. 17. Pulse transmission results: (a) side-by-side view and (b) face-to-face view.

V. CONCLUSION

A novel design of multi-resonance monopole antenna with dual band-notched function has been presented. The proposed antenna can operate from 3 to 12.8 GHz with two rejection bands around 4.9-5.3 GHz and 5.5-6.2 GHz, covering 5.2/5.8 GHz WLAN systems. Simulated and experimental results show that the proposed antenna could be a good candidate for UWB applications.

REFERENCES

[1] "FCC news release," *FCC NEWS (FCC 02-48)*, February 14, 2002.

[2] H. Schantz, "The art and science of ultra-wideband antennas," *Artech House*, 2005.

[3] M. R. Ghaderi and F. Mohajeri, "A compact hexagonal wide slot antenna with microstrip-fed for UWB application," *IEEE Antennas and Wireless Propag. Lett*., vol. 10, pp. 682-685, 2011.

[4] N. Ojaroudi, "Design of ultra-wideband monopole antenna with enhanced bandwidth," *21st Telecommunications Forum, TELFOR 2013*, Belgrade, Serbia, pp. 1043-1046, November 27-28, 2013.

[5] A. Dastranj and H. Abiri, "Bandwidth enhancement of printed e-shaped slot antennas fed by CPW and microstrip line," *IEEE Trans. Antenna Propag.*, vol. 58, pp. 1402-1407, 2010.

[6] N. Ojaroudi, "A new design of koch fractal slot antenna for ultra-wideband applications," *21st Telecommunications Forum, TELFOR 2013*, Belgrade, Serbia, pp. 1051-1054, November 27-28, 2013.

[7] A. Dastranj and H. Abiri, "Bandwidth enhancement of printed e-shaped slot antennas fed by CPW and microstrip line," *IEEE Trans. Antenna Propag.*, vol. 58, pp. 1402-1407, 2010.

[8] N. Ojaroudi, "Application of protruded strip resonators to design an UWB slot antenna with WLAN band-notched characteristic," *Progress in Electromagnetics Research C*, vol. 47, pp. 111-117, 2014.

[9] N. Ojaroudi, "Small microstrip-fed slot antenna with frequency band-stop function," *21st Telecommunications Forum, TELFOR 2013*, Belgrade, Serbia, pp. 1047-1050, November 27-28, 2013.

[10] Y. Zhang, W. Hong, C. Yu, Z. Q. Kuai, Y. D. Don, and J. Y. Zhou, "Planar ultra-wideband antennas with multiple notched bands based on etched slots on the patch and/or split ring resonators on the feed line," *IEEE Transactions on Antennas and Propagation*, vol. 56, pp. 3063-3068, 2008.

[11] J. C. Ding, Z. L. Lin, Z. N. Ying, and S. L. He, "A compact ultra-wideband slot antenna with multiple notch frequency bands," *Microwave and Optical Technology Letter*, vol. 49, pp. 3056-3060, 2007.

[12] X. L. Ma, W. Shao, and G. Q. He, "A novel dual narrow band-notched CPW-fed UWB slot antenna with parasitic strips," *Applied Computational Electromagnetics Society (ACES) Journal*, vol. 27, pp. 581-586, 2012.

[13] L. H. Ye and Q. X. Chu, "3.5/5.5 GHz dual band notch ultra-wideband slot antenna with compact size," *Electronics Letters*, vol. 46, pp. 325-327, 2010.

[14] K. S. Ryu and A. A. Kishk, "UWB antenna with single or dual band notches for lower WLAN band and upper WLAN band," *IEEE Trans. Antennas and Propag.*, vol. 57, pp. 3942-3950, December 2009.

[15] *Ansoft Corporation*, "Ansoft high frequency structure simulation (HFSS)," ver. 13, Pittsburgh, PA, 2010.

[16] A. Sheta, A. Mohra, and S. F. Mahmoud, "Multi-band operation of a compact h-shaped microstrip antenna," *Microwave and Optical Tech. Lett.*, vol. 35, pp. 363-367, 2002.

[17] *CST Microwave Studio*, ver. 2008, "Computer simulation technology," Framingham, MA, 2008.

Triple-Band Microstripline-Fed Printed Wide-Slot Antenna for WiMAX/WLAN Operations

Mustafa H. B. Ucar [1] and Yunus E. Erdemli [2]

[1] Information Systems Engineering Department, Faculty of Technology
Kocaeli University, Umuttepe, 41380 Kocaeli, Turkey
mhbucar@kocaeli.edu.tr

[2] Biomedical Engineering Department, Faculty of Technology
Kocaeli University, Umuttepe, 41380 Kocaeli, Turkey
yunusee@koceli.edu.tr

Abstract ─ A novel triple-band microstrip antenna design is introduced for WiMAX/WLAN applications. The proposed antenna has a moderate size of 38×39×0.79 mm^3, yet offers quite well gain performance (5.6-8 dBi) over the operational bands. The antenna consists of a microstrip feed-line coupled to a pair of concentric rectangular loops, as well as a split-ring element inserted within a slotted ground plane, which may also be considered as a wide-slot antenna element. In the paper, the numerical antenna design along with the corresponding measurement results is presented. An equivalent circuit modeling of the proposed design along with empirical formulae relating antenna parameters with notch frequencies is also introduced to serve as a useful design guideline.

Index Terms ─ Empirical formulae, equivalent circuit modeling, loop element, microstripline feed, multiband operation, printed wide-slot antenna, split-ring element, WiMAX, WLAN.

I. INTRODUCTION

Today's rapidly evolving modern wireless communication systems are experiencing unprecedented changes. This wave of changes leads to drive increasing importance and demand of multiband compact antennas in the wireless systems; namely, Worldwide Inter-operability for Microwave Access (WiMAX) and Wireless Local Area Network (WLAN). These services offer multiband fast-access with a high mobility at either local/wide scale, and require compact printed antenna elements. In general, conventional printed monopoles, dipoles, or slots are shown to exhibit inherent narrow bandwidth characteristics. Hence, it is necessary to tailor either feed structure or antenna element, or both to achieve desired wideband and/or multiband operation. Particularly, multiband operation is preferred to avoid possible interferences from the other communication systems which share the same frequency bands.

Recent studies have led to a variety of promising multi-band [1]-[11] printed antennas to meet WLAN/WiMAX requirements in general. In particular, the designs in [5]-[9] offer triple-band WiMAX/WLAN operations, which is also the scope of this paper. Considering those triple-band designs, an expected tradeoff between antenna size and gain performance is observed as can be seen from Table 1. Particularly, the antenna design of ref. [8] allows for an almost 3 dB gain enhancement as compared to that of ref. [5], while the latter design is almost half in size of the former design.

Table 1: Antenna size and gain comparison

Ref. No	Size (mm^3)	Gain (dBi)
[5]	20×27×1	1.8-2.78
[6]	36×30×1.6	3.27-5.0
[7]	40×40×0.8	1.77-4.13
[8]	50×50×1	4-6

In this study, we introduce a novel triple-band microstrip antenna design for WiMAX/WLAN applications. The multiband antenna has a

Submitted On: November 8, 2013
Accepted On: September 6, 2014

moderate size of 38×39×0.79 mm^3, or equivalently, the electrical size is ~0.3 λ_0×0.3 λ_0 and ~0.75 λ_0×0.75 λ_0 at the operational frequencies of 2.4 GHz and 5.95 GHz, respectively. More importantly, the proposed antenna provides much better gain performance (5.6-8 dBi) over the operational bands, while being comparable in size to its counterparts reported in [5]-[9]. In the paper, the numerical antenna design along with the corresponding measurement results is presented. We note that the full-wave analysis of the proposed design has been carried out using CST Microwave Studio.

In this study, we also introduce a simplistic equivalent circuit model for the proposed antenna, along with empirical formulae relating some design parameters and the notch frequencies to assist engineering design. In particular, equivalent circuit modeling offers a systematic way of design approach, and the related studies are available in the literature for simple antenna structures [12], [13]. However, it may be difficult to consider such analyses for rather complex configurations; e.g., our case. We therefore, offer a preliminary equivalent circuit model based on integration of previously reported simple models [14], [15]. In addition, we have derived empirical formulae relating some design parameters and the notch frequencies for the proposed triple-band antenna, which is expected to serve as an additional design perspective. A similar synthesis was previously reported for an ultra-wideband antenna [16].

The proposed triple-band antenna design is moderate-size, low-loss, low-cost, and provides flatter and better gain profile over the bands of interest compared to the aforementioned counterparts. Besides the antenna's satisfactory performance, we believe that the introduced empirical formulae along with the proposed equivalent circuit model are additional contributions of this research.

II. ANTENNA DESIGN

The triple-band antenna configuration is shown in Fig. 1, along with its physical parameters. As seen in Fig. 1, the slotted ground plane (W×L) is etched on a low-loss (tanδ=0.0009) thin substrate with a thickness of h=0.79 mm and ε_r=2.2. The proposed antenna is comprised of a stepped microstrip feed-line coupled to a pair of concentric rectangular loops as well as a split-ring element inserted within a slotted ground plane, which may also be considered as a wide-slot antenna element as depicted in Fig. 1. The rectangular wide-slot element (W_s×L_s) is excited by a stepped microstripline placed on other side of the substrate. The feedline is designed to have two sections with 50 Ω (W_f×L_f) and ~100 Ω (W_h×L_h) characteristic impedances, so as to serve for broadband matching to 50 Ω system. Also, two strip loadings (W_c×L_c) are located on each side of the feedline for the purpose of better impedance matching, particularly in the third operational band.

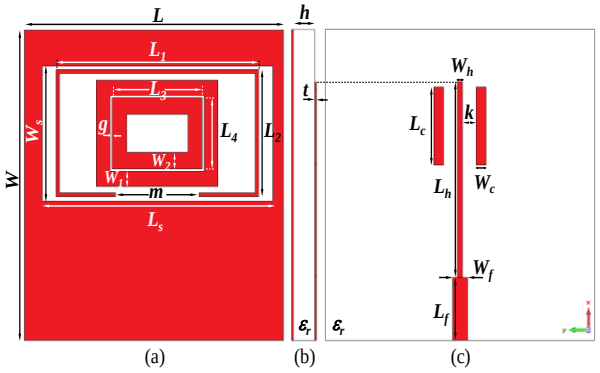

Fig. 1. The proposed antenna configuration: (a) front, (b) side, (c) back views; h=0.79, W=39, L=38, L_s=33, W_s=18.5, t=0.05, L_1=29, L_2=16, L_3=13, L_4=9, W_1=2, W_2=2.1, W_f=2.2, W_h=0.8, W_c=1.4, L_c=9.7, L_h=24.4, L_f=8, g=0.2, m=12, k=1.9 (all in mm), ε_r=2.2.

Multiband antenna operation can be achieved due to inherent antenna structure as reported in [5], [6], and [8]. However, to suppress dispensable bands, additional parasitic elements or loadings (e.g.: strips, slots, rings, etc.) may be utilized within a wide-band antenna design to realize multiband WiMAX/WLAN operation [7]. Here, we employ a similar design approach to form notch bands by inserting parasitic elements into the wide-band antenna design. Hence, three design steps depicted in Fig. 2 have been employed to reach the final triple-band antenna configuration.

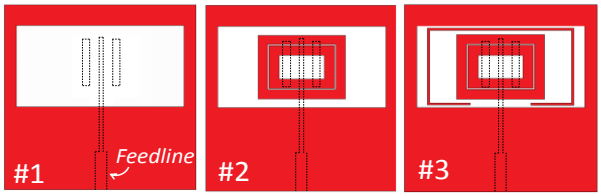

Fig. 2. The design steps for the proposed antenna configuration.

The simulated VSWR characteristics for the configurations #1, #2 and #3 are displayed in Fig. 3. At the beginning, the design #1 is obtained by means of a wide-slot antenna element coupled to a microstripline feed structure, resulting in a wideband VSWR<2 performance over 2.1-6.8 GHz band, as can be seen from Fig. 3. At the second stage, two concentric rectangular loops within the slot element are included to achieve the design #2, while introducing two notch-bands around 4.5 GHz and 6.3 GHz, owing to the outer and inner loops, respectively [4]; thus, resulting in a dual-band operation centered around 3.0 GHz and 5.5 GHz. Finally, a thin split-ring element is also placed around the double-loop element for the purpose of an additional notch-band centered at 3.1 GHz; hence, allowing for a triple-band operation with center frequencies of 2.6/3.5/5.5 GHz, while suppressing unused bands to avoid possible interferences. Consequently, the ultimate design #3 results in a triple-band operation; i.e., 2-2.96 GHz, 3.2-3.8 GHz and 5.05-6.12 GHz, which covers all the designated WLAN (2.4-2.48/5.15-5.35/5.72-5.82 GHz) and WiMAX (2.5-2.69/3.4-3.69/5.25-5.85 GHz) bands.

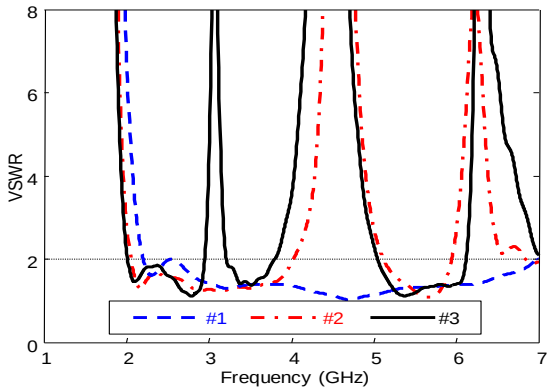

Fig. 3. The simulated VSWR characteristics of the corresponding design steps #1, #2 and #3, as depicted in Fig. 2.

III. RESULTS & DISCUSSIONS

The proposed triple-band antenna was fabricated on an Arlon DiClad 880 thin substrate (h=0.79 mm, ε_r=2.2), as shown in Fig. 4. The corresponding simulated and measured VSWR characteristics are displayed in Fig. 5.

As can be seen from Fig. 5, there is a fairly good agreement between the simulated and measured VSWR results with some expected discrepancies, due to possible material and fabrication tolerances. Of importance, is that the fabricated antenna provides the triple-band WiMAX/WLAN operation (2-2.9/3.2-3.63/5-6.2 GHz) where the notch-bands around 3.1 GHz, 4.5 GHz and 6.3 GHz are observed. We note that the VSWR measurements were carried out using Rohde & Schwarz ZVB8 Vector Network Analyzer.

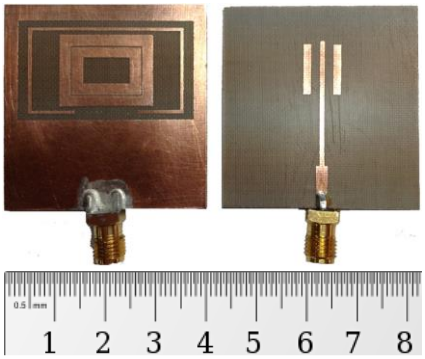

Fig. 4. The front and back views of the fabricated antenna.

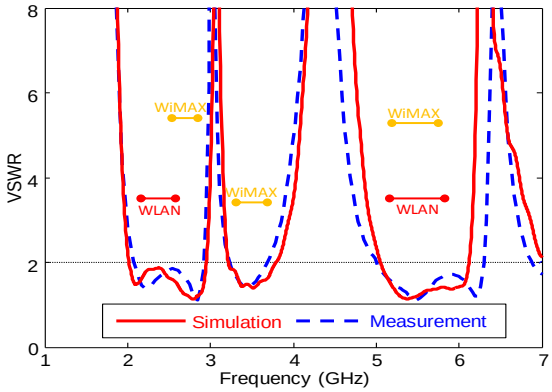

Fig. 5. The simulated and measured VSWR characteristics of the proposed antenna.

Figure 6 shows the computed surface current distributions at the centre frequencies of the notch-

bands; i.e., 3.1/4.5/6.3 GHz. As can be seen, the current distribution at 3.1 GHz is mainly concentrated over the split-ring element, while the distributions at 4.5 GHz and 6.3 GHz are predominantly highlighted around the outer and inner loops. In fact, those results confirm that the lower (3.1 GHz), the middle (4.5 GHz) and the upper (6.3 GHz) notch-bands occur by means of the presence of the split-ring, the outer loop, and the inner loop elements, respectively. As a result, by introducing those parasitic elements, possible undesired interferences at the specified notch-bands can be eliminated; thus, distortion-free communication can be achieved.

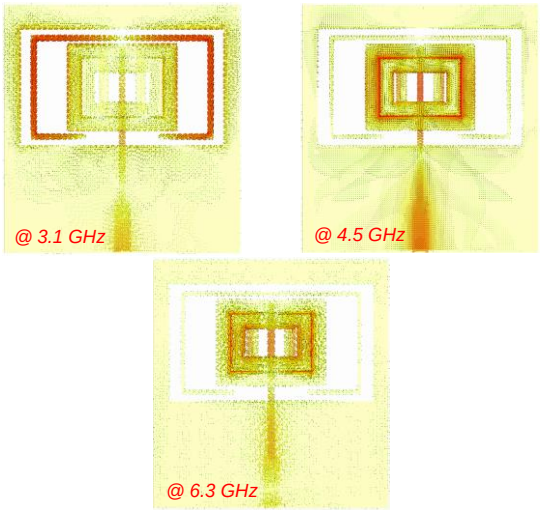

Fig. 6. The simulated surface current distributions at the centre frequencies of the notch-bands.

We also carried out radiation pattern measurements using A-INFO LB-880 DRG horn antenna (0.8-8 GHz) in a non-isolated laboratory environment. The measured patterns along with the simulations at the operational frequencies of 2.6 GHz, 3.5 GHz and 5.5 GHz are displayed in Fig. 7, where a reasonable agreement is observed. As can be seen, the antenna has almost omni-directional patterns in the H-plane and bidirectional patterns in the E-plane. Also, note that the simulated cross-polarization levels are negligible in the E-plane, while the H-plane cross-polarization levels increase with respect to increasing operating frequencies [17].

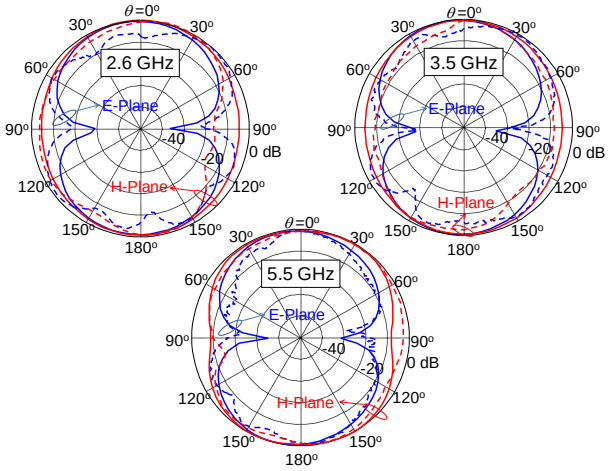

Fig. 7. The computed (solid) and measured (dashed) radiation patterns of the triple-band antenna at the center frequencies of 2.6/3.5/5.5 GHz.

Figure 8 shows the simulated realized-gain (IEEE gain × mismatch losses) characteristics for the antenna designs #1, #2 and #3 (see Fig. 2). As shown, the triple-band design (#3) has gain levels of 5.6-6.4 dBi, 6.6-6.8 dBi, and 6-8 dBi over the operational bands of 2-2.96 GHz, 3.2-3.8 GHz, and 5.05-6.12 GHz, respectively; whereas, expected gain dips occur at the designated notch-bands, owing to the parasitic elements (i.e.: split-ring and double-loop). Moreover, the measured gain has been calculated using the Friis Transmission Equation [18] for several frequency points, as shown in Fig. 8. We remark that the measured gains agree fairly well with the simulated ones over the operational bands, while some differences are observed in the notch bands with noting that a scant measurement setup was employed.

Furthermore, we extracted the measured efficiency (e_{cd}) using the measured gain (G), the measured mismatch losses ($e_m=1-|S_{11}|^2$) and the corresponding directivities (D_o) along with the formulation $G=e_{cd}\times e_m\times D_o$. For instance, the measured efficiency values at the frequencies of 2.6 GHz, 3.5 GHz, and 5.5 GHz are calculated as 97%, 95%, and 94%, which agree quite well with the simulated radiation efficiencies of 98%, 95%, and 97%. We note that possible dielectric and

conductive losses have been considered in the numerical modeling.

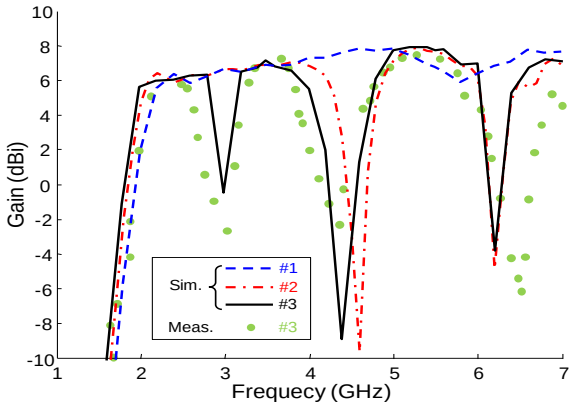

Fig. 8. The simulated and measured realized gain of the designs #1, #2, and #3, as depicted in Fig. 2.

In a systematic design process, it is very helpful for designers to relate geometrical parameters to critical design frequencies. In this context, we have developed an empirical formulae which relate the parameters of parasitic elements to the corresponding centre notch frequencies (namely, the lower frequency: f_L, the middle frequency: f_M, and the upper frequency: f_U). For this purpose, a series of simulations have been carried out by varying some parameters of the double-loop and split-ring elements as depicted in Fig. 9. It has been observed that the critical parameters mainly controlling the respective notch frequencies are L_1 (split-ring), g (gap between the loops), and L_4 (inner-loop). By employing a curve-fitting algorithm (available in MATLAB's Curve Fitting Toolbox), the following empirical equations in polynomial form have been derived based on a series of parametric studies using the CST simulator:

$$L_1 = 9.43 f_L^2 - 73.96 f_L + 167.4, \quad (1.a)$$

$$g = -929 f_M^3 - 1.72\times10^4 f_M^2 - 5.24\times10^4 f_M + 7.57\times10^4, \quad (1.b)$$

$$L_4 = -1.72 f_U - 20.35. \quad (1.c)$$

In Fig. 9, the critical parameters (L_1, g, L_4) are plotted against the particular notch frequencies (f_L, f_M, f_U), where a good agreement is observed between the proposed formulae and the CST simulations. Hence, one can specify notch frequencies, and then obtain the associated antenna parameters by means of the design curves in Fig. 9. We remark that during parametric studies, only one parameter at a time has been varied while the others kept unchanged. Also, note that there has been negligible effect observed on the antenna's frequency response, except for each notch band while varying the corresponding dimension. That is, each parameter mainly affects the corresponding notch band as can be observed from Fig. 10.

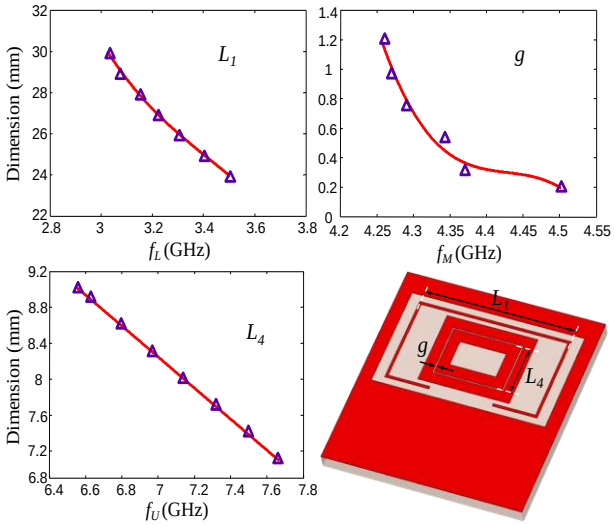

Fig. 9. The design curves for the critical parameters (L_1, g, L_4) vs. the centre notch frequencies: CST simulations (Δ) and the empirical formulae 1 (solid line).

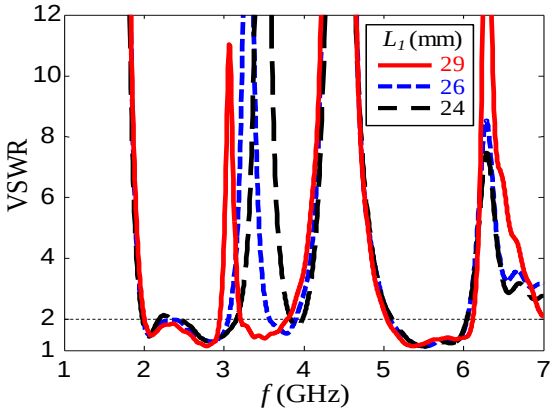

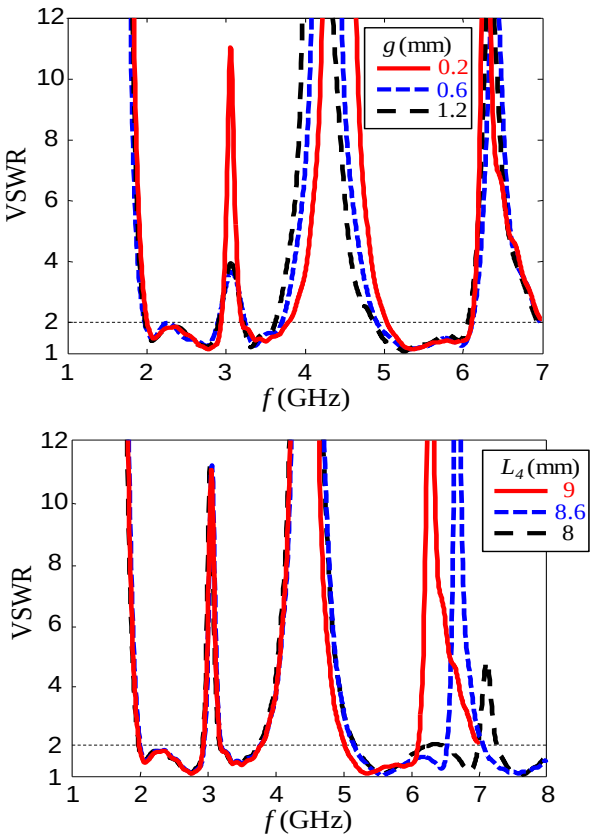

Fig. 10. The effects of the critical parameters (L_1, g, L_4) on the VSWR performance.

Furthermore, an Equivalent Circuit Model (ECM) for the triple-band antenna has been considered to serve as an additional design perspective. As depicted in Fig. 11, the proposed ECM is formed by integration of the circuit model for the loading elements (double-loop [14] and resonant split-ring) and the circuit model for the wide slot antenna alone [15]. Having constructed this simplistic model, the circuit parameters (R, L, C) have been extracted by means of a curve-fitting algorithm [19], based on the simulated VSWR characteristics of the triple-band antenna.

As can be seen from Fig. 12, the proposed ECM predicts the operational bands as well as the notch bands reasonably well. The discrepancies are probably due to the fact that this preliminary ECM does not include additional circuit elements representing coupling effects between the antenna elements. We note that those circuit element values will change if any physical parameter in the structure is altered. One can also develop empirical formulae relating the ECM values with the corresponding physical design parameters [20].

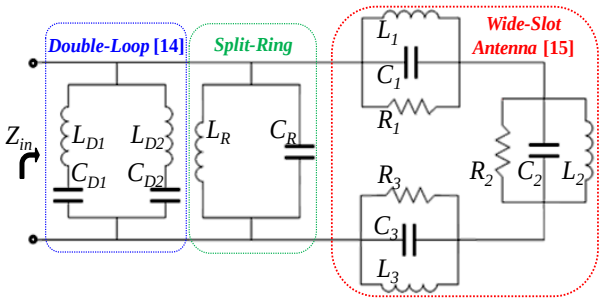

Fig. 11. The proposed equivalent circuit model for the triple-band antenna: C_1=11 pF, L_1=0.65 nH, R_1=50 Ω, C_2=4 pF, L_2=0.7 nH, R_2=25 Ω, C_3=0.7 pF, L_3=1.2 nH, R_3=45 Ω, L_R=0.07 pH, C_R=38 nF, L_{D1}=6.5 nH, C_{D1}=0.2 pF, L_{D2}=8.7 nH, C_{D2}=0.07 pF.

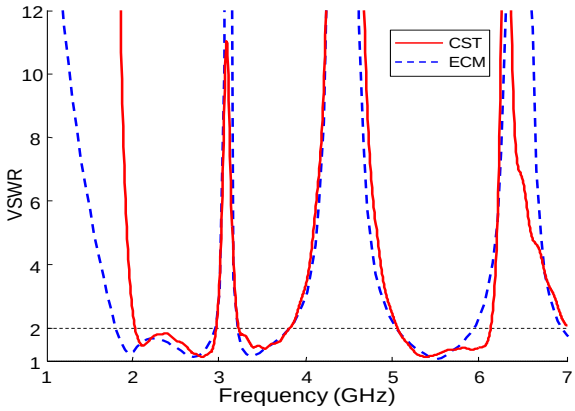

Fig. 12. The comparison of VSWR characteristics for the triple-band antenna: CST simulations vs. Equivalent Circuit Model (ECM).

IV. CONCLUSION

In the paper, a novel printed antenna has been proposed for interference-free triple-band WiMAX/WLAN operations. The printed antenna coupled to a microstrip feedline has a rectangular wide-slot element with the parasitic double-loop and split-ring elements. While the slot element alone shows wideband VSWR performance, the triple-band performance is achieved via utilizing parasitic elements within the wideband antenna design. Those parasitic loadings play a key role in generating the notch bands, which avoid possible interferences from dispensable bands and cover

only the assigned bands for WiMAX and WLAN operations. The proposed antenna is moderate-size, low-loss, low-cost, and more importantly offers flatter and better gain profile (6.5 dBi on the average) as compared to its counterparts to our best knowledge. The measurements of the fabricated antenna have been demonstrated to agree with the corresponding CST simulations quite well. Besides the antenna's satisfactory performance, the introduced empirical formulae as well as the proposed equivalent circuit model can be considered as additional contributions of this research to assist engineering design.

ACKNOWLEDGMENT

This work was supported by the Scientific Research Projects Unit of Kocaeli University (KOU-2012/08).

REFERENCES

[1] C. Y. Pan, T. S. Horng, W. S. Chen, and C. H. Huang, "Dual wideband printed monopole antenna for WLAN/WiMAX applications," *IEEE Antennas Wireless Propag. Lett.*, vol. 6, pp. 149-151, 2007.

[2] D. Zhou, R. A. Abd-Alhameed, A. G. Alhaddad, C. H. See, J. M. Noras, P. S. Excell, and S. Gao, "Multi-band weakly ground-coupled balanced antenna design for portable devices," *IET Science, Measurement & Technology*, vol. 6, no. 4, pp. 306-310, 2012.

[3] L. Hu and W. Hua, "Wide dual-band CPW-fed slot antenna," *Electron. Lett.*, vol. 47, no. 14, pp. 789-790, 2011.

[4] M. H. B. Ucar and Y. E. Erdemli, "Microstripline-coupled printed wide-slot antenna with loop loadings for dual-band WiMAX/WLAN operations," *IEEE Int. Symp. Antennas Propagat.*, Chicago, IL, pp. 1-2, July 2012.

[5] T. Wang, Y. Z. Yin, J. Yang, Y. L. Zhang, and J. J. Xie, "Compact triple-band antenna using defected ground structure for WLAN/WiMAX applications," *Prog. Electromagn. Res. Lett*., vol. 35, pp. 155-164, 2012.

[6] X. Q. Zhang, Y. C. Jiao, and W. H. Wang, "Compact wide tri-band slot antenna for WLAN/WiMAX applications," *Electron. Lett.*, vol. 48, no. 2, pp. 64-65, 2012.

[7] H. W. Liu, C. H. Ku, and C. F. Yang, "Novel CPW-fed planar monopole antenna for WiMAX/WLAN applications," *IEEE Antennas Wireless Propag. Lett.*, vol. 9, pp. 240-243, 2010.

[8] Z. X. Yuan, Y. Z. Yin, Y. Li, B. Ding, and J. J. Xie, "Multiband printed and double-sided dipole antenna for WLAN/WiMAX applications," *Microwave Opt. Technol. Letts*., vol. 54, pp. 1019-1022, 2012.

[9] P. Wang, G. J. Wen, and Y. Huang, "Compact CPW-fed planar monopole antenna with triple-band operation for WLAN/WiMAX applications," *Applied Computational Electromagnetic Society (ACES) Journal*, vol. 27, no. 8, pp. 691-696, June 2012.

[10] P. Shu and Q. Feng, "Design of a compact quad-band hybrid antenna for compass/WiMAX/WLAN applications," *Prog. Electromagn. Res.*, vol. 138, 585-598, 2013.

[11] A. Dadgarpour, A. Abbosh, and F. Jolani, "Planar multiband antenna for compact mobile transceivers," *IEEE Antennas Wireless Propag. Lett.*, vol. 10, pp. 651-654, 2011.

[12] Y. Wang, J. Li, and L. X. Ran, "An equivalent circuit modeling method for ultra-wideband antennas," *Prog. Electromagn. Res.*, vol. 82, pp. 433-445, 2008.

[13] Y. S. Wang and S. J. Chung, "A short open-end slot antenna with equivalent circuit analysis," *IEEE Trans. Antennas and Propag.*, vol. 58, no. 5, pp. 1771-1775, 2010.

[14] X. F. Luo, P. T. Teo, A. Qing, and C. K. Lee, "Design of double-square-loop frequency-selective surfaces using differential evolution strategy coupled with equivalent-circuit model," *Microwave Opt. Technol. Letts*., vol. 44, pp. 159-162, 2005.

[15] I. Pele, A. Chousseaud, and S. Toutain, "Simultaneous modeling of impedance and radiation pattern antenna for UWB pulse modulation," *IEEE Int. Symp. Antennas Propagat.*, Monterey, CA, vol. 2, pp. 1871-1874, June 2004.

[16] J. R. Kelly, P. S. Hall, and P. Gardner, "Band-notched UWB antenna incorporating a microstrip open-loop resonator," *IEEE Trans. Antennas and Propag.*, vol. 59, no. 8, pp. 3045-3048, 2011.

[17] J. Y Sze and K. L. Wong, "Bandwidth enhancement of a microstrip-line-fed printed wide-slot antenna," *IEEE Trans. Antennas and Propag.*, vol. 49, no. 7, pp. 1020-1024, 2001.

[18] C. A. Balanis, "Antenna theory analysis and design," 3rd ed., *New York: Wiley-Interscience*, pp. 1029, 2005.

[19] M. H. B. Ucar, A. Sondas, and Y. E. Erdemli, "Dual-band loop-loaded printed dipole antenna with a wideband microstrip balun structure," *Applied Computational Electromagnetic Society (ACES) Journal*, vol. 27, no. 6, pp. 458-465, June 2012.

[20] Y. E. Erdemli, K. Sertel, R. A. Gilbert, D. E. Wright, and J. L. Volakis, "Frequency selective surfaces to enhance performance of broadband reconfigurable arrays," *IEEE Trans. Antennas Propag.*, vol. 50, no. 12, pp. 1716-1724, 2002.

Mustafa H. B. Ucar received his B.S., M.S., and Ph.D. degrees from Kocaeli University, Kocaeli, Turkey, all in Electronics and Computer Education Department in 2004, 2007, and 2013, respectively. He currently serves as an Assistant Professor in the Department of Information Systems Engineering, Kocaeli University, Turkey. His research interests include numerical analysis and design of reconfigurable antennas/arrays/EM filters and frequency selective surfaces.

Yunus E. Erdemli received his B.S. degree in Electrical Engineering from Middle East Technical University, Ankara, Turkey, in 1992, and the M.S. and Ph.D. degrees from the University of Michigan, Ann Arbor, both in Electrical Engineering, in 1996 and 2002, respectively. During 1994-2002, he was a graduate Research Assistant at the University of Michigan Radiation Laboratory, Ann Arbor, where he also served as a Postdoctoral Research Associate. He currently serves as a Professor in the Department of Biomedical Engineering, Kocaeli University, Turkey. His research interests include biomedical applications, numerical analysis and design of conformal and reconfigurable antenna arrays, frequency selective surfaces/volumes and metamaterials for various communication applications.

Miniaturized Dual-Mode Dual-Band BPF Using a Single Square Patch Loaded Stepped-Impedance Square Open Loop Resonator

Jin Xu

School of Electronics and Information
Northwestern Polytechnical University, Xi'an, 710072, P.R. China
xujin227@nwpu.edu.cn

Abstract ─ This letter presents a dual-mode dual-band Bandpass Filter (BPF) using a single Square Patch Loaded Stepped-Impedance Square Open Loop Resonator (SPLSISOLR). The first four Transmission Poles (TPs) of SPLSISOLR can be tuned freely. A pair of high-impedance microstrip lines coupled with the resonator are employed to excite these four TPs to build up a dual-mode dual-band BPF, with two TPs in each passbands. The tapped point of the 50 Ω feeding lines can be freely sliding on the high impedance microstrip lines, which increases the design freedom of external quality factor of two passbands. To validate the proposed method, a dual-band filter centered at 1.79/5.42 GHz with -3 dB fractional bandwidth of 4.5%/22.5% and compact size of $0.15\lambda_g \times 0.14\lambda_g$ are designed. The fabricated filter has the merits of high band-to-band isolation, wide stopband, DC block and simple design procedure.

Index Terms ─ Bandpass Filter (BPF), dual-band, dual-mode, open loop resonator, patch resonator.

I. INTRODUCTION

With the development of modern dual-band wireless systems, dual-band Bandpass Filter (BPF) is great in demand for a single RF module to handle dual communication modes. So far, several dual-band BPFs have been studied in the past few years [1-3]. However, at least two resonators are used in the dual-band BPFs reported in [1-3], which may result in a relatively large circuit area. Dual-mode dual-band BPF using a single resonator becomes a good candidate and has been widely, owing to its compact size, high performance, simple physical configuration and design procedure [4]-[9].

Most of the reported dual-mode dual-band BPFs with a single resonator are realized by a ring resonator [4]-[6] or patch resonator [7]-[9]. By introducing the perturbations, such as *C*-sections in [4], loaded open stubs in [5], capacitive coupling in [6], embedded pair of slots in [7], cross slot and two sets of loaded stub in [8], arc- and radial-oriented slots in [9], many more modes are excited or are capable of being tuned to form the dual-mode second passband. These reported filters exhibit their own merits, but it has to admit that they also suffer from many drawbacks. The dual-band filters reported in [4], [5], [8], [9] have a less than 15 dB band-to-band isolation and suffer from a notch-like stopband on the upper stopband of the second passbands. Moreover, the dual-band filters reported in [8] and [9] lack of DC block function. In addition, two dual-mode dual-band structures presented in [6] and [7] have a lower central frequency ratio of two passbands.

In [10], a circular patch loaded uniform-impedance circular open loop resonator is proposed to exploit a dual-mode single band BPF. By using source-load coupling, transmission zeros are introduced and located on both sides of the passband, leading to a high passband skirt. In this paper, a novel Square Patch Loaded Stepped-Impedance Square Open Loop Resonator (SPLSISOLR) is proposed to exploit a dual-mode dual-band BPF. The first four Transmission Poles (TPs) are utilized and fed by a pair of high-impedance microstrip lines capacitively coupled with the resonator. The 50 Ω feeding lines are directly connected to the high-impedance microstrip lines, and the tapped point of the 50 Ω feeding lines can be freely sliding on the high-impedance microstrip lines to increase the design

Submitted On: March 12, 2013
Accepted On: September 5, 2014

freedom of external quality factor of two passbands. As an example, a dual-mode dual-band BPF centered at 1.79/5.42 GHz with -3 dB fractional bandwidth of 4.5%/22.5% is designed. The designed filter exhibits compact size, good return loss, high passband skirt and simple design procedure. Good agreement can be observed between the simulation and the measurement.

II. ANALYSIS OF SPLSISOLR

Figure 1 depicts the physical configuration of proposed SPLSISOLR, which mainly consists of three sections: i.e., a Square Patch Resonator (SPR), a stepped-impedance square Open Loop Resonator (OLR), and a pair of High-Impedance Microstrip Lines (HIML) capacitively coupled with the resonator. The space between the SPR and the stepped-impedance square OLR is equidistant and equals to S_1. Compared with the dual-mode single-band filter presented in [10], the appearance of the resonator is changed from circular shape to square shape, which is benefit for building up the second passband. The uniform-impedance OLR is changed to be a stepped-impedance one for the sake of providing many more design freedoms. The SPLSISOLR proposed here is designed on the substrate Arlon DiClad 880 (h=0.508 mm, ε_{re}=2.2, tanδ=0.0009). The width of 50 Ω feeding line W_f is chosen to be 1.55 mm. As stated in [7]-[10], a larger L_{sp} can lead to lower TPs. Additionally, L_{sp} mainly affects even-mode resonant poles, but has almost no effect on odd-mode resonant poles [10]. To analyze the property of proposed SPLSISOLR simply, L_{sp} is set to be 15 mm in the following discussion. Under the physical dimensions selected as W_1=W_2=0.8 mm, S_1=1 mm, S_2=5 mm, W_c=0.2 mm, S_c=0.5 mm, d_t=1.8 mm and L_c=7 mm, Fig. 2 plots a typical weakly coupling frequency response of proposed SPLSISOLR. As shown, the first four TPs (f_{p1}-f_{p4}) are into two groups, with two TPs in each group. If appropriate coupling coefficient and external quality factor are applied to the SPLSISOLR, a dual-mode dual-band can be designed. f_{p1} close to f_{p2} can form the first passband, while f_{p3} together with f_{p4} is able to build up the second passband. As seen in Fig. 2, the bandwidth of the first passband (BW1) will be much smaller than the bandwidth of second passband (BW2). The fifth TP f_{p5} is close to the second passband, which will result in a spurious passband if physical dimensions are not carefully selected.

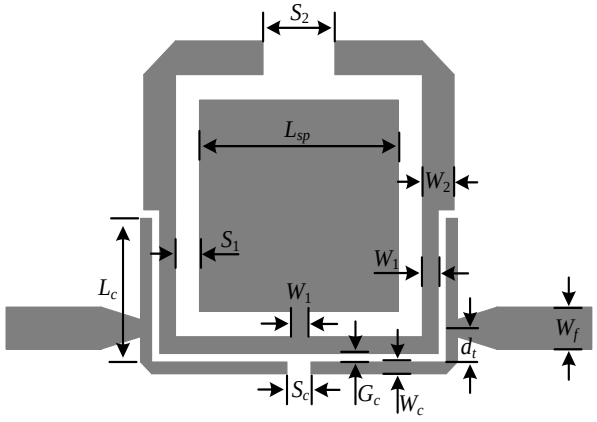

Fig. 1. Physical configuration of proposed SPLSISOLR.

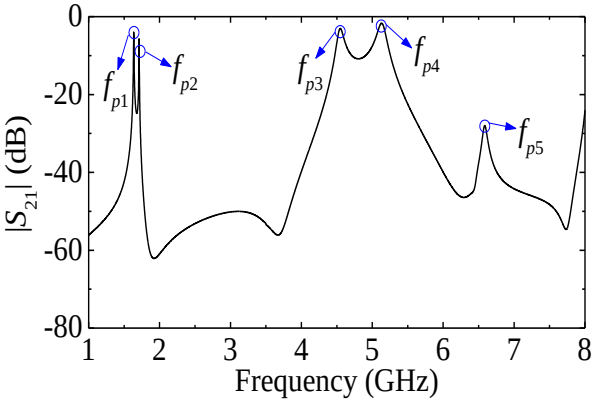

Fig. 2. Typical weakly coupling frequency response of SPLSISOLR under Gc=0.5 mm.

There are various physical dimensions which can be tuned to achieve the desired filter performance. The coupling coefficient of the designed filter can be tuned by L_c and G_c. The gap G_c is usually very narrow to provide a strong coupling. Figure 3 plots the simulated $|S_{21}|$ versus varied L_c. A longer L_c can increase the coupling degree, but too long L_c will bring spurious passband close to the second passband. So that the length of L_c should be selected neither too short to achieve enough coupling degree, nor too long to suppress the spurious frequency response. Figures 4, 5 and 6 plot the simulated $|S_{21}|$ versus varied W_1, S_2 and W_2, respectively. As W_1 increases, BW1

increases while the second passband shift towards lower frequency apparently. As S_2 increases, both the first passband and the second passband move towards higher frequency. Meanwhile, BW1 becomes narrower. W_2 has almost no effect on the performance of the second passband, but BW1 becomes wide and the first passband moves towards lower frequency as W_2 increases. It is noted that BW2 does not change dramatically as W_1, S_2 and W_2 varies. In addition, although the variation of W_1, S_2 and W_2 will affect the spurious passband, this can be then tuned by the length of L_c. Therefore, the frequency position and the bandwidth of two passband can be easily tuned by these physical dimensions.

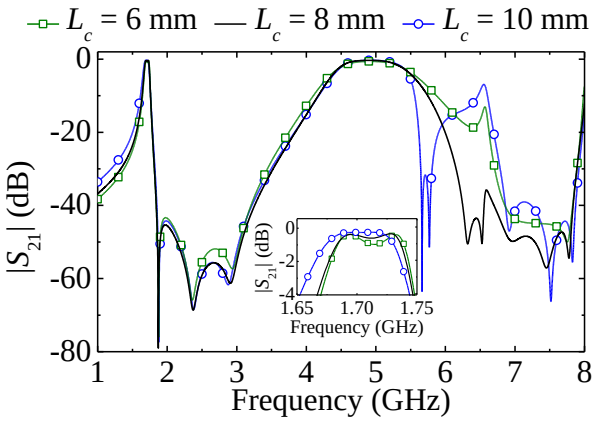

Fig. 3. Simulated |S21| versus varied Lc under Gc=0.1 mm.

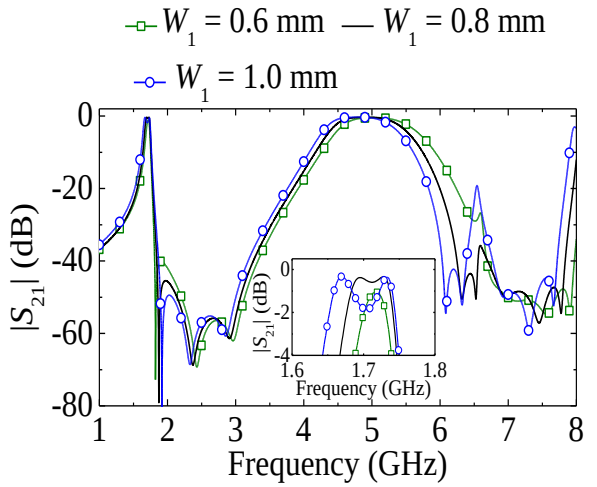

Fig. 4. Simulated |S21| versus varied W1 under Gc=0.1 mm.

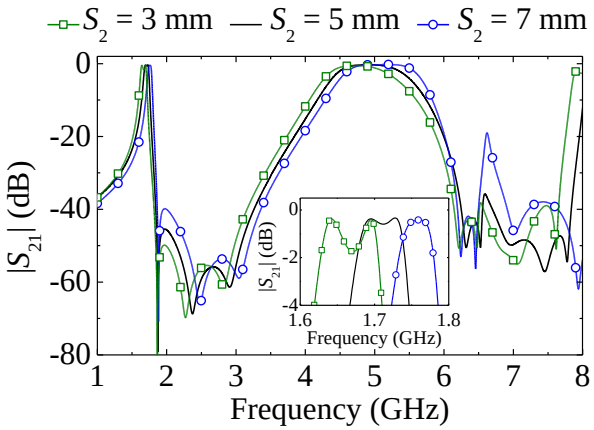

Fig. 5. Simulated |S21| versus varied S2 under Gc=0.1 mm.

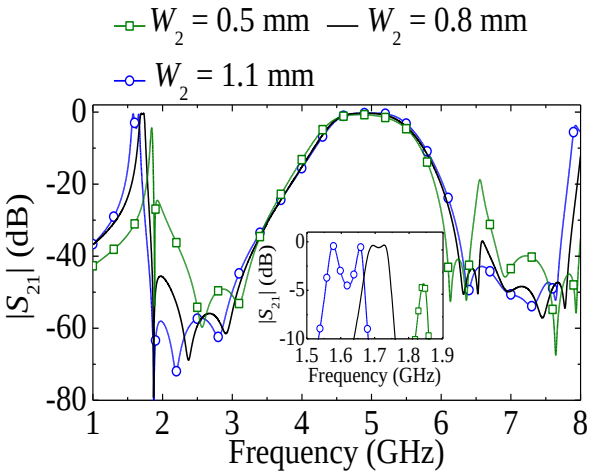

Fig. 6. Simulated |S21| versus varied S2 under Gc=0.1 mm.

III. DUAL-MODE DUAL-BAND BPF DESIGN

To verify the proposed method, a dual-mode dual-band BPF shown in Fig. 1 is designed on the substrate Arlon DiClad 880 (h=0.508 mm, ε_{re}=2.2, tanδ=0.0009). The SPLSISOLR is optimized in 3-D full wave EM simulator HFSS. After W_1 and S_2 are tuned to achieve the desired frequency position and bandwidth of two passbands, W_2 can then be tuned to separate the performance of the first passband. L_c is optimized to achieve the desired coupling coefficient and also suppress the spurious passband. The tuned physical dimensions of SPLSISOLR are L_{sp}=14.2 mm, W_1=0.62 mm, L_{11}=7.79 mm, L_{12}=7.5 mm, S_1=1.0 mm, W_2=0.73

mm, L_{21}=8.7 mm, L_{22}=4.975 mm, W_c=0.2 mm, G_c=0.09 mm, L_{c1}=8.12 mm, L_{c2}=8.56 mm and S_c=0.5 mm. Figure 7 plots the external quality factor of two passbands against d_t. As d_t increases, the external quality factor of the first passband (Q_{e1}) decreases, while the external quality factor of the second passband (Q_{e2}) keeps almost constant at about the value of 5. Thus, BW1 can be easily controlled by d_t. In our design, d_t=1.8 mm is selected to provide the appropriate external quality factor for two passbands.

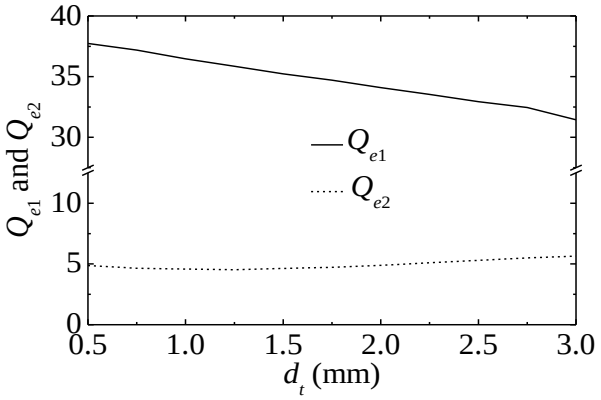

Fig. 7. Variation of Qe1 and Qe2 against varied dt.

The overall circuit size excluding 50 Ω feeding lines is 18.02 mm × 17.84 mm, corresponding to 0.15λ_g × 0.14λ_g, where λ_g represents the guided wave-length of 50 Ω microstrip line at the central frequency of the first passband. Figure 8 shows the photograph of fabricated filter. Figure 9 plots the simulated and measured *S*-parameters of the fabricated filter. Good agreement can be observed between the simulation and measurement. There are some discrepancies which are attributed to the fabrication error as well as SMA connectors. The measured central frequencies and -3 dB FBW of two passbands are 1.79/5.42 GHz and 4.5%/22.5%, respectively. The measured Insertion Loss (IL) at two central frequencies are 2.8/1.1 dB, while the return losses of two passbands are better than 20 dB. The band-to-band isolation is better than 30 dB from 1.91 GHz to 3.52 GHz. The fabricated filter also has -20 dB rejection level stopband from 6.45 GHz to 8.59 GHz.

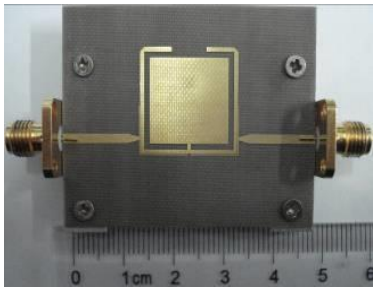

Fig. 8. Photograph of the fabricated filter.

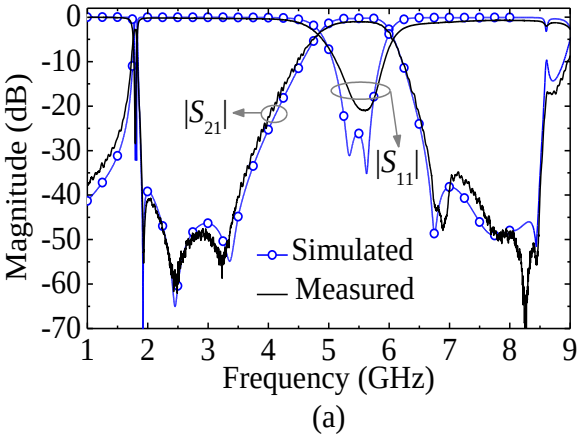

(a)

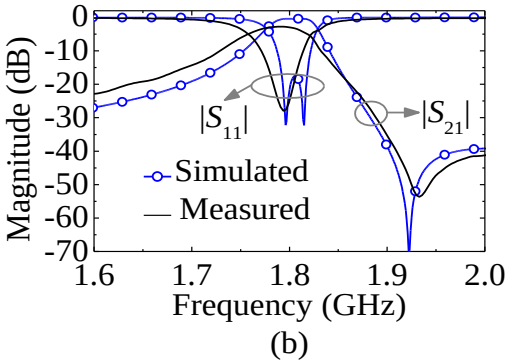

(b)

Fig. 9. Simulated and measured results of the fabricated filter: (a) wideband view, and (b) narrow-band view of the first passband.

Table 1 gives a performance comparison of this work with the reported dual-mode dual-band BPFs using a single resonator. After comparison, it can be easily found that it exhibits the merits of higher isolation and more compact sizes. Moreover, the designed filter has a larger dual-band central frequency ratio. In addition, this work

also exhibits the best out-of-band rejection performance compared with the reported works in [4]-[9], which do not show in Table 1.

Table 1: Performance comparison with reported works

		IL (dB)	Isolation (dB)	Circuit Area (λ_g^2)
[4]	1st	2.56, 1.45	>12	0.21 × 0.21
	2nd	2.39, 1.56	>12	0.14 × 0.16
[5]	1st	2, 1.4	>11	0.31 × 0.38
	2nd	2, 2	>12	0.28 × 0.33
[6]		0.65, 1	>30	0.39 × 0.39
[7]		1.1, 1.6	>20	0.31 × 0.31
[8]		0.6, 1.4	>11	0.46 × 0.42
[9]		2.5, 1.3	>18	0.43 × 0.69
This work		2.8, 1.1	>40	0.15 × 0.14

IV. CONCLUSION

A dual-mode dual-band BPF centered at 1.79/5.42 GHz with -3 dB FBW of 4.5%/22.5% and compact size of $0.147\lambda_g \times 0.145\lambda_g$ are presented in this paper. Compared with the reported dual-mode dual-band BPFs by using ring resonators or patch resonators in [4-9], the fabricated filter proposed in this paper has the merits of higher band-to-band isolation, higher passband selectivity, wider stopband, simpler physical configuration and design procedure. All these merits make it attractive in modern dual-band operation systems.

ACKNOWLEDGMENT

This work was supported by the Fundamental Research Funds for Central Universities under Grant 3102014JCQ01058, and the National Natural Science Foundation of China under Grant 61401358.

REFERENCES

[1] M. Hayati, A. Khajavi, and H. Abdi, "A miniaturized microstrip dual-dand bandpass filter using folded UIR for multimode WLANs," *Applied Computational Electromagnetics Society (ACES) Journal*, vol. 28, no. 1, pp. 35-40, January 2013.

[2] X. Li and J. Zeng, "A novel dual-band microstrip bandpass filter design and harmonic suppression," *Applied Computational Electromagnetics Society (ACES) Journal*, vol. 28, no. 4, pp. 348-352, April 2013.

[3] Y. Ma, W. Che, W. Feng, and J. Chen, "High selectivity dual-band bandpass filter with flexible passband frequencies and bandwidths," *Applied Computational Electromagnetics Society (ACES) Journal*, vol. 28, no. 5, pp. 419-426, May 2013.

[4] Y. C. Chiou, C. Y. Wu, and J. T. Kuo, "New miniaturized dual-mode dual-band ring resonator bandpass filter with microwave C-sections," *IEEE Microw. Wireless Compon. Lett.*, vol. 20, no. 2, pp. 67-69, 2009.

[5] S. Luo, L. Zhu, and S. Sun, "A dual-band ring resonator bandpass filter based on two pairs of degenerate modes," *IEEE Trans. Microw. Theory Tech.*, vol. 58, no. 12, pp. 3427-3432, 2010.

[6] S. Sun, "A dual-band bandpass filter using a single dual-mode ring resonator," *IEEE Microw. Wireless Compon. Lett.*, vol. 21, no. 6, pp. 298-300, 2011.

[7] Y. Sung, "Dual-mode dual-band filter with band notch structures," *IEEE Microw. Wireless Compon. Lett.*, vol. 20, no. 2, pp. 73-75, 2010.

[8] Y. C. Li, H. Wong, and Q. Xue "Dual-mode dual-band filter based on a stub-loaded patch resonator," *IEEE Microw. Wireless Compon. Lett.*, vol. 21, no. 10, pp. 525-527, 2011.

[9] R. Zhang, L. Zhu, and S. Luo, "Dual-mode dual-band bandpass filter using a single slotted circular patch resonator," *IEEE Microw. Wireless Compon. Lett.*, vol. 22, no. 5, pp. 233-235, 2012.

[10] X. C. Zhang, Z. Y. Yu, and J. Xu, "Design of microstrip dual-mode filters based on source-loaded coupling," *IEEE Microw. Wireless Compon. Lett.*, vol. 18, no. 10, pp. 677-679, 2008.

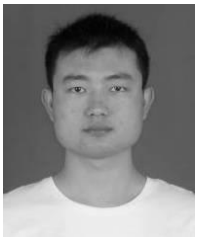

Jin Xu was born in AnHui, China, in 1987. He received his B. Eng. degree in Information Countermeasure Technology and his Ph.D. degree in Information and Communication Engineering from Nanjing University of Science and Technology (NUST), Nanjing, China, in 2009 and 2014, respectively. He is currently an Associate Professor with the School of Electronics and Information, Northwestern Polytechnical University, Xi'an, China. His research interests include UWB technology, MCM technology, microwave passive/active components, microwave and millimeter-wave MMICs developed on SiGe, phased array radar and wireless communication system.

From February 2011 to September 2011, he was an attached Ph.D. student at the Institute of Microelectronics, Singapore. From October 2011 to September 2012, he joined MicroArray Technologies

Corporation Limited, Chengdu, P.R. China, where he was an IC R&D Engineer. Since 2011, he has served as a Reviewer for some journals including IEEE Microwave Wireless Component Letters, International Journal of Electronics, PIER and JEMWA.

UWB Monopole Antenna with Dual Band-Stop Performance Using G-Shaped SRR and SIR Structures at Feed Line

Sajjad Ojaroudi [1], Yasser Ojaroudi [1], Noradin Ghadimi [2], and Nasser Ojaroudi [2]

[1] Young Researchers and Elite Club, Germi Branch
Islamic Azad University, Germi, Iran

[2] Young Researchers and Elite Club, Ardabil Branch
Islamic Azad University, Ardabil, Iran
noradin.ghadimi@gmail.com

Abstract ─ This article presents a new design of ultra-wideband monopole antenna with the characteristics of dual band rejection .The antenna consists of a circular radiating patch, a feed-line with G-shaped Step-Impedance Resonator (SIR) slot and Split-Ring Resonator (SRR) structure, and a ground plane which provides a wide usable fractional bandwidth of more than 120% with two notch bands around 5.15-5.35 GHz and 7.25-7.75 GHz, to avoid interferences from High Performance Radio Local Area Networks (HIPERLAN) and downlink frequency of X-band satellite systems. The simulated and measured results show that the antenna design exhibits an operating bandwidth (VSWR<2) from 2.86 to 12.92 GHz, excluding the rejected bands. The proposed antenna configuration is simple, easy to fabricate and can be integrated into any UWB system. The antenna has an ordinary circular-disc radiating patch, therefore displays good omni-directional radiation patterns, even at higher frequencies.

Index Terms ─ Dual band-notched function, G-shaped structure, hiperlan, satellite communications, UWB.

I. INTRODUCTION

After allocation of the frequency band from 3.1 to 10.6 GHz for the commercial use of Ultra-Wideband (UWB) systems by the Federal Communication Commission (FCC) [1], ultra-wideband systems have received phenomenal gravitation in wireless communication. Designing an antenna to operate in the UWB band is quite a challenge, because it has to satisfy the requirements such as ultra wide impedance bandwidth, omni-directional radiation pattern, constant gain, high radiation efficiency, constant group delay, low profile, easy manufacturing, etc. [2]. In UWB communication systems, one of key issues is the design of a compact antenna while providing wideband characteristic over the whole operating band. Consequently, a number of microstrip antennas with different geometries have been experimentally characterized [3-7].

There are many narrowband communication systems which severely interfere with the UWB communication system, such as the High Performance Radio Local Area Networks (HIPERLAN) operating at 5.15-5.35 GHz, or downlink of X-band satellite communication (7.25-7.75 GHz). Therefore, UWB antennas with band-notched characteristics to filter the potential interference are desirable. Nowadays, to mitigate this effect, many UWB antennas with various band-notched properties have developed [8-11]. Many techniques are also used to introduce notch band for rejecting the interference in the UWB antennas. It is done either by inserting switchable structures in the ground plane [12], applying a shunt open-circuited stub [13], using Step-Impedance Resonators (SIR) [14], inserting fractal structures [15], or using T-ring slot at the square radiating patch [16].

All of the above methods are used for rejecting a single band of frequencies. However, to effectively utilize the UWB spectrum and to

Submitted On: December 1, 2013
Accepted On: September 6, 2014

improve the performance of the UWB system, it is desirable to design the antenna with dual band rejection. It will help to minimize the interference between the narrow band systems with the UWB system. Some methods are used to obtain the dual band rejection in the literature [17-20].

In this paper, a different method is proposed to obtain the dual band rejection of frequency bands for HiperLAN and downlink frequency of X-band satellite communication systems. The HiperLAN frequency band is rejected by inserting a G-shaped SRR in the feed-line at center frequency of 5.2 GHz, and a G-shaped SIR is inserted to reject the desired downlink band of satellite systems at a center frequency of 7.5 GHz. The proposed antenna with the dual band-notched function is successfully implemented and the simulation results show reasonable agreement with the measurement results. The designed antenna has a small size. Good VSWR and radiation pattern characteristics are obtained in the frequency band of interest.

II. ANTENNA DESIGN

The structure of proposed monopole antenna fed by a microstrip line is shown in Fig. 1. The dielectric substance (FR4) with thickness of 1.6 mm with relative permittivity of 4.4 and loss tangent 0.018 is chosen as substrate to facilitate printed circuit board integration. The basic monopole antenna structure consists of a circular radiating patch, a feed line, and a ground plane. The proposed antenna is connected to a 50-Ω SMA connector for signal transmission. The radiating patch is connected to a feed line of width W_f and length L_{gnd} .The width of the microstrip feed line is fixed at 2 mm, as shown in Fig. 1. On the other side of the substrate, a conducting ground plane of width W_{sub} and L_{gnd} length is placed. Final parameter values of the presented antenna design are specified in Table 1.

Table 1: Final parameter values of the antenna

Parameter	W_{sub}	W_{sub}	W	L	W_f
(mm)	12	18	0.25	3.8	2
Parameter	L_f	W_1	L_1	W_2	L_2
(mm)	7	0.25	3.3	0.75	4.25
Parameter	W_3	L_3	W_4	L_4	W_5
(mm)	0.25	4.75	1.3	0.25	0.75
Parameter	L_5	W_6	L_6	d	R
(mm)	0.25	1.25	1.65	0.25	5

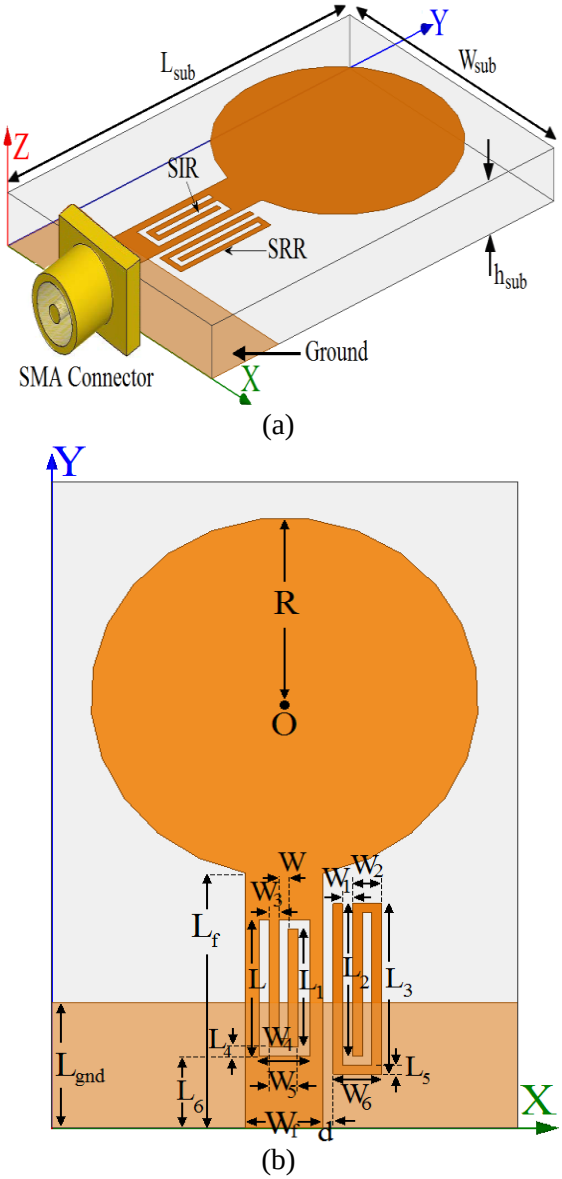

Fig. 1. Structure of the proposed antenna: (a) side view, and (b) top view.

At the first notched frequency, the current concentrated on the edges of the interior and exterior of G-shaped SRR. Additionally, the G-shaped SIR acts as a filtering element to generate another notched frequency, because it can create additional surface current path around of feed-line. At this notched frequency (7.5 GHz), the current flows are more dominant around the modified SIR, and they are oppositely directed between the inserted slits and the radiating patch [8-12]. As a result, the desired high attenuation near the notched frequencies can be produced.

III. RESULTS AND DISCUSSIONS

In this section, the microstrip monopole antenna with various design parameters was constructed, and the numerical and experimental results of the input impedance and radiation characteristics are presented and discussed. The analysis and performance of the proposed antenna is explored by using Ansoft simulation software High-Frequency Structure Simulator (HFSS) [21], for better impedance matching.

The structure of the various antennas used for simulation studies were shown in Fig. 2. VSWR characteristics for the ordinary circular monopole antenna (Fig. 2 (a)), antenna with a G-shaped SRR at feed-line (Fig. 2 (b)), and the proposed antenna structure (Fig. 2 (c)) are compared in Fig. 3.

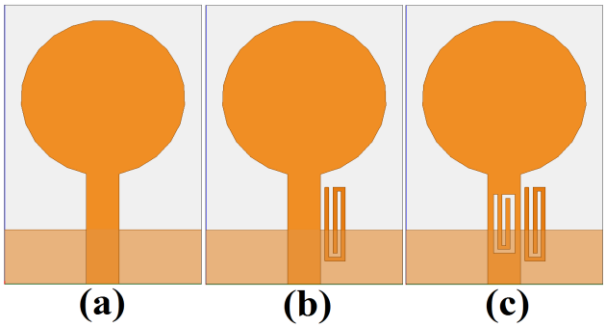

Fig. 2. (a) Ordinary square antenna, (b) antenna with a G-shaped SRR at feed line, and (c) the proposed antenna.

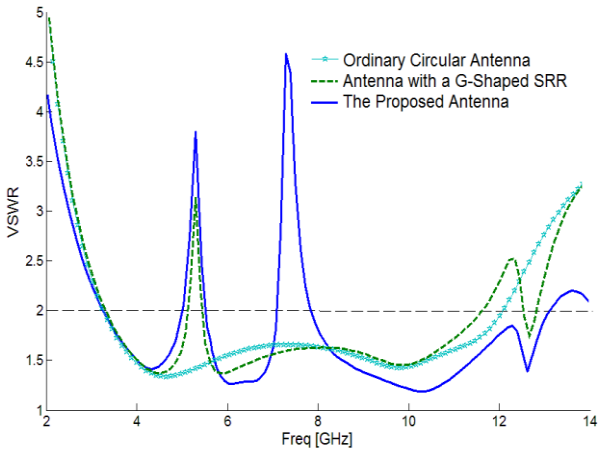

Fig. 3. Simulated VSWR for the various antenna structures shown in Fig. 2.

As shown in Fig. 3, to generate a single frequency band-notched function (5.15-5.35 GHz), we use a G-shaped SRR, and also by adding a G-shaped SIR at feed-line, the dual band-notched function can be achieved that covers all the 5.2 GHz HiperLAN and 7.5 GHz satellite down-link bands.

The simulated current distribution on the radiating patch for the proposed antenna at the notched frequencies of 5.2 and 7.5 GHz is presented in Figs. 4 (a) and 4 (b), respectively. The current direction on the reject structures is opposite to that on the nearby antenna structure, so the far fields produced by the currents on the reject structures and nearby antenna structure cancel out each other in the reject band. In Fig. 4 (b), the current mainly flows around the outer inverted G-shaped SRR, which destructs the radiation of the original antenna at this band and results in the lower stop-band [22-24].

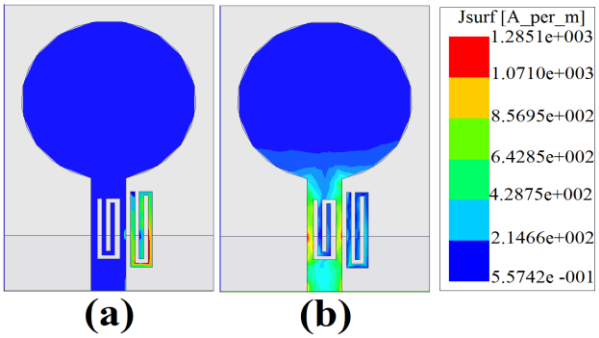

Fig. 4. Simulated surface current distributions for the proposed antenna at the notched frequencies: (a) 5.2 GHz, and (b) 7.5 GHz.

In Fig. 4 (b), the current distribution at 7.5 GHz is even on the outer and inner of G-shaped SIR, but the current direction on the inner slits is opposite to that on the outer ones. It is suggested that two band notches should be mutually interfered with and the notched property does not have any influence on the antenna radiation at 7.5 GHz. Then, a pass-band between two adjacent stop-bands can be obtained because of the mutual interference of the two notched structures [25-27].

Figure 5 shows the measured and simulated VSWR characteristics of the proposed antenna. The fabricated antenna has the frequency band of 3.02 to over 13.32 GHz, with two notch bands around 5.15-5.35 GHz and 7.25-7.75 GHz.

The maximum gain of the proposed antenna was shown in Fig. 6. A sharp decrease of

maximum gain in the notched frequency bands at 5.2 and 7.5 GHz are shown in Fig. 6. For other frequencies outside the notched frequency band, the antenna gain with the filters is similar to those without them [28-32].

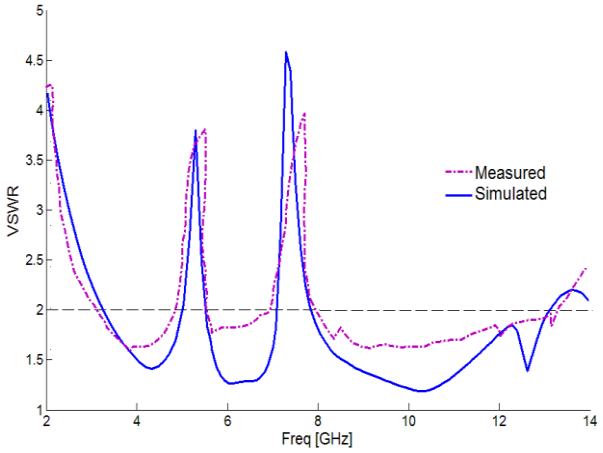

Fig. 5. VSWR comparison of the proposed antenna.

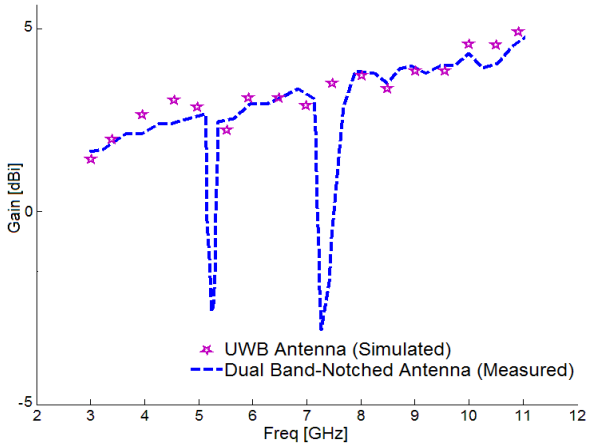

Fig. 6. Measured maximum gain of the proposed antenna.

Figure 7 depicts the measured and simulated radiation patterns including the co-polarization and cross-polarization in the H-plane (x-z plane) and E-plane (y-z plane). It can be seen that nearly omni-directional radiation pattern can be observed on x-z plane over the whole UWB frequency range, especially at the low frequencies. The radiation patterns on the y-z plane are like a small electric dipole leading to bidirectional patterns in a very wide frequency band. With the increase of frequency, the radiation patterns become worse because of the increasing effects of the cross-polarization [33-38].

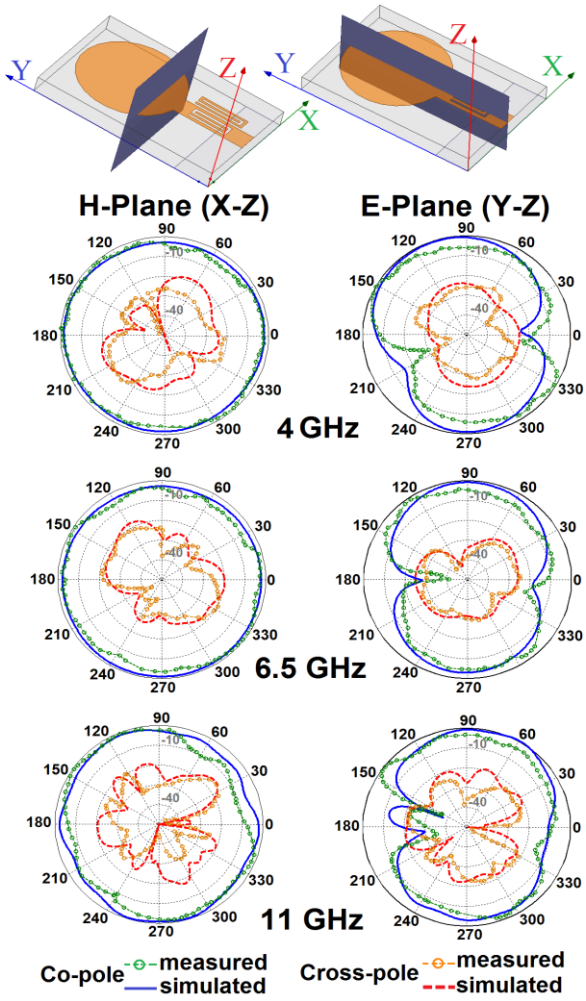

Fig. 7. Measured and simulated radiation patterns.

IV. CONCLUSION

In this paper, a new antenna structure is proposed that provides a double stop-band notch in the 5.2/7.5 GHz for various UWB applications. The fabricated antenna has the frequency band of 2.86 to over 12.92 GHz, with two rejection bands around 5.15-5.35 and 7.25-7.75 GHz. The proposed antenna has a simple configuration and small size. The designed antenna can be used in UWB systems to reduce interference between UWB and other wireless communication systems. The proposed antenna has an ordinary square radiating patch, therefore displays a good omni-directional radiation pattern even at higher

frequencies.

ACKNOWLEDGMENT

The authors are thankful to MWT Company staff for their help (www.microwave-technology.com).

REFERENCES

[1] "FCC news release," *FCC NEWS (FCC 02-48)*, February 14, 2002.

[2] D. Cheng, "Compact ultra-wideband microstrip resonating antenna," *US Patent 7872606*, January 2011.

[3] Z. N. Chen, "Impedance characteristics of planar bow-tie-like monopole antennas," *Electronics Letters*, vol. 36, pp. 1100-1101, June 2000.

[4] N. Ojaroudi, "Design of ultra-wideband monopole antenna with enhanced bandwidth," *21st Telecommunications Forum, TELFOR 2013*, Belgrade, Serbia, pp. 1043-1046, November 27-28, 2013.

[5] N. Ojaroudi, "A new design of koch fractal slot antenna for ultra-wideband applications," *21st Telecommunications Forum, TELFOR 2013*, Belgrade, Serbia, pp. 1051-1054, November 27-28, 2013.

[6] N. Ojaroudi, S. Amiri, and F. Geran, "A novel design of reconfigurable monopole antenna for UWB applications," *Applied Computational Electromagnetics Society (ACES) Journal*, vol. 28, no. 6, pp. 633-639, July 2013.

[7] N. Ojaroudi, "Compact UWB monopole antenna with enhanced bandwidth using rotated L-shaped slots and parasitic structures," *Microw. Opt. Technol. Lett.*, vol. 56, pp. 175-178, 2014.

[8] T. Dissanayake and K. P. Esselle, "Prediction of the notch frequency of slot loaded printed UWB antennas," *IEEE Trans. Antennas and Propag*., vol. 55, no. 11, pp. 3320-3325, 2007.

[9] N. Ojaroudi, "Design of small reconfigurable microstrip antenna for UWB-CR applications," *19th International Symposium on Antenna and Propagation, ISAP2014*, Kaohsiung, Taiwan, December 2-5, 2012.

[10] N. Ojaroudi, "Application of protruded strip resonators to design an UWB slot antenna with WLAN band-notched characteristic," *Progress In Electromagnetics Research C*, vol. 47, pp. 111-117, 2014.

[11] T. G. Ma and S. J. Wu, "Ultra-wideband band-notched folded strip monopole antenna," *IEEE Trans. Antennas Propag.*, vol. 55, no. 9, pp. 2473-2479, 2007.

[12] N. Ojaroudi and M. Ojaroudi, "A novel design of reconfigurable small monopole antenna with switchable band notch and multi-resonance functions for UWB applications," *Microw. Opt. Technol. Lett*., vol. 56, pp. 652-656, 2013.

[13] C. Y. Pan, K. Y. Chiu, J. H. Duan, and J. Y. Jan, "Band-notched ultra-wideband planar monopole antenna using shunt open-circuited stub," *Microwave and Optical Technology Letter*, vol. 53, no. 7, pp. 1535-1537, 2011.

[14] N. Ojaroudi, M. Ojaroudi, and S. Amiri, "Compact UWB microstrip antenna with satellite down-link frequency rejection in X-band communications by etching an E-shaped step-impedance resonator slot," *Microw. Opt. Technol. Lett*., vol. 55, pp. 922-926, 2013.

[15] Y. S. Li, X. D. Yang, C. Y. Liu, and T. Jiang, "Analysis and investigation of a cantor set fractal UWB antenna with a notch-band characteristic," *Progress In Electromagnetics Research B*, vol. 33, pp. 99-114, 2011.

[16] M. T. Partovi, N. Ojaroudi, M. Ojaroudi, and N. Ghadimi, "Enhanced bandwidth of small square monopole antenna by using inverted U-shaped slot and conductor-backed plane," *Applied Computational Electromagnetics Society (ACES) Journal*, vol. 27, no. 12, pp. 1007-1013, 2012.

[17] N. Ojaroudi, "Microstrip monopole antenna with dual band-stop function for UWB applications," *Microw. Opt. Technol. Lett*., vol. 56, pp. 818-822, 2014.

[18] N. Ojaroudi, "Circular microstrip antenna with dual band-stop performance for ultra-wideband systems," *Microw. Opt. Technol. Lett*., vol. 56, pp. 2095-2098, 2014.

[19] Y. Zhang, W. Hong, C. Yu, Z. Q. Kuai, Y. D. Don, and J. Y. Zhou, "Planar ultra-wideband antennas with multiple notched bands based on etched slots on the patch and/or split ring resonators on the feed line," *IEEE Transactions on Antennas and Propagation*, vol. 56, no. 9, pp. 3063-3068, 2008.

[20] N. Ojaroudi, S. Amiri, and F. Geran, "Reconfigurable monopole antenna with controllable band-notched performance for UWB communications," *20th Telecommunications Forum, TELFOR 2012*, Belgrade, Serbia, pp. 1176-1178, November 20-22, 2012.

[21] "Ansoft high frequency structure simulation (HFSS)," ver. 13, *Ansoft Corporation*, 2010.

[22] N. Ojaroudi, "Small microstrip-fed slot antenna with frequency band-stop function," *21st Telecommunications Forum, TELFOR 2013*, Belgrade, Serbia, pp. 1047-1050, November 27-28, 2013.

[23] N. Ojaroudi, "Design of UWB monopole antenna with dual band-stop characteristic," *In Proceedings of the Loughborough Antennas and Propagation Conference (LAPC '14)*, Loughborough, UK,

November 10-11, 2014.

[24] N. Ojaroudi, "Reconfigurable microstrip-fed monopole antenna for multimode application," *In Proceedings of the Loughborough Antennas and Propagation Conference (LAPC '14)*, Loughborough, UK, November 10-11, 2014.

[25] N. Ojaroudi, "Design of microstrip antenna for 2.4/5.8 GHz RFID applications," *German Microwave Conference, GeMic 2014*, RWTH Aachen University, Germany, March 10-12, 2014.

[26] N. Ojaroudi and N. Ghadimi, "Dual-band CPW-fed slot antenna for LTE and WiBro applications," *Microw. Opt. Technol. Lett*., vol. 56, pp. 1013-1015, 2014.

[27] N. Ojaroudi, "An UWB microstrip antenna with dual band-stop performance using a meander-line resonator," *22nd International Conference on Software, Telecommunications and Computer Networks (SoftCOM)*, Split, Croatia, September 17-19, 2014.

[28] N. Ojaroudi, "New design of multi-band PIFA for wireless communication systems," *19th International Symposium on Antenna and Propagation, ISAP2014*, Kaohsiung, Taiwan, December 2-5, 2012.

[29] N. Ojaroudi and N. Ghadimi, "UWB multi-resonance antenna with rejection of intelligent transport system band using a cross-shaped conductor-backed plane," *Microw. Opt. Technol. Lett.*, vol. 56, pp. 1641-1644, 2014.

[30] N. Ojaroudi and N. Ghadimi, "Design of CPW-fed slot antenna for MIMO system applications," *Microw. Opt. Technol. Lett*., vol. 56, pp. 1278-1281, 2014.

[31] N. Ojaroudi, H. Ojaroudi, and N. Ghadimi, "Quad-band planar inverted-F antenna (pifa) for wireless communication systems," *Progress In Electromagnetics Research Letters*, vol. 45, 51-56, 2014.

[32] N. Ojaroudi and N. Ghadimi, "Band-notched UWB slot antenna," *Microw. Opt. Technol. Lett*., vol. 56, pp. 1744-1747, 2014.

[33] N. Ojaroudi and N. Ghadimi, "UWB small slot antenna with WLAN frequency band-stop function," *Electron. Lett.*, vol. 49, pp. 1317-1318, 2013.

[34] N. Ojaroudi, H. Ojaroudi, and Y. Ojaroudi, "Very low profile ultra-wideband microstrip band-stop filter," *Microw. Opt. Technol. Lett*., vol. 56, pp. 709-711, 2014.

[35] N. Ojaroudi, M. Mehranpour, S. Ojaroudi, and Y. Ojaroudi, "Application of the protruded structures to design an UWB slot antenna with band-notched characteristic," *Applied Computational Electromagnetics Society (ACES) Journal*, vol. 29, no. 2, pp. 184-189, 2014.

[36] N. Ojaroudi, N. Ghadimi, and Y. Ojaroudi, "Bandwidth improvement of omni-directional monopole antenna with a modified ground plane," *Applied Computational Electromagnetics Society (ACES) Journal*, vol. 29, no. 4, pp. 328-334, 2014.

[37] N. Ojaroudi, N. Ghadimi, and Y. Ojaroudi, "UWB microstrip-fed slot antenna with band-rejection performance using an SRR conductor-backed plane," *Applied Computational Electromagnetics Society (ACES) Journal*, vol. 29, no. 3, pp. 203-207, 2014.

[38] N. Ojaroudi, N. Ghadimi, and Y. Ojaroudi, "Planar ultra-wideband (UWB) antenna with C-band rejection using self-complementary structures," *Applied Computational Electromagnetics Society (ACES) Journal*, vol. 29, no. 3, pp. 203-207, 2014.

Amplitude-Only Synthesis of Multi-Subaperture Antenna Array by Nonlinear Least-Square Method

Hua Guo, Chen-Jiang Guo, and Jun Ding

School of Electronics and Information
Northwestern Polytechnical University, Xi'an 710129, China
xdguohua@163.com, cjguo@nwpu.edu.cn, dingjun@nwpu.edu.cn

Abstract ― An improved nonlinear least-square method is presented to the synthesis of multi-subaperture antenna array for SAR application. This method changes the traditional nonlinear least-square method's shortness of being sensitive to its initial value. The whole aperture and the subapertures can generate different radiation beams. Also, the whole aperture and the several subapertures can work simultaneously. The mathematical model of nonlinear least-square method is given and the amplitudes of the array elements are optimized. The Peak Side Lobe Level (PSLL) is controlled effectively. The simulation results show the feasibility and effectiveness of the presented method in the synthesis of array antenna.

Index Terms ― Antenna array, multi-beam, nonlinear least-square method, pattern synthesis.

I. INTRODUCTION

Pattern synthesis of antenna arrays has been paid more and more attention in recent years. Many methods have been developed in the synthesis of antenna arrays, such as Genetic Algorithm (GA) [1], Particle Swarm Optimization (PSO) [2], and Differential Evolution (DE) algorithm [3]. These methods are global optimization algorithms and can usually get a satisfied result. However, these methods have the disadvantage of time consuming, so many other methods have been introduced into the synthesis of antenna arrays, such as Fast Fourier Transform (FFT) method [4,5], Projection Matrix Algorithm (PMA) [6], and Convex (CVX) optimization [7]. These methods are iterative methods and have the advantage of being fast. Also, some microwave simulation softwares such as HFSS and CST have been used in the analysis of array antenna [8-10].

Multi-subaperture antenna array is to divide the whole array aperture into several sub-arrays and multi-beams are usually obtained by these sub-arrays. Multi-beam array antennas have many applications in communication and radars. Several synthesis methods are introduced and some kinds of radiation patterns are synthesized [11-15]. A comparison study between phase-only and amplitude phase synthesis of symmetric dual-pattern linear antenna arrays using floating-point or real-valued genetic algorithms is presented in [11]. An iterative method based on the method of successive projections for power synthesis of reconfigurable arrays of arbitrary geometry is introduced in [12]. A novel mixed-integer optimization formulation for the optimal design of a reconfigurable antenna array with quantized phase excitations is proposed in [13]. Three approaches for the synthesis of the optimal compromise between sum and difference patterns for sub-arrayed linear and planar arrays are presented in [14]. An analytical technique based on Almost Difference Sets (ADSs) for the design of interleaved linear arrays with well-behaved and predictable radiation features is proposed in [15].

Amplitude-only optimization is one of the most popular methods in the pattern synthesis of array antenna. Because only the excitation amplitudes of the array elements are optimized, the computational complexity will be reduced greatly. Low side lobe synthesis thesis using amplitude-only tapering on the turned ON elements of large circular thinned arrays is presented in [16]. In [17], an efficient method based on Bees Algorithm (BA) for the pattern

Submitted On: May 19, 2013
Accepted On: September 6, 2014

synthesis of linear antenna arrays with the prescribed nulls is presented. An amplitude-only optimizing method is presented to synthesize the multiple beams of an array antenna for multi-mode SAR application [18].

Nonlinear least-square method is an iterative method and has no special requirements for the positions of the array elements. In this paper, improved nonlinear least-square method is employed in the synthesis of multi-subaperture antenna array, which makes the algorithm not sensitive to its initial value. The whole aperture of the antenna array is divided into several subapertures. The whole aperture and each subaperture have different radiation patterns. Also, all the beams generated by the whole array aperture and every subaperture are synthesized simultaneously. The paper is organized as follows. Section II is devoted to present the mathematical model of the nonlinear least-square method. The optimization steps are given in section III. Section IV gives the simulation results. Finally, conclusions are given.

II. MATHEMATICAL MODEL

The structure of a linear multi-subaperture array is as shown in Fig. 1. The array elements are disposed along x axis. The array antenna has N elements and the coordinate of the first element is 0. The whole array aperture is divided into S subapertures which are expressed as Sub_s, s=1,2,⋯,S. The whole array aperture can obtain a radiation pattern and each subaperture can get a different radiation beam. So, the whole array antenna can produce S+1 different beams simultaneously. If the adjacent elements spacing is d_i, i=1,2⋯,N, the position of each element can be written as:

$$x_i = (i-1)d_i,\ i = 1,2,\cdots,N. \tag{1}$$

The array factor of the whole aperture can be given by:

$$AF^{(\mathrm{Whole})}(\theta) = \sum_{n=1}^{N} A_n E_n(\theta)\exp(jkx_n\cos\theta), \tag{2}$$

where $\theta\in[0,\pi]$ is the angle respect to the array axis, $k=2\pi/\lambda$ is wave number, λ is wavelength, x_n is the position of the nth element, A_n is the complex excitation coefficient of the nth element, $E_n(\theta)$ is the radiation pattern of the nth element.

In order to simply the optimization procedure, assuming each subaperture has the same number of array elements, the array element number of each subaperture is N/S. The array factor of sth subaperture is written as:

$$AF^{(\mathrm{Sub}_s)}(\theta) = \sum_{n=N_s}^{N_s'} A_n E_n(\theta)\exp(jkx_n\cos\theta), \tag{3}$$

where $N_s=(s-1)N/S+1$ and $N_s'=sN/S$, s=1,2,⋯,S, are the lower and upper element boundary of sth subaperture, respectively.

In order to fulfill the optimization of nonlinear least-square method, the radiation angle θ is divided into M equal parts. Then, the angle of each discrete point is given by:

$$\theta_m = \frac{m-1}{M-1}\pi,\ m = 1,2,\cdots,M. \tag{4}$$

After the radiation angle is discretized, the array factors of the whole aperture and sth subaperture can be shown as follows:

$$\begin{aligned} AF^{(\mathrm{Whole})}(\theta_m) &= \sum_{n=1}^{N} A_n E_n(\theta_m)\exp(jkx_n\cos\theta_m) \\ &= \sum_{n=1}^{N} T_{mn}A_n, \end{aligned} \tag{5}$$

$$\begin{aligned} AF^{(\mathrm{Sub}_s)}(\theta_m) &= \sum_{n=N_s}^{N_s'} A_n E_n(\theta_m)\exp(jkx_n\cos\theta_m) \\ &= \sum_{n=N_s}^{N_s'} T_{mn}A_n, \end{aligned} \tag{6}$$

where $T_{mn}=E_n(\theta_m)\exp(jkx_n\cos\theta_m)$.

The sets of the equations in (5) and (6) can be expressed in the following matrix form [18]:

$$\begin{bmatrix} & \mathbf{T}^{(\mathrm{Whole})} & & \\ \mathbf{T}^{(\mathrm{Sub}_1)} & \mathbf{0} & \cdots & \mathbf{0} \\ \mathbf{0} & \mathbf{T}^{(\mathrm{Sub}_2)} & \cdots & \mathbf{0} \\ & & \vdots & \\ \mathbf{0} & \mathbf{0} & \cdots & \mathbf{T}^{(\mathrm{Sub}_S)} \end{bmatrix} \begin{bmatrix} A_1 \\ A_2 \\ A_3 \\ \vdots \\ A_N \end{bmatrix} = \begin{bmatrix} \mathbf{AF}^{(\mathrm{Whole})} \\ \mathbf{AF}^{(\mathrm{Sub}_1)} \\ \mathbf{AF}^{(\mathrm{Sub}_2)} \\ \vdots \\ \mathbf{AF}^{(\mathrm{Sub}_S)} \end{bmatrix}, \tag{7}$$

where $\mathbf{T}^{(\mathrm{Whole})}=[T_{mn}]$ is $M\times N$ matrix and $\mathbf{T}^{(\mathrm{Sub}_s)}=[T_{mn}]$, $N_s\le n\le N_s'$, s=1,2,⋯,S, is $M\times N/S$ matrix. $\mathbf{0}$ denotes a $M\times N/S$ zero matrix. $A_n=I_n\exp(j\alpha_n)$ is the complex excitation coefficient of the nth element. I_n and α_n are excitation amplitude and phase of the nth element, respectively.

In order to synthesize the radiation patterns more accurately, the normalized radiation patterns are used here. The normalized radiation patterns of the antenna array can be expressed as:

$$F_m^{(\mathrm{Whole})} = \frac{1}{AF_{\max}^{(\mathrm{Whole})}}\sum_{n=1}^{N} T_{mn}I_n e^{j\alpha_n},\ m = 1,2,\cdots,M, \tag{8}$$

$$F_m^{(\mathrm{Sub}_s)} = \frac{1}{AF_{\max}^{(\mathrm{Sub}_s)}} \sum_{n=N_s}^{N_s'} T_{mn} I_n e^{j\alpha_n}, \; s = 1, 2, \cdots, S, \quad (9)$$

where $AF_{\max}^{(\mathrm{Whole})}$ and $AF_{\max}^{(\mathrm{Sub}_s)}$ are the maximum value of $\mathbf{AF}^{(\mathrm{Whole})}$ and $\mathbf{AF}^{(\mathrm{sub}_s)}$, respectively. The normalized radiation patterns of the whole aperture and each subaperture can be expressed in the following vector form:

$$\mathbf{F} = [\mathbf{F}^{(\mathrm{Whole})} \quad \mathbf{F}^{(\mathrm{Sub}_1)} \quad \mathbf{F}^{(\mathrm{Sub}_2)} \quad \cdots \quad \mathbf{F}^{(\mathrm{Sub}_S)}]^{\mathrm{T}}, \quad (10)$$

where the superscript T denotes the transpose symbol. The total element number of vector **F** is $(S+1)\times M$.

The vector of the normalized desired radiation patterns of the whole aperture and the sth subaperture are depicted by $\mathbf{f}^{(\mathrm{Whole})}$ and $\mathbf{f}^{(\mathrm{Sub}_s)}$, $s=1,2,\cdots,S$. Similar to be shown in (10), the normalized desired radiation patterns can be expressed in the following vector form:

$$\mathbf{f} = [\mathbf{f}^{(\mathrm{Whole})} \quad \mathbf{f}^{(\mathrm{Sub}_1)} \quad \mathbf{f}^{(\mathrm{Sub}_2)} \quad \cdots \quad \mathbf{f}^{(\mathrm{Sub}_S)}]^{\mathrm{T}}. \quad (11)$$

The objective function of nonlinear least-square method is determined by the absolute error of the synthesized and desired radiation patterns which can be given by:

$$r_j(\boldsymbol{\xi}) = \left| |F_j| - f_j \right|, \; j = 1, 2, \cdots, (S+1)M, \quad (12)$$

where f_j and F_j, $j=1,2,\cdots,(S+1)M$, are the jth element of **f** and **F**, respectively. The vector of the optimized parameters is $\boldsymbol{\xi}=[I_1, I_2, \cdots, I_N]$. $|F_j|$ can be given as follows:

$$|F_j| = \frac{1}{AF_{\max}^{(\mathrm{Whole})}} \sqrt{\left(\sum_{n=1}^{N} a_n\right)^2 + \left(\sum_{n=1}^{N} b_n\right)^2}, \quad (13)$$

$$1 \le j \le M$$

$$|F_j| = \frac{1}{AF_{\max}^{(\mathrm{Sub}_s)}} \sqrt{\left(\sum_{n=N_s}^{N_s'} a_n\right)^2 + \left(\sum_{n=N_s}^{N_s'} b_n\right)^2}, \quad (14)$$

$$sM + 1 \le j \le (s+1)M, \; s = 1, 2, \cdots, S$$

where $a_n = I_n \cos(kx_n \cos\theta_m + \alpha_n)$ and $b_n = I_n \sin(kx_n \cos\theta_m + \alpha_n)$.

In this paper, the desired radiation patterns are pencil beams and the scanning angle of each radiation pattern is 90°. So, the excitation phases are set to be zero and only the excitation amplitudes are optimized.

The optimization objective is to minimize the total absolute error of the synthesized and desired radiation patterns. Considering the constraints of excitation amplitudes, the mathematical model of nonlinear least-square method can be expressed as:

$$\begin{cases} \min\left(\sum_{j=1}^{(S+1)M} r_j(\boldsymbol{\xi})\right). \\ s.t. \; 0 \le I_n \le 1, \; n = 1, 2, \cdots, N \end{cases} \quad (15)$$

In performing the beamforming of array antenna, only the good agreement between the synthesized and desired radiation pattern in the main lobe area is concerned. The shape of the radiation pattern in side lobe area is not considered. Only the maximum value of the side lobe level should be restricted. Then, the desired radiation pattern can be expressed as:

$$f_j = \begin{cases} \mathrm{HB}_j, & |F_j| > \mathrm{HB}_j \\ |F_j|, & \mathrm{LB}_j \le |F_j| \le \mathrm{HB}_j \\ \mathrm{LB}_j, & |F_j| < \mathrm{LB}_j \end{cases}, \quad (16)$$

$$j = 1, 2, \cdots, (S+1)M$$

where HB_j and LB_j are real and positive functions, which denote the upper and lower bounds of the desired radiation pattern, respectively.

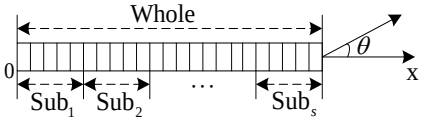

Fig. 1. Structure of a linear multi-subaperture array antenna.

III. OPTIMIZATION STEPS

In order to overcome the impact of matrix singular on the computing precision, Levenbert-Marquardt method is used to solve the model of nonlinear least-square method [19]. The algorithm steps are given as follows:

Step 1. Choose $\boldsymbol{\xi}^{(0)}$ as the initial value, let $\boldsymbol{\xi}_{\mathrm{best}}=\boldsymbol{\xi}^{(0)}$, where $\boldsymbol{\xi}_{\mathrm{best}}$ is the best solution of the optimization parameters. Calculate the initial synthesized radiation patterns of the whole aperture and subapertures by (7) and they are normalized by (8) and (9). The error between the synthesized and desired radiation patterns is calculated by (12). Set $r_{\mathrm{best}}=(r_j(\boldsymbol{\xi}^{(0)}))^{\mathrm{T}} r_j(\boldsymbol{\xi}^{(0)})$, where r_{best} is the minimum optimization error. Give $m_{\max}$ and $k_{\max}$, where $m_{\max}$ and $k_{\max}$ are the maximum iterative steps for outer and inner iterative procedure. Let m=0.

Step 2. Give $\beta \in (0,1)$, $\mu_k > 1$, $\nu > 1$ and $\varepsilon > 0$, $\varepsilon_0 > 0$, $0 < \Delta\varepsilon < 1$, let k=0. Where β, μ_k and ν are the parameters used in the optimization procedure. ε

and ε_0 are the thresholds of the outer and inner iterative procedure which are very small numerical values. $\Delta\varepsilon$ is the maximum offset value of the excitation amplitude in each outer iterative procedure.

Step 3. For j=1,2,⋯, (S+1)M, calculate $r_j(\boldsymbol{\xi}^{(k)})$ by (12) and $S(\boldsymbol{\xi}^{(k)})$ is determined by $(r_j(\boldsymbol{\xi}^{(k)}))^{\mathrm{T}} r_j(\boldsymbol{\xi}^{(k)})$.

Step 4. For j=1,2,⋯,(S+1)M, calculate $\nabla r_j(\boldsymbol{\xi}^{(k)})$, where $\nabla r_j(\boldsymbol{\xi}^{(k)})=[J_{ij}(\boldsymbol{\xi}^{(k)})]$, $J_{ij}=\partial r_j(\boldsymbol{\xi}^{(k)})/\partial \xi_i^{(k)}$, and i=1,2,⋯,N. Moreover, $\partial r_j(\boldsymbol{\xi}^{(k)})/\partial \xi_i^{(k)}$ can be determined as follows:

If $|F_j|-f_j \geq 0$, then

$$\frac{\partial r_j(\boldsymbol{\xi}^{(k)})}{\partial \xi_i^{(k)}} = \frac{\partial |F_j|}{\partial I_i^{(k)}} = \frac{1}{AF_{\max}^{(\mathrm{Whole})}} \left(\frac{\sum_{n=1}^{N} a_n \cos(kx_i \cos\theta_m + \alpha_i)}{\sqrt{(\sum_{n=1}^{N} a_n)^2 + (\sum_{n=1}^{N} b_n)^2}} + \frac{\sum_{n=1}^{N} b_n \sin(kx_i \cos\theta_m + \alpha_i)}{\sqrt{(\sum_{n=1}^{N} a_n)^2 + (\sum_{n=1}^{N} b_n)^2}} \right), \quad (17)$$

$$1 \leq j \leq M,\ 1 \leq i \leq N$$

$$\frac{\partial r_j(\boldsymbol{\xi}^{(k)})}{\partial \xi_i^{(k)}} = \frac{\partial |F_j|}{\partial I_i^{(k)}} = \frac{1}{AF_{\max}^{(\mathrm{Sub}_s)}} \left(\frac{\sum_{n=N_s}^{N_s'} a_n \cos(kx_i \cos\theta_m + \alpha_i)}{\sqrt{(\sum_{n=N_s}^{N_s'} a_n)^2 + (\sum_{n=N_s}^{N_s'} b_n)^2}} + \frac{\sum_{n=N_s}^{N_s'} b_n \sin(kx_i \cos\theta_m + \alpha_i)}{\sqrt{(\sum_{n=N_s}^{N_s'} a_n)^2 + (\sum_{n=N_s}^{N_s'} b_n)^2}} \right). \quad (18)$$

$$sM+1 \leq j \leq (s+1)M,$$

$$(s-1)N/S+1 \leq i \leq sN/S,\ s=1,2,\cdots,S$$

If $|F_j|-f_j<0$, a minus is added to the right hand side of (17) and (18), $\partial r_j(\boldsymbol{\xi}^{(k)})/\partial \xi_i^{(k)}$ can be obtained.

Step 5. Calculate $\nabla S(\boldsymbol{\xi}^{(k)})=(\nabla r_j(\boldsymbol{\xi}^{(k)}))^{\mathrm{T}} r_j(\boldsymbol{\xi}^{(k)})$.

Step 6. Let $\mathbf{Q}=(\nabla r_j(\boldsymbol{\xi}^{(k)}))^{\mathrm{T}} \nabla r_j(\boldsymbol{\xi}^{(k)})$, solve equation $[\mathbf{Q}+\mu_k \mathbf{I}]\mathbf{d}^{(k)}=-\nabla S(\boldsymbol{\xi}^{(k)})$, where $\mathbf{I}$ represents the unit diagonal matrix. Then, $\mathbf{d}^{(k)}$ can be calculated.

Step 7. Set $\boldsymbol{\xi}^{(k+1)}=\boldsymbol{\xi}^{(k)}+\mathbf{d}^{(k)}$, if $\max(\mathbf{d}^{(k)})<\varepsilon$ or $k>k_{\max}$, go to step 10, otherwise, go to step 8.

Step 8. If $S(\boldsymbol{\xi}^{(k)})<S(\boldsymbol{\xi}^{(k)})+\beta(\nabla S(\boldsymbol{\xi}^{(k)}))^{\mathrm{T}}\mathbf{d}^{(k)}$, set $\mu_k=\mu_k/\nu$, go to step 9, otherwise, set $\mu_k=\mu_k\times\nu$, go to step 6.

Step 9. Let $k=k+1$, go to step 3.

Step 10. If $S(\boldsymbol{\xi}^{(k+1)})<\varepsilon_0$ or $m>m_{\max}$, $\boldsymbol{\xi}_{\mathrm{best}}=\boldsymbol{\xi}^{(k+1)}$, terminate iteration, otherwise, if $S(\boldsymbol{\xi}^{(k+1)})<r_{\mathrm{best}}$, set $\boldsymbol{\xi}_{\mathrm{best}}=\boldsymbol{\xi}^{(k+1)}$, $\boldsymbol{\xi}^{(0)}=\boldsymbol{\xi}^{(0)}+\Delta\varepsilon\times\boldsymbol{\xi}^{(0)}\times\mathrm{rand}(0,1)$, where rand(0,1) is uniformly distributed random numbers between [0,1], normalize the excitation amplitudes, let $m=m+1$, go to step 2.

Among the above steps, another layer of iteration is added to the traditional nonlinear least-square method. If the solution does not meet the requirements, another vector nearer the former initial value is selected as the initial value and the computation is repeated. The best solution of all the iterations is saved as the ultimate result. This improves the traditional nonlinear least-square method's shortness of dependence on the initial value and increases the optimization ability of nonlinear least-square method.

IV. SIMULATION RESULTS

In this section, several simulation results are presented. The achieved results show the effectiveness and feasibility of the proposed method. Let us refer to the linear array of Fig. 1, consisting of N elements and S subapertures. The adjacent elements spacing is chosen as $\lambda/2$. Assuming all elements are isotropic sources; i.e., $E_n(\theta)=1$. The parameters used in those above expressions are as follows: $\mu_k=|r_j(\boldsymbol{\xi}^{(k)})|$, $\nu=1.5$, $\Delta\varepsilon=0.3$, $\varepsilon=10^{-6}$, $\varepsilon_0=0.01$, $M=361$, $k_{\max}=500$, $m_{\max}=200$. A normal personal computer Intel Core i3 530 @ 2.93 GHz CPU and 2 GB of RAM is used and the synthesis is programmed by MATLAB version 7.1.

A. Simulation result for N=60 and S=3

In this simulation example, the whole array aperture is divided into 3 subapertures. So, the number of the radiation patterns to be synthesized is 4. The Peak Side Lobe Level (PSLL) of the desire radiation pattern is selected as –25 dB. Every subaperture has 20 elements. Figure 2 shows the excitation amplitudes distribution of the antenna array. From this figure, we can see that Sub_1 has the minimum amplitudes values. So, the gain of Sub_1 is the smallest. Figure 3 shows the radiation patterns for the whole aperture and

subapertures. The beam parameters of this multi-subaperture antenna array are given in Table 1. We can find that the PSLL of all the synthesized beams is lower than –16 dB. The 3 dB beam width is less than 3° for the whole aperture and is less than 6° for each subaperture. To get this simulation result, the simulation time is about 710 seconds. The dynamic range ration (I_{max}/I_{min}, DRR) of this antenna array is 16.7.

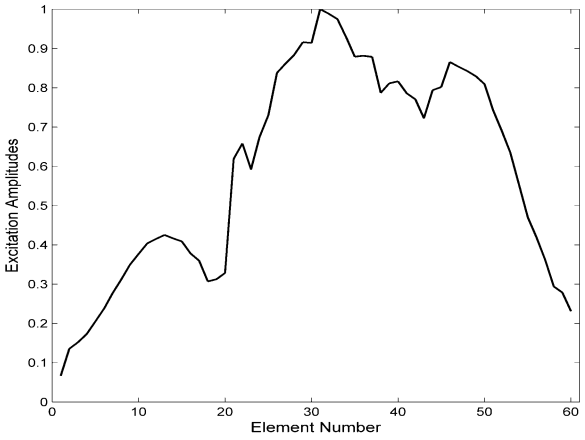

Fig. 2. Excitation amplitudes distribution for N=60 and S=3.

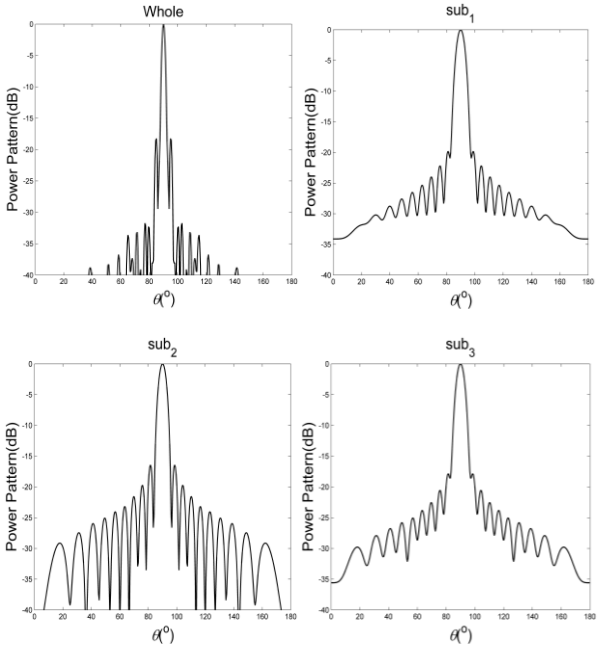

Fig. 3. Radiation patterns for N=60 and S=3.

Table 1: Beam parameters for N=60 and S=3

Beam Parameters	Whole	Sub_1	Sub_2	Sub_3
PSLL (dB)	-18.2	-19.8	-16.4	-17.8
Gain (dB)	31.0	15.6	24.4	22.1
3 dB beam width (°)	2.11	5.96	5.35	5.78
Main beam width (°)	8.0	15.0	13.0	14.0

B. Simulation result for N=60 and S=5

In order to indicate the feasibility of the algorithm in the synthesis of antenna array, another simulation example is introduced. In this simulation example, the whole array aperture is divided into 5 subapertures. So, the number of the radiation patterns to be synthesized is 6. The PSLL of the desired radiation pattern is also selected as –25 dB. The element number of every subaperture is 12. The excitation amplitudes distribution is shown in Fig. 4. From this figure, we can find that the excitation amplitudes distribution for each subaperture has a peak value. Figure 5 depicts the radiation patterns for the whole aperture and the five subapertures. The beam parameters of the radiation patterns are given in Table 2. It can be found from Table 2 that the PSLL for the radiation patterns is lower than -16 dB. The 3 dB beam width is less than 2° for the whole aperture and is less than 10° for the subaperture. Sub_5 has the minimum gain of 13.4 dB. In order to obtain these six radiation patterns, the simulation time is about 990 seconds. The dynamic range ration of the excitation amplitudes is 6.5.

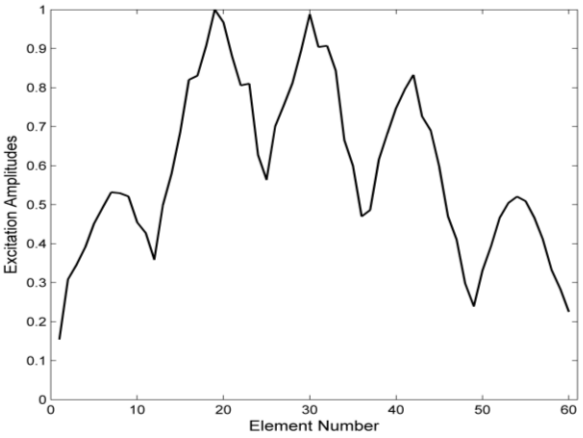

Fig. 4. Excitation amplitudes distribution for N=60 and S=5.

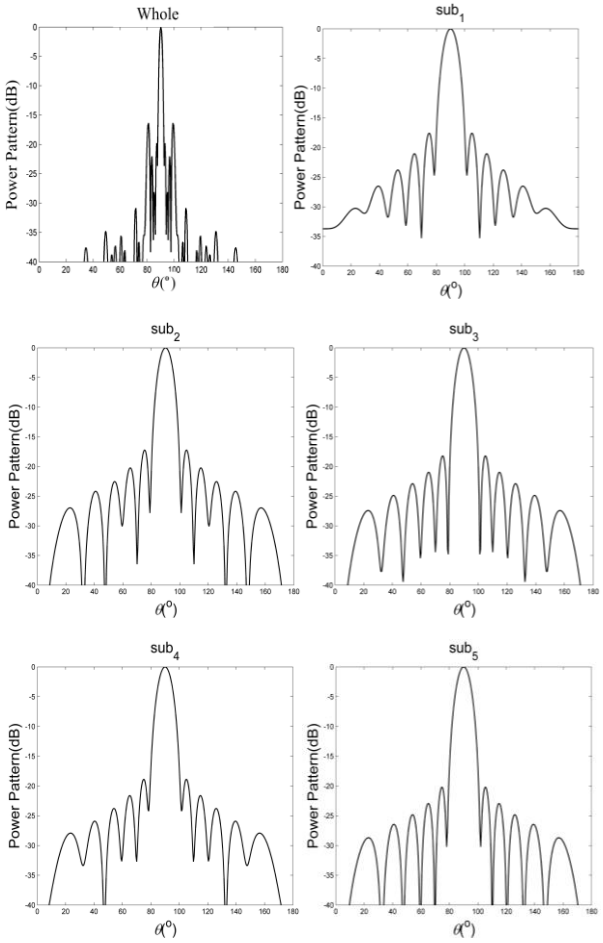

Fig. 5. Radiation patterns for N=60 and S=5.

Table 2: Beam parameters for N=60 and S=5

Beam Parameters	Whole	Sub_1	Sub_2	Sub_3	Sub_4	Sub_5
PSLL (dB)	-16.3	-17.6	-17.2	-18.2	-18.9	-20.2
Gain (dB)	31.0	13.9	19.5	19.2	17.3	13.4
3 dB beam width (°)	1.96	9.60	9.24	9.37	9.60	9.71
Main beam width (°)	10.0	23.0	22.0	22.0	23.0	24.0

C. Simulation result for N=90 and S=5

In this example, the element number of the array antenna is increased to 90 and the number of the subaperture is 5. So, each subaperture has 18 elements. Figure 6 depicts the excitation amplitudes distribution. From Fig. 6, we can find that the excitation dynamic range ration is 12.9. The radiation patterns of this kind of antenna array are shown in Fig. 7. The beam parameters of the radiation patterns are given in Table 3. Compared with the synthesis result when N=60, we can get that the PSLL reduces to −17.2 dB and the beam width is narrower. The total computational time is about 1400 seconds to get these six radiation patterns.

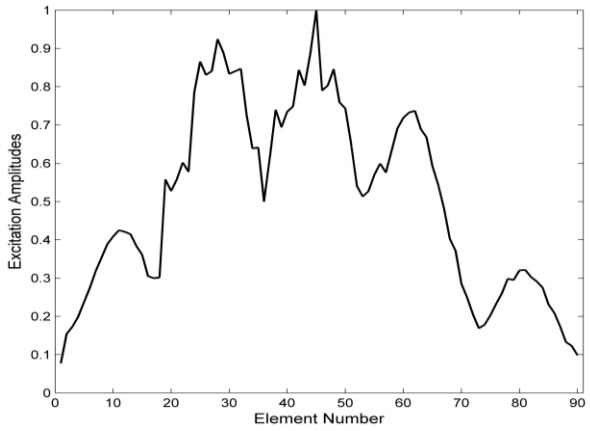

Fig. 6. Excitation amplitudes distribution for N=90 and S=5.

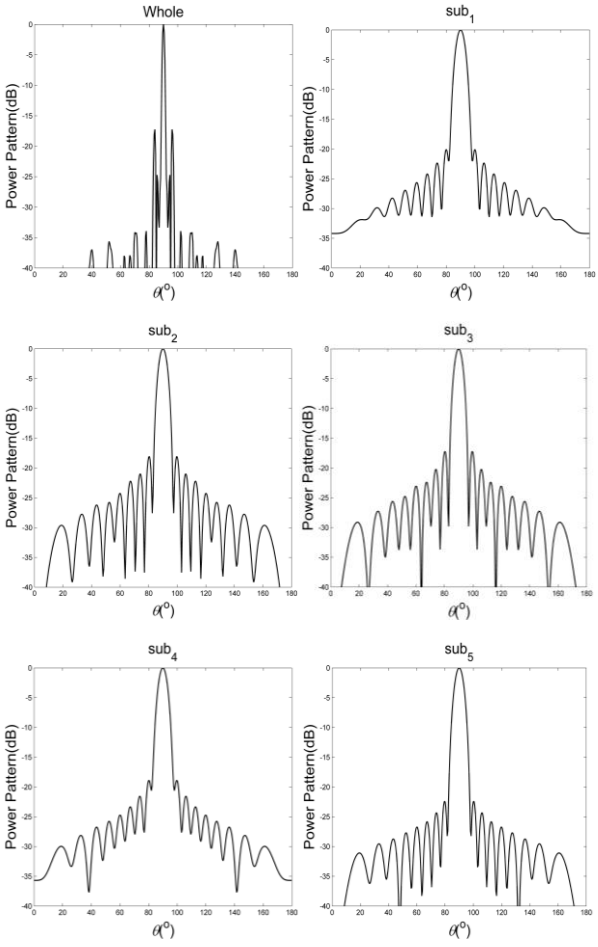

Fig. 7. Radiation patterns for N=90 and S=5.

Table 3: Beam parameters for N=90 and S=5

Beam Parameters	Whole	Sub_1	Sub_2	Sub_3	Sub_4	Sub_5
PSLL (dB)	-17.2	-20.1	-18.1	-17.2	-18.9	-22.4
Gain (dB)	33.2	14.8	22.3	22.4	19.8	12.3
3 dB beam width (°)	1.86	5.58	6.16	6.22	6.44	6.43
Main beam width (°)	5.0	16.0	15.0	15.0	16.0	16.0

V. CONCLUSION

Multi-subaperture antenna array is synthesized by an improved nonlinear least-square method. The whole array aperture is divided into several subapertures. A new method is given to determine the desired function for the nonlinear least-square method. The whole aperture and the subapertures can generate different radiation patterns. The excitation amplitudes are optimized in order to reduce the PSLL of the radiation beams. The PSLL is lower than −16 dB for the synthesized radiation patterns. Also, the beam width of the radiation patterns can be controlled effectively. When N=60, the dynamic range ratio of the excitation amplitudes distribution is less than 17 for S=3 and is less than 7 for S=5. When N=90 and S=5, the dynamic range ration is less than 13. Also, the beam width becomes narrower as the increase of element number of the whole array aperture or each subaperture. Moreover, this method can also be used in the synthesis of phase-only multi-beam antenna arrays.

ACKNOWLEDGMENT

This work was supported by the National Defense Pre-Research Foundation of China under Grant No. 9140A01010412HK03004.

REFERENCES

[1] S. Baskar, A. Alphones, and P. N. Suganthan, "Genetic-algorithm-based design of a reconfigurable antenna array with discrete phase shifters," *Microwave and Optical Technology Letters*, vol. 45, no. 6, pp. 461-465, 2005.

[2] W. B. Wang, Q. Feng, and D. Liu, "Synthesis of thinned linear and planar antenna arrays using binary PSO algorithm," *Progress In Electromagnetics Research*, vol. 127, pp. 371-387, 2012.

[3] R. Li, L. Xu, X. W. Shi, N. Zhang, and Z. Q. Lv, "Improved differential evolution strategy for antenna array pattern synthesis problems," *Progress In Electromagnetics Research*, vol. 113, pp. 429-441, 2011.

[4] W. P. M. N. Keizer, "Fast low-sidelobe synthesis for large planar array antennas utilizing successive fast fourier transforms of array factor," *IEEE Trans. Antennas Propagat.*, vol. AP-55, no. 3, pp. 715-722, 2007.

[5] K. Yang, Z. Q. Zhao, and Q. H. Liu, "Fast pencil beam pattern synthesis of large unequally spaced antenna arrays," *IEEE Trans. Antennas Propagat.*, vol. AP-61, no. 2, pp. 627-634, 2013.

[6] A. K. Bhattacharyya, "Projection matrix method for shaped beam synthesis in phased arrays and reflectors," *IEEE Trans. Antennas Propagat.*, vol. AP-55, no. 3, pp. 675-683, 2007.

[7] S. E. Nai, W. Ser, Z. L. Yu, and H. Chen, "Beam pattern synthesis for linear and planar arrays with antenna selection by convex optimization," *IEEE Trans. Antennas Propagat.*, vol. AP-58, no. 12, pp. 3923-3930, 2010.

[8] S. E. Hosseininejad, N. Komjani, H. Oraizim, and M. T. Noghani, "Optimization design of SIW longitudinal slot array antennas with specified radiation patterns," *Applied Computational Electromagnetic Society (ACES) Journal*, vol. 27, no. 4, pp. 320-325, 2012.

[9] F. Tokan, F. Gunes, B. Turetken, and K. Surmeli, "A simple synthesis of a high gain planar array antenna for volume scanning radars," *Applied Computational Electromagnetic Society (ACES) Journal*, vol. 27, no. 3, pp. 271-277, 2012.

[10] F. Tokan and F. Gunes, "Mutual coupling compensation in non-uniform antenna arrays using inter-element spacing restrictions," *Applied Computational Electromagnetic Society (ACES) Journal*, vol. 26, no. 7, pp. 596-602, 2011.

[11] G. K. Mahanti, A. Chakrabarty, and S. Das, "Phase-only and amplitude-phase synthesis of dual-pattern linear antenna arrays using floating-point genetic algorithms," *Progress In Electromagnetics Research*, vol. 68, pp. 247-259, 2007.

[12] G. Buttazzoni and R. Vescovo, "Power synthesis for reconfigurable arrays by phase-only control with simultaneous dynamic range ratio and near-field reduction," *IEEE Trans. Antennas Propagat.*, vol. AP-60, no. 2, pp. 1161-1165, 2012.

[13] S. Baskar, A. Alphones, and P. N. Suganthan, "Genetic-algorithm-based design of a reconfigurable antenna array with discrete phase shifters," *Microwave and Optical Technology Letters*, vol. 45, no. 6, pp. 461-465, 2005.

[14] G. Oliveri and L. Poli, "Synthesis of monopulse sub-arrayed linear and planar array antennas with optimized sidelobes," *Progress In Electromagnetics Research*, vol. 99, pp. 109-129,

2009.
[15] G. Oliveri and A. Massa, "Fully interleaved linear arrays with predictable sidelobes based on almost difference sets," *IET Radar, Sonar and Navigation*, vol. 4, no. 5, pp. 649-661, 2010.
[16] W. P. M. N. Keizer, "Amplitude-only low sidelobe synthesis for large thinned circular array antennas," *IEEE Trans. Antennas Propagat*., vol. AP-60, no. 2, pp. 1157-1161, 2012.
[17] K. Guney and M. Onay, "Amplitude-only pattern nulling of linear antenna arrays with the use of bees algorithm," *Progress In Electromagnetics Research*, vol. 70, pp. 21-36, 2007.
[18] W. J. Gao and X. M. Liu, "Amplitude-only optimizing method of multi-subaperture multi-beam antenna for SAR application," *The International Conference on Electronics, Communication and Control*, Ningbo, China, pp. 117-120, September 2011.
[19] D. W. Marquardt, "An algorithm for least-squares estimation of nonlinear parameters," *Journal of the Society for Industrial and Applied Mathematics*, vol. 11, no. 2, pp. 431-441, 1963.

Hua Guo Received his B.S. degree in Applied Physics from Xidian University (XDU) in 2004. In 2007, he obtained his M.S. degree in Radio Physics from XDU. He is now working towards his Ph.D. degree in Electromagnetic Fields and Microwave Techniques at Northwestern Polytechnical University (NWPU). His research interests include electromagnetic theory and calculation, array antenna design, phased arrays and radars.

Chen-Jiang Guo Received his B.Eng. degree in Electronic Engineering in 1984 from Northwestern Polytechnical University (NWPU). He obtained his M.S. degree in Electromagnetic Fields and Microwave Techniques in 1987 from the NWPU. In 2007, he received his Ph.D. degree in Circuits and Systems from NWPU. He is now a Professor of Electromagnetic Fields and Microwave Techniques at NWPU. His research interests include electromagnetic theory, antenna theory and design, microwave circuit design and Electromagnetic Compatibility (EMC).

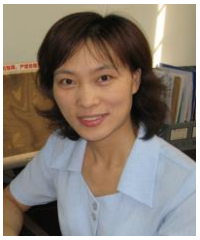

Jun Ding Received her B.Eng. degree in Electronic Engineering in 1986 from Northwestern Polytechnical University (NWPU). She obtained her M.S. degree in Electromagnetic Fields and Microwave Techniques in 1989 from NWPU. In 2005, she received her Ph.D. degree in Circuits and Systems from NWPU. She is now a Professor of Electromagnetic Fields and Microwave Techniques at NWPU. Her research interests include electromagnetic calculation, antenna theory and design, microwave circuit design and Electromagnetic Compatibility (EMC).

Time Domain Analysis of GaAS MESFET Transistors Excited by an Incident Electromagnetic Field

L. Mirzavand, A. Abdipour, and R. Mirzavand

Institute of Communications Technology and Applied Electromagnetics
Electrical Engineering Department
Amirkabir University of Technology, Tehran, 15914, Iran
lmirzavand@aut.ac.ir, abdipour@aut.ac.ir, rmirzavand@aut.ac.ir

Abstract ─ A numerical method for the fully distributed modeling of Field Effect Transistor (FET) excited by an incident electromagnetic field using a Finite-Difference Time-Domain (FDTD) method is described. The transistor is modeled using the fully distributed model which consists of a configuration of the conventional equivalent circuit of the transistor and three coupled lines as each distributed element. The distributed source terms represent the coupling with an electromagnetic field in the equation which can be used in the Electromagnetic Interference (EMI) analysis. As a numerical example, the method is applied to a GaAs MESFET and the time domain results are presented.

Index Terms ─ Coupled active transmission lines, Electromagnetic Interference (EMI), Field Effect Transistor (FET), Finite-Difference Time-Domain (FDTD), incident wave, transistor distributed modeling.

I. INTRODUCTION

Modeling and prediction of undesired Electromagnetic Interference (EMI), such as crosstalk and external incident field, is very important to increasing the frequency and high-density packaging of microwave circuits [1]-[3]. Perfect analysis of the microwave transistors is one of major steps in the analysis of a microwave active circuit. In the very high (micro/mm-wave) frequencies, the dimension of the electrodes of a transistor becomes comparable to the wave length. Therefore, the device modeling must include the effect of wave propagation. This effect is considered in the global modeling of mm-wave circuits, but a huge CPU time is necessary for this very slow full wave analysis [4]-[5]. Recently, a time domain fully-distributed model for transistors was presented to reduce the simulation time with a good degree of accuracy in 1-40 GHz [6]-[7]. The fully distributed model considers three coupled lines while the number of slices has been increased to the infinity [6]. This model can be easily implemented with a fast FDTD simulation while describing the transistor behavior accurately. On the other hand, the FDTD solution of some coupled transmission lines has the ability to consider an external incident field in its equations [8]. This electromagnetic fields may be caused by reflections of our circuit in a box [9], by other circuits [10]-[11], or by the lightning strike [12]-[13]. This paper presents a time domain fully-distributed model for a transistor excited by an incident electromagnetic field by considering the propagation along the electrodes. First, the differential equations are derived for a MESFET using the transmission line theory. Then, the FDTD approach is applied to solve the equations in the time domain. Finally, the simulation results for an example transistor are presented. The method can be extended to other active devices with transmission line model [14].

Although the model has some approximates, such as using a one dimensional model and ignoring the secondary scattering, to the best of authors' knowledge, this is the first publication that the excitation effects on a transistor have been considered and simulated in a very small simulation time. However, more accurate results can be obtained by modifying the model in two or three dimensions and considering multiple

Submitted On: October 3, 2013
Accepted On: September 8, 2014

scattering effects of the structure.

II. FULLY DISTRIBUTED MODEL

A typical millimeter-wave FET excited by an incident electromagnetic field has been shown in Fig. 1. The fully distributed model of a millimeter-wave field effect transistor is one of the accurate models applied to consider the distributed and wave propagation effects on device behaviour. The following part shows that this model can also be used in the EMI simulations of active devices.

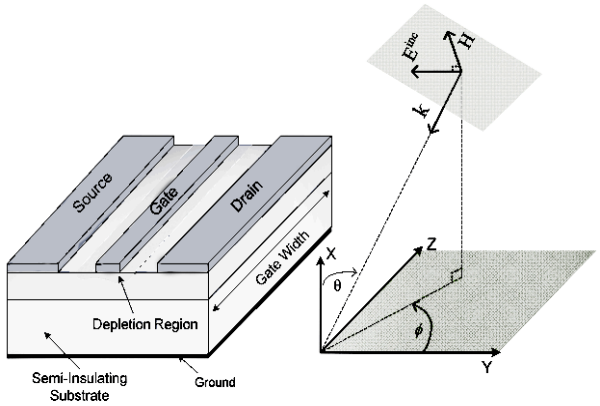

Fig. 1. The structure of a typical millimeter-wave FET excited by a plane wave.

The fully distributed model contains infinite cells cascaded together [6]. Each cell has two parts: the passive part which contains the coupled electrode transmission lines, resistance and internal inductance of electrodes, and the active part or an intrinsic GaAs FET equivalent circuit, whose elements are per unit length. We assume a linear circuit as equivalent circuit of a FET similar to [7], and add the incident wave to its equations (Fig. 2). For a transistor with electrodes in the z-direction excited with an incident wave, the time domain equations can be written as:

$$\frac{\partial}{\partial z}V(z,t)+L\frac{\partial}{\partial t}I(z,t)+RI(z,t)=\underbrace{-\frac{\partial}{\partial z}V_T(z,t)+E_L(z,t)}_{V_F(z,t)}, \quad (1)$$

$$\frac{\partial}{\partial z}I'(z,t)+C\frac{\partial}{\partial t}V'(z,t)+GV'(z,t)=\underbrace{-C\frac{\partial}{\partial t}V_T'(z,t)}_{I_F(z,t)}, \quad (2)$$

where $V_F(z,t)$ and $I_F(z,t)$ are 3×1 vectors containing the effects of the incident field;

$$V(z,t)=[V_d\ V_g\ V_s]^T(z,t), \quad (3)$$

$$I(z,t)=[I_d\ I_g\ I_s]^T(z,t), \quad (4)$$

$$V'(z,t)=[V_d\ V_g\ V_s\ V_g']^T(z,t), \quad (5)$$

$$I'(z,t)=[I_d\ I_g\ I_s\ 0]^T(z,t), \quad (6)$$

$$V_T(z,t)=[V_{Td}\ V_{Tg}\ V_{Ts}]^T(z,t), \quad (7)$$

$$E_L(z,t)=[E_{Ld}\ E_{Lg}\ E_{Ls}]^T(z,t), \quad (8)$$

$$V_T'(z,t)=[V_{Td}\ V_{Tg}\ V_{Ts}\ 0]^T(z,t), \quad (9)$$

are the functions of position z along the device and the passive parameters are defined as:

$$L=\begin{bmatrix} L_d & M_{gd} & M_{ds} \\ M_{gd} & L_g & M_{gs} \\ M_{ds} & M_{gs} & L_s \end{bmatrix}, \quad (10a)$$

$$C=\begin{bmatrix} C_{11} & -C_{12} & -C_{13} & 0 \\ -C_{12} & C_{22} & -C_{23} & C_{gs} \\ -C_{13} & -C_{23} & C_{33} & -C_{gs} \\ 0 & 0 & 0 & R_iC_{gs} \end{bmatrix}, \quad (10b)$$

$$R=\begin{bmatrix} R_d & 0 & 0 \\ 0 & R_g & 0 \\ 0 & 0 & R_s \end{bmatrix}, \quad (10c)$$

$$G=\begin{bmatrix} G_{ds} & 0 & -G_{ds} & G_m \\ 0 & 0 & 0 & 0 \\ -G_{ds} & 0 & G_{ds} & -G_m \\ 0 & -1 & 1 & 1 \end{bmatrix}, \quad (10d)$$

where $C_{11}=C_{dp}+C_{dsp}+C_{dg}+C_{dgp}$, $C_{22}=C_{gp}+C_{gsp}+C_{dg}+C_{dgp}$, $C_{33}=C_{sp}+C_{ds}+C_{dsp}+C_{gsp}$, $C_{12}=C_{dg}+C_{dgp}$, $C_{13}=C_{ds}+C_{dsp}$, and $C_{23}=C_{gsp}$. In the above equations, V_d, I_d, V_g, I_g, V_s, and I_s are the drain, gate and source voltages and currents, respectively. The values of V_T and E_L describe the incident field excitation.

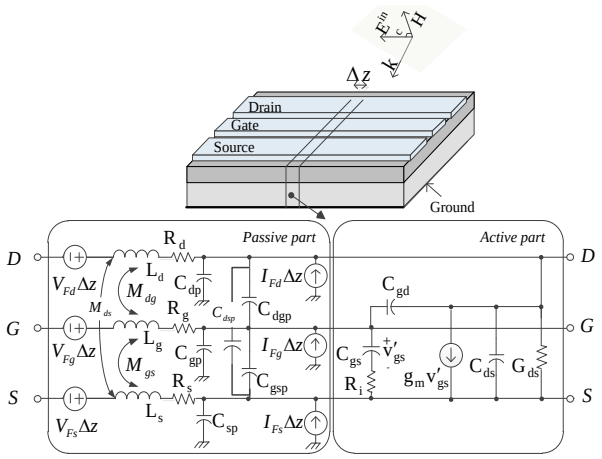

Fig. 2. The equivalent circuit of a differential slice in the fully distributed model with an incident field.

III. THE FDTD EQUATION

The solution of (1) can be determined by using an iterative finite difference procedure [6]. In this method, the transmission line is divided into small elements along the length of the line and similarly the time is divided into small steps. In order to insure stability in the FDTD solution of the equations, the discrete voltage and current solution points are not physically located at the same point, but they are staggered one-half cell apart. In addition, the discrete voltages and currents must be similarly staggered or "interlaced" in time with the time points for the voltages and one-half temporal cell apart spaced points for the currents. The boundary conditions must be applied at the first and last nodes. Hence, the currents I_0 and I_{Nz+1} are calculated by V_{in} and R_{in} at the beginning of gate, and R_L at the end of drain, respectively (Fig. 3). Approximation of derivatives in (1) by the finite differences gives the following equations:

$$V_1'^{n+1} = \left(\frac{C}{\Delta t}+\frac{G}{2}+\frac{1}{R_s'\Delta z}\right)^{-1} \left\{ \begin{array}{l} \left(\frac{C}{\Delta t}-\frac{G}{2}-\frac{1}{R_s'\Delta z}\right)V_1'^{n} \\ -\frac{2}{\Delta z}\left(I_1'^{\,n+\frac{1}{2}}-\frac{V_{in}'^{n}+V_{in}'^{n+1}}{2R_s'}\right) \\ -\frac{C}{\Delta t}\left(V_{T,1}'^{\,n+1}(z,t)-V_{T,1}'^{\,n}(z,t)\right) \end{array} \right\}, \quad (11)$$

$$V_k'^{n+1} = \left(\frac{C}{\Delta t}+\frac{G}{2}\right)^{-1} \left\{ \begin{array}{l} \left(\frac{C}{\Delta t}-\frac{G}{2}\right)V_k'^{n} \\ -\frac{2}{\Delta z}\left(I_k'^{\,n+\frac{1}{2}}+I_{k-1}'^{\,n+\frac{1}{2}}\right) \\ -\frac{C}{\Delta t}\left(V_{T,k}'^{\,n+1}(z,t)-V_{T,k}'^{\,n}(z,t)\right) \end{array} \right\}, \quad (12)$$

$$V_{N_z+1}'^{\,n+1} = \left(\frac{C}{\Delta t}+\frac{G}{2}\right)^{-1} \left\{ \begin{array}{l} \left(\frac{C}{\Delta t}-\frac{G}{2}\right)V_{N_z+1}'^{n}+\frac{2}{\Delta z}I_{N_z}'^{\,n+0.5} \\ -\frac{C}{\Delta t}\left(V_{T,N_z+1}^{\,n+1}(z,t)\right. \\ \left.-V_{T,N_z+1}^{\,n}(z,t)\right) \end{array} \right\}, \quad (13)$$

$$I_k^{\,n+1.5} = \left(\frac{L}{\Delta t}+\frac{R}{2}\right)^{-1} \left\{ \begin{array}{l} \left(\frac{L}{\Delta t}-\frac{R}{2}\right)I_k^{\,n+0.5}+\left(E_{L,k}^{\,n+1.5}(z,t)\right. \\ \left.+E_{L,k}^{\,n+0.5}(z,t)\right)-\frac{1}{\Delta z}\left(V_{k+1}^{\,n+1}-V_k^{\,n+1}\right. \\ \left.+V_{T,k+1}^{\,n+1}(z,t)-V_{T,k}^{\,n+1}(z,t)\right) \end{array} \right\}, \quad (14)$$

where

$$V_k^{\,n} = V[(k-1)\Delta z, n\Delta t], \quad (15)$$

$$I_k^{\,n} = I[(k-\frac{1}{2})\Delta z, n\Delta t], \quad (16)$$

$$\left[V_{T,k}^{\,n}\right]_i = x_i E_x^{\,inc}(x_i, y_i, (k-1)\Delta z, n\Delta t)) + y_i E_y^{\,inc}(x_i, y_i, (k-1)\Delta z, n\Delta t)), \quad (17)$$

$$\left[E_{L,k}^{\,n}\right]_i = E_z^{\,inc}(x_i, y_i, (k-0.5)\Delta z, n\Delta t)) - E_z^{\,inc}(0,0,(k-0.5)\Delta z, n\Delta t)), \quad (18)$$

where coordinates x_i and y_i describe the locations of the individual conductors. It should be noted that the excitation due to fields should be computed as the incident field, thus, all conductors

should be removed when computing the $V_{T,K}$ and $E_{L,K}$ vectors.

In general, the accuracy of the solution depends on having sufficiently small spatial and temporal cell sizes. It means that we have to consider the Courant condition, $\Delta t<(\Delta z/v_p)$, where v_p is the phase velocity of the medium. In the case of multi-conductor lines, more than one velocity exists on the lines [1]. In fact we can obtain the mode velocities by calculating the eigenvalues of the product matrix *LC*. Therefore, we consider the largest of the mode velocities to satisfy the Courant condition.

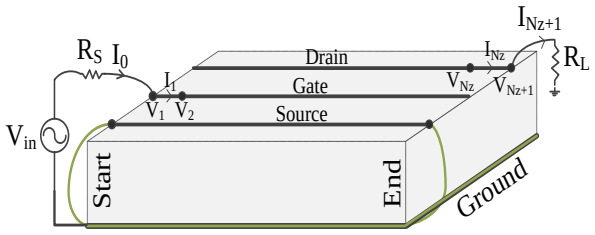

Fig. 3. The circuits used as boundary conditions.

IV. NUMERICAL RESULTS

In this part a GaAs MESFET (NE710) excited by an incident plane wave was modeled using the FDTD method for active transmission lines. The distance between the electrodes and ground plane, which is important in the calculation of the effects of incident field, has been considered as 140 μm and the width of gate is 240 μm. Using Δz=10 μm, we have 24 cells along the *z*-direction. Both input and output nodes were connected to the center of gate and drain electrodes. The source electrode is grounded at the beginning and the end. The element values used in the fully distributed model are shown in Table 1 [6]. The transistor is biased at V_{ds}=3 V and I_{ds}=10 mA, and the incident wave is considered as a sinusoidal pulse at the frequency of 40 GHz. The incidence direction is θ=90º, ϕ=90º, and η=90º. The amplitude of the incident wave is selected in such a way that produces a voltage of 1 mV at the start of the gate line. The numerical results of voltage and current at the start and end of the drain are shown in Figs. 4 and 5. It can be seen that the amplitude of output voltage at the drain line is equal to 2.03 mV. A comparison of the formulation of this paper with the results in the literature can be made when the amplitude of the incident wave is small with respect to the amplitude of the local oscillator, which is connected to the beginning of the gate. The transistor is excited by a local oscillator at the frequency of 25 GHz to make 100 mV at the beginning of the gate. Therefore, the incident wave is very small with respect to the excited signal and as shown in Fig. 6, the results of this work's formulation is very close to the results of [6]. The frequency response of transistor can be calculated using a Gaussian waveform as the excitation. The Gaussian pulse is considered by the expression $\exp[-\alpha(ndt-\beta dt)^2]$ where β=8 and $\alpha=(4/\beta/dt)^2$. The incidence direction is θ=90º, ϕ=90º, and η=90º. Simulation result of wide frequency band is shown in Fig. 7. The maximum output is appeared in 69 GHz. Moreover, the optimal gate width of transistor can be finding for the operation at a desired frequency. Figure 8 shows the voltage of drain's end with respect to the gate width, at 25 GHz, which has a maximum value at 390 μm.

Table 1: Per unit length values of distributed model for NE710 (at V_{ds}=3 V and I_{ds}=10 mA) [6]

Element	Value
C_{gs}	0.771 nF/m
C_{ds}, C_{gd}	0.0178 nF/m
g_m	146.42 S/m
R_i	0.002 Ω/m
L_d	780 nH/m
L_g	161 nH/m
L_m	360 nH/m
C_{gp}	29.6 pF/m
C_{dp}	148 pF/m
C_{gdp}	29 pF/m
R_d	900 Ω/m
R_g	34300 Ω/m
C_{gpk}	0.036 pF/m
C_{dpk}	0.0296 pF/m
L_{gpk}	0.766 nH/m
L_{dpk}	0.869 nH/m

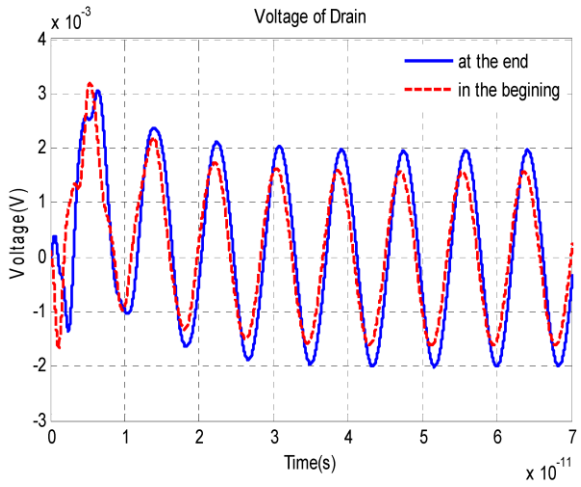

Fig. 4. Voltage of the drain line.

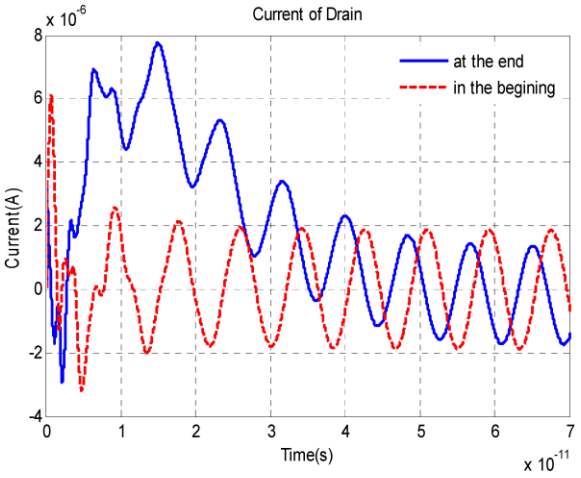

Fig. 5. Induced current on the drain line.

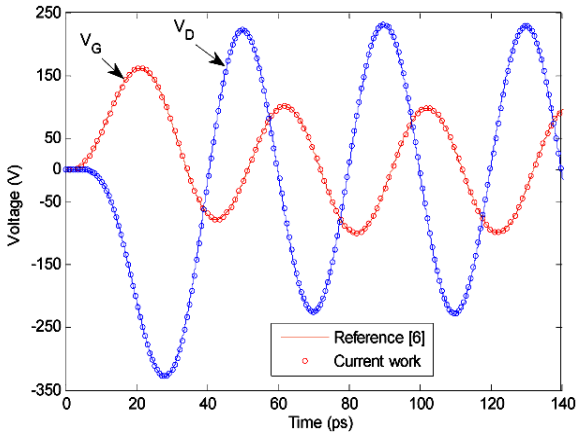

Fig. 6. Voltage in the beginning of gate (V_G) and end of drain (V_D).

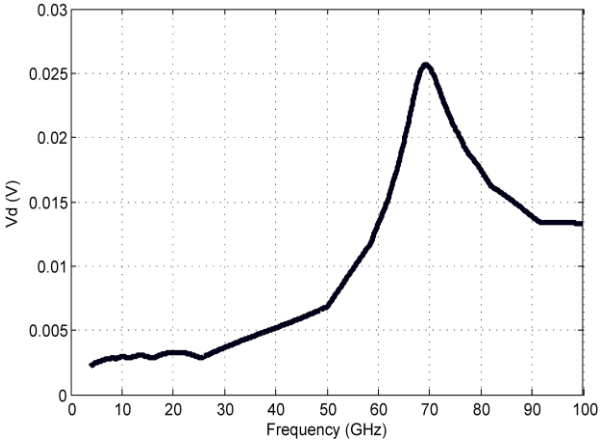

Fig. 7. Voltage at the end of rain with respect to the frequency.

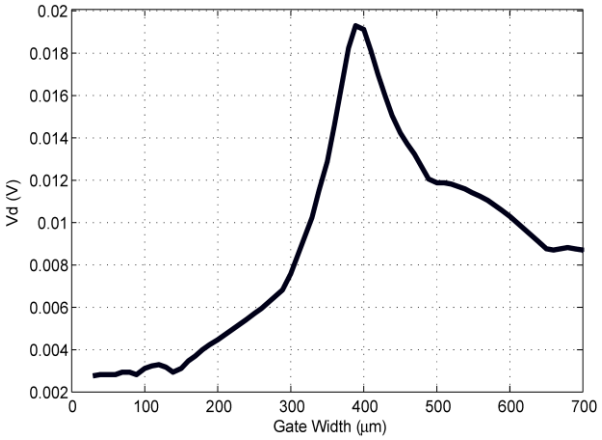

Fig. 8. Voltage at the end of drain with respect to the gate width.

IV. CONCLUSION

An accurate method for transient analysis of millimeter wave transistors excited by an external wave has been described using the FDTD. The method can be used in the EMI analysis of high frequency active circuits which has some transistors. Also, it is usable in the calibration steps of a micro/mm-wave measurement when the active device is tested in an environment with a strong EMI, which may be caused by radio transmitters. The effect of gate width can be studied with presented method, which is helpful in a transistor design.

REFERENCES

[1] C. R. Paul, "Analysis of multiconductor

transmission lines," *John Wiley Interscience*, NY, 1994.

[2] W. Luo, W. Y. Yin, M. D. Zhu, and J. Y. Zhao, "Hybrid tdie-TDPO method for studying on transient responses of some wire and surface structures illuminated by an electromagnetic pulse," *Progress In Electromagnetics Research*, vol. 116, 203-219, 2011.

[3] T. Eudes, B. Ravelo, and A. Louis, "Transient response characterization of the high-speed interconnection rlcg-model for the signal integrity analysis," *Progress In Electromagnetics Research*, vol. 112, 183-197, 2011.

[4] R. Mirzavand, A. Abdipour, G. Moradi, and M. Movahhedi, "Full-wave semicoductor devices simulation using ADI-FDTD method," *Progress In Electromagnetics Research M*, vol. 11, 191-202, 2010.

[5] R. Mirzavand, A. Abdipour, G. Moradi, and M. Movahhedi, "Full-wave semicoductor devices simulation using ADI-FDTD method," *IET Microwaves, Antennas & Propagation*, vol. 5, no. 8, 685-691, 2010.

[6] A. Taeb, A. Abdipour, and A. Mohammadi, "Modeling and analysis of a nonlinear fully distributed FET using FDTD technique," *AEU-International Journal of Electronics and Communications*, vol. 61, 444-452, 2007.

[7] K. Afrooz, A. Abdipour, A. Tavakoli, and M. Movahhedi, "FDTD analysis of small signal model for GaAs MESFETs based on three line structure," *Asia-Pacific Microwave Conf. (APMC 2007)*, Bangkok, Thailand, December 2007.

[8] A. Orlandi and C. R. Paul, "FDTD analysis of lossy, multiconductor transmission lines terminated in arbitrary loads," *IEEE Trans. Electromag. Compat.*, vol. 38, 388-399, 1996.

[9] J. Bernal Mendez, F. Mesa, and D. R. Jackson, "Low-frequency excitation of leaky modes in a microstrip line with a top cover," *Progress In Electromagnetics Research*, vol. 114, 235-254, 2011.

[10] Z. Wang, "Reducing mutual coupling of closely space microstrip antennas for MIMO application at 5.8 GHz," *Journal of Electromagnetic Waves and Applications*, vol. 25, no. 2-3, 399-409, 2011.

[11] S. K. Koo, H. S. Lee, and Y. B. Park, "Crosstalk reduction effect of asymmetric stub loaded lines," *Journal of Electromagnetic Waves and Applications*, vol. 25, no. 8-9, 1156-1167, 2011.

[12] M. Izadi, M. Z. A. Ab-Kadir, and C. Gomes, "Evaluation of electromagnetic fields associated with inclined lightning channel using second order FDTD-hybrid methods," *Progress In Electromagnetics Research*, vol. 117, 209-236, 2011.

[13] C. Gomes and M. Z. A. Ab-Kadir, "Protection of naval systems against electromagnetic effects due to lightning," *Progress In Electromagnetics Research*, vol. 113, 333-349, 2011.

[14] S. Yamacli and M. Avci, "Accurate voltage-dependent transmission line model for carbon nanotube interconnects and the delay calculation," *Journal of Electromagnetic Waves and Applications*, vol. 25, no. 4, 553-563, 2011.

Laleh Mirzavand was born in Boroujen, Iran, in 1986. She received her B.Sc. in 2007 from Isfahan University of Technology and her M.Sc. degree in 2010 from Amirkabir University of Technology, both in Electrical Engineering. She is currently a Research Assistant with the Institute of Communications Technology and Applied Electromagnetics, Amirkabir University of Technology, Tehran, Iran. Her research interests are in the areas of microwave and millimeter-waves circuits, instrumentation and measurement techniques.

Abdolali Abdipour was born in Alashtar, Iran, in 1966. He received his B.Sc. degree in Electrical Engineering from Tehran University, Tehran, Iran, in 1989, his M.Sc. degree in Electronics from Limoges University, Limoges, France, in 1992, and his Ph.D. degree in Electronic Engineering from Paris XI University, Paris, France, in 1996. He is currently a Professor with the Electrical Engineering Department, Amirkabir University of Technology (Tehran Polytechnic), Tehran, Iran. He has authored three books, Noise in Electronic Communication: Modeling, Analysis and Measurement (AmirKabir Univ. Press, 2005, in Persian), Transmission Lines (Nahre Danesh Press, 2006, in Persian), Active Transmission Lines in Electronics and Communications: Modeling and Analysis (Amirkabir Univ. Press, 2007, in Persian - top selected book of year) and High Frequency Field Effect Transistors: Electronic-Electromagnetics Modeling & Analysis (Amirkabir Univ. Press, 2013, in Persian).

His research areas include wireless communication systems (RF technology and transceivers), RF/microwave/millimeter-wave circuit and system design, Electromagnetic (EM) modeling of active devices and circuits, high-frequency electronics (signal and noise), nonlinear modeling, and analysis of

microwave devices and circuits. He has authored or coauthored over 280 papers in refereed journals and local and international conferences. Currently, he is Director of the Institute of Communications Technology and Applied Electromagnetics, Amirkabir University of Technology (Tehran Polytechnic), Tehran, Iran.

Rashid Mirzavand received his B.Sc. degree from Isfahan University of Technology, Isfahan, Iran, in 2004, M.Sc. and Ph.D. degrees from Amirkabir University of Technology (Tehran Polytechnic), Tehran, Iran, in 2007 and 2011, all in Electrical Engineering. In September 2009, he joined the Centre for Analysis, Scientific Computing and Applications (CASA), Eindhoven University of Technology (TU/e), Eindhoven, The Netherlands, as a Visiting Ph.D. Student. He is currently an Assistant Professor with the Institute of Communications Technology and Applied Electromagnetics, Amirkabir University of Technology, Tehran, Iran. He has authored or coauthored several papers in refereed journals and international conferences and a book in Persian (High Frequency Field Effect Transistors: Electronic-Electromagnetics Modeling & Analysis; Amirkabir Univ. Press, 2013). His research interests are in the areas of RF/Microwave & mm-wave circuits, and systems, computational electromagnetic and wireless communication systems.